Segmentation of the Oral and Facial Regions from Imaging Modalities with Reduced or No Ionizing Radiation

JI DONG XU

(B. Eng.), Huazhong University of Science and Technology

A THESIS SUBMITTED FOR THE DEGREE OF DOCTOR OF PHILOSOPHY

NUS GRADUATE SCHOOL FOR INTEGRATIVE SCIENCES AND ENGINEERING

NATIONAL UNIVERSITY OF SINGAPORE

2013

Declaration

I hereby declare that the thesis is my original work and it has been written by me in its entirety. I have duly acknowledged all the sources of information which have been used in the thesis. This thesis has also not been submitted for any degree in any university previously.

Signed: Ji Dongxu

Ji Dongxu

Date: 2014/02/20

This thesis is dedicated to

My Parents,

who raised me and supported my education,

for your love and sacrifices.

My Grandparents,

whose love sustained me.

Acknowledgements

I would like to thank my supervisors Assoc. Prof. Kelvin Foong Weng Chiong, Assoc. Prof. Ong Sim Heng and members of my thesis advisory committee Prof. Kenji Takada, Dr. Yen Shih-Cheng and Dr. Ng Hsiao Piau for their guidance and help, without which my research would not be carried out smoothly.

I would also like to thank Mr. Francis Hoon, laboratory officer at vision and machine learning laboratory, for his assistance during my Ph.D. study. Special thanks to my friends and colleges in the lab Mr. Lu Yongning, Mr. Yang Yang, Mr. Zhang Zhiyuan and Dr. Wei Dong for their encouragement and company during my candidature.

Finally, I would like to thank NUS Graduate School for Integrative Sciences and Engineering (NGS) for awarding me the NGS scholarship. Many thanks go the directors, mangers and staff at NGS for their help.

Contents

Summary

With rapid advances in medical imaging technology, the use of computer tomography (CT) and magnetic resonance (MR) image data for orthodontic treatment and maxillofacial surgery has become increasingly common. Fan beam CT (traditional CT) and cone beam CT (CBCT) are two commonly used types of CT. In contrast with fan beam CT, CBCT can produce volumetric images with higher spatial resolution and lower radiation exposure to patients. But the trade-off is that CBCT is usually more noisy than fan beam CT. Both CT imaging modalities permit clinicians to study hard tissues like mandible, maxilla and teeth. In contrast with radiation-based CT, magnetic resonance imaging (MRI) presents substantial health advantages to the patient. MR imaging has no ionizing radiation and provides visualization of internal soft and hard tissues. In dentistry, CBCT is usually used to study the bone structures while MRI is used to study the muscles.

The main focus of the thesis is to present approaches for segmenting the human mandibular body from MR images and segmenting the human anterior teeth from CBCT images. Both of the segmentation approaches allow clinicians to study the oral and maxillofacial

images with 3D data taken from imaging modalities with little or noionizing radiation.

An approach for segmenting the human mandibular body from MRI was firstly presented. The segmentation of mandibular body in MRI is difficult due to the partial volume effects, missing of some bone structures and the mixture of bone with air in MR images. A two-stage rule-constrained seedless region growing approach was presented to segment the mandibular body in MRI. The proposed approach was implemented and the segmentation results were compared with other algorithms and the ground truth. The proposed method showed the best results in most scenarios. The precision of reconstruction of mandibular shape from MRI was studied by comparing with the 3D mandibular shape obtained from CT images.

An approach for segmenting the anterior tooth segmentation from CBCT was then presented. The most challenging part of tooth segmentation is to segment the root of the tooth. The new level set algorithm is able to detect the contour of the tooth root from CBCT with three novelties: (1) a more accurate estimation of intensity distributions of the tooth root is used; (2) a more robust shape prior is used to add a more reasonable shape constraint on the contour evolution; and (3) the thickness of tooth dentine wall is used as a new constraint to avoid leakage problem. The proposed approach was implemented and the segmentation results were compared with other algorithms and the ground truth. The proposed method showed the

best results in most scenarios. After segmenting the teeth, a 3D interactive tooth movement and collision detection system was then built to help the clinicians to address impacted canine cases.

List of Figures

Chapter 1

Introduction

1.1 Motivation

The oral (mouth) and maxillofacial (jaws and face) regions refer to the soft and hard anatomical tissues of the mouth, jaws, face and skull (Eder *et al.*, 2003). The hard tissues consist of jaw bones such as the maxilla, the mandible, and the teeth; the soft tissues consist of four muscles used for chewing: the masseter muscle, the medial pterygoid muscle, the lateral pterygoid muscle and the temporalis muscle (Fig. 1.1). The muscles control the movement of the mandible and the teeth for mastication (chewing). Thus the malfunction of either the muscles moving the mandible or the teeth might lead to problems in the mastication process. The aim of jaw surgery is to correct any jaw and facial deformity so that a functional balance between the hard and soft tissues of the mouth, jaws and muscles is established.

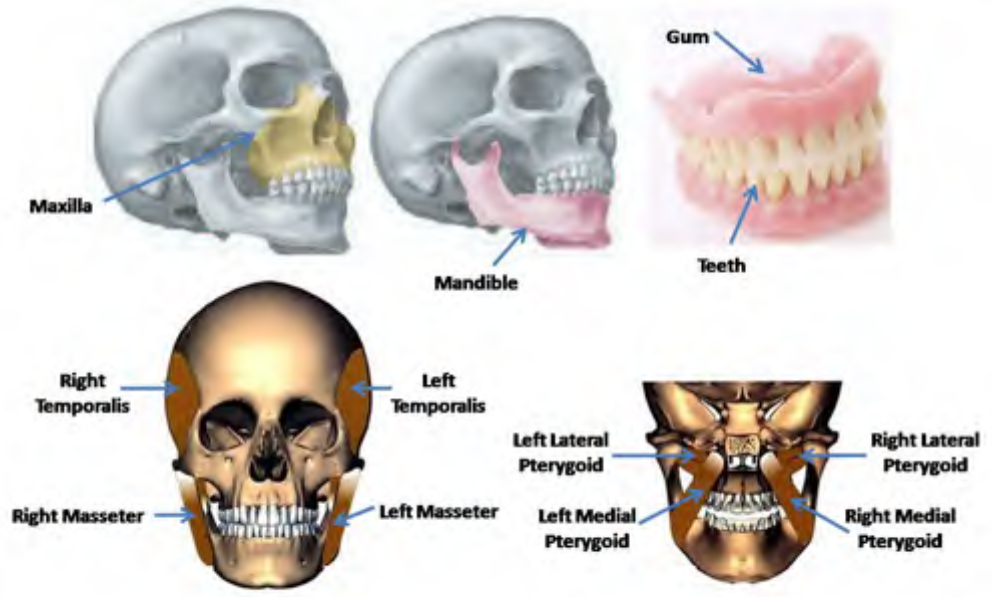

Figure 1.1: Soft and hard tissues in oral and maxillofacial region (modified from Eder *et al.* (2003); Liebgott (2011)).

Traditional pre-surgical planning for oral and maxillofacial surgeries is performed using profile tracings and plastic models. Profile tracings are intrinsically 2D and do not permit clinicians to visualize the muscles. Plastic models are 3D but only permit clinicians to visualize the surface of the crown of the tooth. In recent years, however, the availability of more powerful medical imaging machines has brought the diagnostic oral and maxillofacial imaging from the era of 2D to 3D. The application of 3D imaging like computed tomography (CT) and magnetic resonance imaging (MRI) of the oral and maxillofacial regions has become more common. Fan beam CT (traditional CT) and cone beam CT (CBCT) are two commonly used types of CT. In contrast with fan beam CT, CBCT can produce volumetric images with higher resolution and lower radia-

tion exposure to patients (Scarfe *et al.*, 2006). But the trade-off is that CBCT is usually noisier than fan beam CT. Both of them permit clinicians to study hard tissues like the mandible, the maxilla and the teeth. In contrast with X-ray based CT, magnetic resonance imaging (MRI) presents substantial health advantages to the patient. MR imaging has no ionizing radiation and provides visualization of the internal anatomy of soft tissues and hard tissues (Hashemi *et al.*, 2010). Within the limitation of current imaging technologies, the hard tissues of oral and maxillofacial images can be obtained using fan beam CT, CBCT and MRI. The soft tissues can be obtained using MRI.

With the increasing image spatial resolution and number of images taken per diagnostic scan, the use of computer algorithms and systems to process and analyze the images are in demand. The delineation of regions of interest using automated computer algorithms is a key fundamental step in fulfilling further computer aided radiological tasks. These computer algorithms, also known as medical image segmentation algorithms, are of importance in various medical imaging applications like diagnosis and treatment planning by providing 3-D visualization and 3-D measurement of the patient.

Unfortunately, the segmentation of medical images is a challenging task and there is no universal method which works for all kinds of anatomical structures. The segmentation method may fail at the same anatomical structure if the images of the structure are obtained by using a different modality or even using the same modality but in different imaging machines.

In the following sections of this chapter, previous studies of the segmentation of multi-modal oral and maxillofacial images are first provided. This is followed by the motivation of the thesis on the problems of mandibular body

Table 1.1: Status of studies on segmentation of multi-modal oral and maxillofacial images.

	MRI	CBCT	Fan beam CT
Muscles	✓	NA	NA
Mandible	×	✓	✓
Maxilla	×	✓	✓
Teeth	×	×	✓

✓: Semi-automated and automated segmentation methods have been proposed to segment the given anatomy in this modality
NA: Not applicable
×: Segmentation methods have not been proposed to segment the given anatomy in this modality

segmentation in MRI and anterior teeth segmentation in CBCT. The objectives and outline of this thesis are presented, followed by the contributions of the thesis.

1.2 Previous work

In this section, previous work on the state-of-art segmentation problems of both soft and hard tissues in oral and maxillofacial images will be briefly introduced. The segmentation methods of multi-modal oral and maxillofacial images can be classified based on the imaging modality. The current status of segmentation methods for multi-modal oral and maxillofacial images is shown in Table 1.1.

The segmentation approaches for muscles from MRI and those for hard tissues from CT in oral and maxillofacial regions have been reported in the literature. No research has been reported on the segmentation of muscles tissues in oral and maxillofacial regions from CT. In general, while some of the problems have been successfully solved, the problems of hard tissue segmentation in MRI

and tooth segmentation in CBCT remain unsolved. Segmentation algorithms reported in the literature for different structures will be briefly reviewed in the following subsections.

1.2.1 Bone segmentation from traditional CT

Several investigative approaches for the segmentation of the jaws (the mandible and the maxilla) and the teeth from traditional CT have been reported in the literature. The reported approaches are listed as follows:

(1) Segmentation of mandible from traditional CT:

- "*An automatic segmentation and reconstruction of mandibular structures from CT-data*" (Barandiaran *et al.*, 2009). This method is based on automatic multiple thresholding followed by a region-growing algorithm to extract the object of interest. However, the paper failed to carry out a statistical comparison study and thus the proposed method cannot be considered reliable.

- "*Automatic segmentation of jaw tissues in CT using active appearance models and semi-automatic landmarking*" (Rueda *et al.*, 2006). This method is based on a 2D active appearance model (AAM). The model is constructed from manual segmentation of 215 images. The authors reported a mean error of 1.63mm for the cortical bone and 2.90mm for the trabecular bone.

(2) Segmentation of maxilla from traditional CT:

- "*Automatic bone and tooth detection for CT-based dental implant planning*" (Nguyen *et al.*, 2012). This method is similar to the segmentation

method proposed by Kainmueller *et al.* (2009). The authors build a statistical shape model (SSM) for maxilla from 43 manually segmented CT and CBCT datasets. The details of the segmentation algorithm are presented in Nguyen (2012). They achieve a segmentation accuracy of 0.5±0.5mm for the maxillary bone surface distance between the adapted SSM and the ground truth.

(3) Segmentation of teeth from traditional CT:

- "*Automated segmentation of teeth in multi-slice CT images*" (Keyhaninejad *et al.*, 2006). This method is based on the level set method. They firstly obtain the head mask, then hard tissues are separated from other tissues by a level set technique. The teeth are then segmented from other hard tissues using the distinct intensity of teeth.

- "*Individual tooth segmentation from CT images using level set method with shape and intensity prior*" (Gao & Chae, 2010). This method is also based on the level set method. This method generates a shape prior with intensity and boundary features and integrates the three terms into one energy functional to be minimized. They use the framework to segment the crowns and roots of individual teeth. The segmented crown and root are finally merged to render the shape of the tooth. Their segmentation approach works well for CT images.

1.2.2 Bone segmentation from CBCT

(1) Segmentation of mandible from CBCT:

- "*Automatic Segmentation of Mandibles in Low-Dose CT-Data*" (Lamecker *et al.*, 2006). The method is based on segmenting the mandible using an active shape model (ASM), which is constructed from 13 manually segmented individual mandible shapes. A training data set is first manually decomposed into 8 patches, and then an automatic method is used to find the surface correspondences needed to build an ASM. The segmentation is eventually achieved by two phases of matching.

- "*Fully automatic shape constrained mandible segmentation from cone-beam CT data*" (Gollmer & Buzug, 2012). The method is based on the statistical shape model (SSM). In contrast to previous approaches, the method was fully automated in terms of both the establishment of statistical shape model and the segmentation itself. The segmentation accuracy is similar to that of previous SSM based mandible segmentation approaches whereas the size of their training sample is 3.5 times smaller.

(2) Segmentation of maxilla from CBCT:

- "*3D segmentation of maxilla in cone-beam computed tomography imaging using base invariant wavelet active shape model on customized two-manifold topology*" (Chang *et al.*, 2013). The method is based on wavelet density model (WDM) to segment the outer surface of the anterior wall of maxilla. Nineteen CBCT datasets are used to conduct two experiments. This mode-based segmentation approach is validated and compared with 3 different segmentation approaches. The results show that the performance of the proposed segmentation approach is better than those of the other approaches. Their results have a 0.25 ± 0.2 mm surface error from

the ground truth.

1.2.3 Muscle segmentation from MRI

The problems of segmentation of muscles within oral and maxillofacial region in MRI have been systematically studied (Ng *et al.*, 2006b, 2007a,b, 2008, 2009, 2010). Ng (2008) used an improved watershed segmentation algorithm which implements a post-segmentation merging step, based on both intensity and spatial criteria, to reduce the number of partitions significantly. The segmentation accuracy was improved by preprocessing with K-means clustering before applying the improved watershed algorithm. They explored the use of the gradient vector flow (GVF) snake (Xu & Prince, 1998) to segment the masticatory muscles from 2D MR images. Finally they reported the methods that incorporate information from patient specific models by matching distributions of the pixel intensity values to segment the human masticatory muscles from MRI.

These segmentation approaches provide the engineering solutions for automated segmentation of the muscles in MRI, which are intended to free the clinicians from tedious and time-consuming work on manual segmentation of the soft tissues.

1.2.4 Remaining segmentation problems

We have seen that the hard tissues can be segmented from both traditional fan beam CT or the more noisy low-dose CBCT except for one remaining segmentation case, namely tooth segmentation in CBCT. The soft tissues in MRI have already been addressed. However, no one has reported automated segmenta-

tion of hard tissues in MRI. The remaining problems in multi-modal oral and maxillofacial images are the main concerns of this thesis.

1.3 This Thesis

This section presents the objectives and the outline of the thesis and states its contributions.

1.3.1 Objectives and outline of the thesis

1.3.1.1 Objectives

The objectives of the study are:

- To develop an automated method to extract the human mandible body shape from magnetic resonance (MR) images of the head.
- To determine the validity of magnetic resonance imaging (MRI) as a non-ionising imaging modality for generating a realistic shape of the mandible and to evaluate the precision of the mandibular shape.
- To develop an improved level set method to extract the shapes of anterior teeth from CBCT images of the head.
- To develop a 3D interactive tooth movement and collision detection system to assist the clinicians in treatment planning.

1.3.1.2 Outline of the thesis

The thesis consists of seven chapters, including this introductory chapter.

- In chapter 2, we present medical concepts and commonly used segmentation techniques with which the thesis is related.
- In chapter 3, we present a two-stage rule-constrained seedless region growing approach for mandibular body segmentation in MRI.
- In chapter 4, we present a precision study of the reconstruction of mandibular shape from magnetic resonance imaging.
- In chapter 5, we present a segmentation algorithm of anterior teeth in cone beam computed tomography images using the level set method.
- In chapter 6, we present a 3D interactive tooth movement and collision detection system.
- Finally, in Chapter 7, we conclude the thesis with the achievements and recommendations for future work.

1.3.2 Thesis contributions

The main contributions of this thesis are the segmentation algorithms for mandible from MRI and teeth from CBCT, both of which are located in the oral and maxillofacial area. These segmentation approaches allow clinicians to study the oral and maxillofacial images with 3D data in modalities that present no or relatively lower radiation to the patients. The two segmentation algorithms are followed by two medical studies. The significant contributions of this thesis are given as follows:

- The proposed two-stage rule-constrained seedless region growing approach

for mandibular body segmentation in MRI can address the leakage problem in mandible segmentation from MRI (Chapter 3). With the proposed automated segmentation approach, the shape of the mandibular body can be obtained without making the patient undergo another round of CT scanning. This will decrease the radiation dosage exposed to the patient. The segmented mandible can be integrated with the segmented muscles to build a complete skeletal muscle system to better analyze the masticatory system for specific patients.

- A precision study of the reconstruction of the mandibular shape from magnetic resonance imaging is described in Chapter 4. The study shows that the shape of the mandibular body generated from MRI are as accurate as those generated from CT. However, the anatomical areas at the coronoid processes and condylar heads generated from MRI are less precise when compared with those generated from CT imaging.

- The level-set based segmentation algorithm can segment the anterior teeth in CBCT images (Chapter 5). The proposed method is better than previous methods in its capability to define the root boundary. Previous methods work only for fan beam CT data, while the proposed method offers a solution for tooth segmentation in the lower-radiation imaging CBCT.

- Finally, a 3D interactive tooth movement and collision detection system is built to assist the clinicians find feasible solutions for patient specific impacted canine cases (Chapter 6).

Chapter 2

Preliminaries

This chapter presents relevant anatomical concepts, medical imaging techniques and reviews related segmentation methods. In Section 2.1, we describe the anatomies of the mandible and teeth, which are the regions of interest of this thesis. We discuss image modalities used in medical applications in Section 2.2. Finally, we give a review of the related segmentation methods in Section 2.3.

2.1 Mandible and teeth

2.1.1 Overview

In this thesis, we focus on analyzing tooth and mandible segmentation algorithms. Thus we will describe these two regions in detail.

2.1.2 Mandible

The human mandible (also known as the lower jaw), is the strongest and largest facial bone and serves to hold the lower teeth (Fig. 2.1). The components of the mandible are:

- The body of the mandible is the horizontal part on each side.
- The alveolar margin is upper portion of the mandibular body.
- The ramus is the ascending part of the mandible at each side.
- The angle of the mandible is at the junction of the lower border of the ramus with the posterior border.
- The condyle is a rounded knob by means of which the mandible can make all its movements.
- The coronoid process is a sharp projection at the top of each ramus and in front of the condyle.

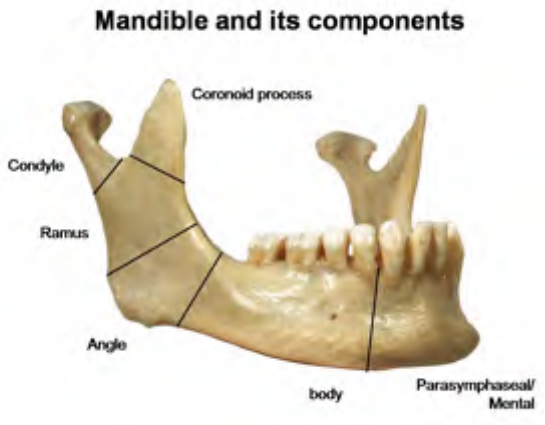

Figure 2.1: Mandible and its components (from Wikimedia Commons).

2.1.3 Tooth

Human teeth are white hard structures embedded in the jaws (maxilla and mandible) and are covered by gums. The function of the teeth are cutting and crushing food in preparation for swallowing and digestion. Teeth are made of various tissues of different hardness and density.

Humans usually have 32 permanent teeth, which are classified as incisors, canines, premolars and molars (Fig. 2.2).

Figure 2.2: Permanent teeth of right half of lower dental arch, seen from above (from Wikimedia Commons).

The tooth can be separated into two regions: the crown and the root. The area that lies above the cementoenamel junction (the "neck" of the tooth) is called the crown. It is made of dentin with a pulp chamber inside (Cate, 1998). The area below the cementoenamel junction and covered with cementum is called the root. Similar to the crown, the root is also composed with dentin and pulp. The different parts of a tooth are described as follows (Fig. 2.3):

Figure 2.3: Section of a human tooth (from www.studiodentaire.com).

- Enamel, made of calcium phosphate, is the hardest substance of the tooth body. Its thickness varies over the surface of the tooth body.
- Dentin is softer than enamel, it decays more rapidly and is vulnerable to cavities if not treated properly.
- Periodontal ligaments (PDL) are a group of tissue fibers which attach a tooth to the alveolar bone (Fig. 2.3).
- Covering the root of the tooth, cementum is a substance like bones (Cate, 1998). It is softer than either enamel or dentin. It functions as a medium by which the PDL attaches to the tooth for stabilization.
- Pulp is the soft, living central structure of teeth. It consists of blood vessels and nerves (Cate, 1998).

2.2 Medical imaging modalities

This section introduces the medical imaging modalities used in this thesis.

2.2.1 Computed tomography

In 1972, Hounsfield publicly introduced the first clinical CT scanner and described its design in 1973 (Hounsfield, 1973). Since then, X-ray computed tomography (CT), which uses computer-processed X-rays to generate "slices" of region of interest (ROI), becomes one of the commonly used medical imaging modalities. The 3D CT has several advantages over traditional 2D x-ray images: (1) CT eliminates blurring resulting from the superimposition of structures outside the region of interest; (2) due to the high-contrast resolution of CT, differences between tissues which have different physical density (mass density) can be easily distinguished (Mull, 1984; Phillips & Lannutti, 1997); (3) unlike conventional X-ray radiography which projects 3D body structure onto a 2D image, CT generates several slices of 2D images, with about 1mm slice thickness, of the body. CT images can be viewed in the axial (horizontal), coronal, or sagittal planes, depending on the diagnostic demand. However, the resolution of CT is not as good as that of conventional x-ray images.

Computed tomographic scanning is used in several medical applications such as the detection of cancers , injured or dead tissues, blood clots and cysts. CT can be divided into two types, fan beam and cone beam, based on geometries of acquisition X-ray beam (Scarfe *et al.*, 2006) (Fig. 2.4).

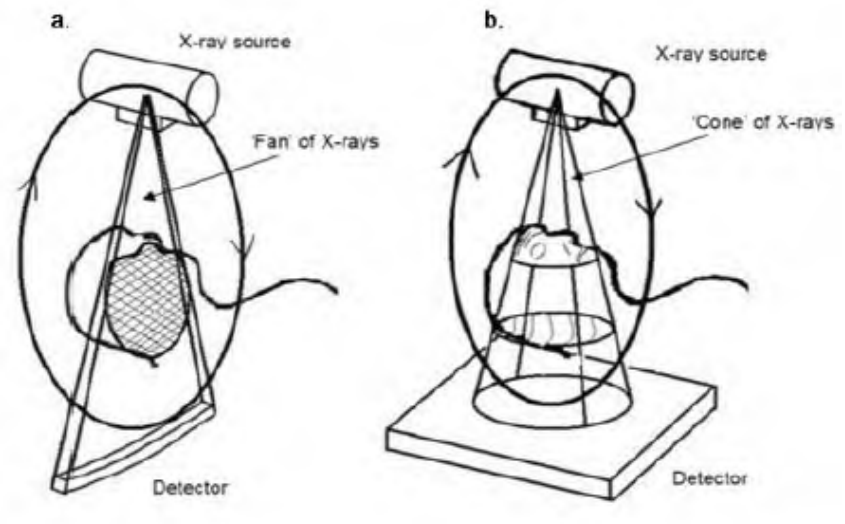

Figure 2.4: Different X-ray beam projection schemes. (a) fan-beam CT; (b) cone-beam CT (from Scarfe *et al.* (2006)).

The first-generation of fan beam CT gantries employ a scanning mechanism, also known as "traverse and index". A narrow pencil beam from a collimated source traverses the slice linearly to obtain a projection. The frame is then rotated to obtain more such projections. Since the first-generation of CT gantries, it has undergone 6 generations of refinements until the seventh-generation gantries, which are known as multi-slice CT (MSCT). In contrast with the scheme of single row detectors, multiple detectors are placed close to each other so that could simultaneously collect data from multiple slices (Fig. 2.5). The advantages of MSCT are a much shorter imaging acquisition time and improved 3D rendering quality with decreased helical artifacts.

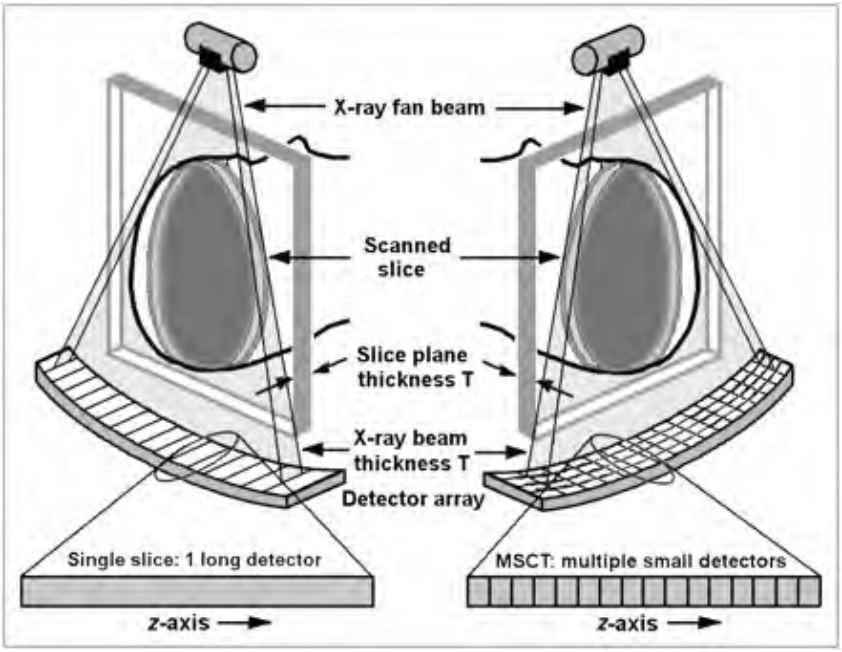

Figure 2.5: Difference between single detector CT and multiple detector CT (from Goldman (2008)).

In contrast with fan-beam CT, cone-beam CT (CBCT) scanners use 2D digital arrays to provide an area detector which is combined with a 3D beam (Fig. 2.4b). The scheme of cone-beam CT involves a single $360°$ scan in which a x-ray source and a detector move around the patients head at the same time. During the scanning, the patients head is stabilized with a head holder (Fig. 2.6). Computing algorithms such as filtered backprojection or iterative reconstruction methods are applied to these acquired projections to generate 3D volumetric images, which can be displayed in axial, sagittal and coronal planes.

Figure 2.6: Cone-beam computed tomography system. A phantom is stabilized with a head holder (from U.S. Food and Drug Administration website).

Compared with traditional fan-beam CT, CBCT is more suitable for imaging the oral and maxillofacial region. It provides high-quality images of contrasted structures and is very useful for evaluating hard tissues (Sukovic, 2003; Ziegler *et al.*, 2002). Similar to conventional CT, limitations exist in the use of CBCT for imaging soft tissues. The application of CBCT in clinical practice shows present advantages for oral and maxillofacial imaging over conventional CT:

- Imaging resolution: The volumetric data set consists of a 3D collection of smaller cubic elements, also known as voxels. A voxel (volumetric pixel) is a volumetric element in a regular grid in 3D space. Although conventional CT images can be as small as 0.625mm square in a given plane, the thickness between slices is usually 1$\sim$2mm. Unlike the anisotropic resolution of conventional CT, all CBCT scanners provide spatial resolution that are isotropic (equal in 3 orthogonal planes). This provides

sub-millimetre resolution result (even exceeding the resolution of most MSCT) ranging from 0.4mm to 0.125mm.

- Scan time: Because CBCT can acquire all image projections in a single rotation, scan time is usually around 1 minute, which is comparable with those of conventional CT systems. Faster scanning time can reduce motion artifacts.

- Field of view (FOV): The FOV of most CBCT scanners can be adjusted to small regions of interest for specific diagnostic tasks. They are also capable of scanning the whole craniofacial complex.

- Radiation dose reduction: Research publications indicate that, compared with fan-beam CT, CBCT is able to reduce the effective dose of radiation significantly by as much as 98% (Cohnen *et al.*, 2002; Dula *et al.*, 1996; Heiland *et al.*, 2004; Ludlow *et al.*, 2003; Mah *et al.*, 2003; Ngan *et al.*, 2003; Scaf *et al.*, 1997; Schulze *et al.*, 2004). The effective dose of radiation has been reduced to that of a periapical dentition survey, which is 4-15 times that of a panoramic radiograph (Danforth & Clark, 2000; Gibbs, 2000; Ngan *et al.*, 2003; White, 1992).

- Reduced image artifact: Thanks to improved artifact suppression algorithms and more imaging details, published reports have shown that CBCT images can introduce a low level of imaging artifacts, especially in reconstructions of the teeth and jaws (Cohnen *et al.*, 2002; Scarfe *et al.*, 2006).

2.2.2 Magnetic resonance imaging

Magnetic resonance imaging (MRI) is a medical imaging modality which uses magnetic field and radio waves to image internal structures inside the body. Unlike CT, MRI has no ionising radiation. Compared with CT, it has more imaging contrast for soft tissues like brains and muscles. It can detect diseased tissues like tumors.

In MRI, tissues can be differentiated on the basis of spin-lattice relaxation time (T_1) and spin-spin relaxation time (T_2). In physics, spin-lattice relaxation denotes the mechanism by which the longitudinal component of the magnetic moment comes into thermodynamic equilibrium with its surroundings (the "lattice"). The signal decay process is characterized by the time constant spin-lattice relaxation time (also known as T_1). Similarly, spin-spin relaxation denotes the mechanism by which the transverse component of the magnetic moment comes into the equilibrium value of zero. The signal decay process is characterized by the time constant spin-spin relaxation time (Hashemi *et al.*, 2010). The imaging differences between these two types of MRI settings are illustrated in Fig. 2.7.

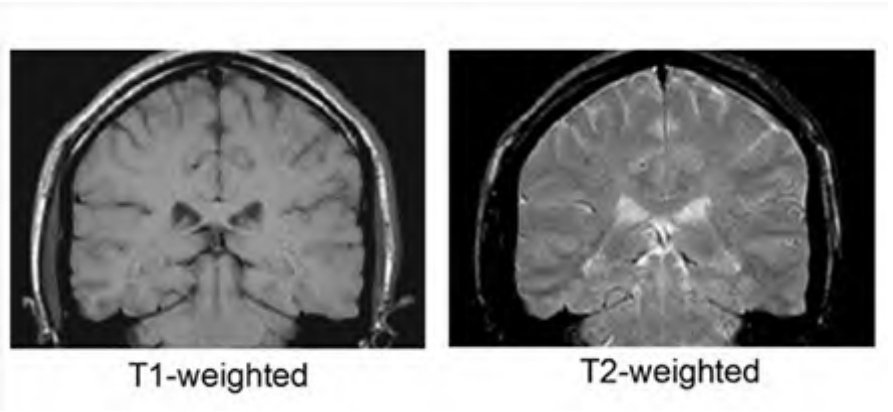

Figure 2.7: Comparison between T_1-weighted MRI and T_2-weighted MRI.

2.3 Review of related segmentation methods

Medical image segmentation, which plays an important role in medical imaging applications, is one of the most fundamental and challenging problems in medical image analysis. It uses automated or semi-automated methods to partition anatomical structures out from their surrounding environments. We will review existing segmentation methods with an emphasis on discussing the advantages and disadvantages of using these approaches to solve medical imaging problems. We will also discuss the application of image segmentation methods for different imaging modalities and the corresponding difficulties.

2.3.1 Overview

Diagnostic imaging is frequently used in medical applications. MRI, CT and other medical imaging techniques provide various ways to map the anatomy of human organs or other interior structures. With the increasing resolution and number of patient images, the use of computer algorithms to process and analyze them are in demand. The delineation of regions of interest using automated computer algorithms is a key fundamental step in fulfilling further radiological tasks. These computer algorithms, also known as medical image segmentation algorithms, are of importance in various medical imaging applications like diagnosis and treatment planning (Khoo *et al.*, 1997; Taylor, 1995), computer-assisted surgery (Grimson *et al.*, 1997; Jolesz *et al.*, 2001), anatomical structure study (Farag *et al.*, 2005), biological processes simulation (Prastawa *et al.*, 2009), pathology localization (El-Baz *et al.*, 2006) and tracking the progress of diseases (Gra; Greenspan *et al.*, 2006).

However, segmentation of medical images is a challenging task due to the following reasons:

- Regions within the target anatomical structures usually have inhomogeneous intensities because they might be consist of various tissues.
- The surrounding background may also have inhomogeneous intensities One typical example (human mandibular body on an MRI) is shown in Fig. 2.8: the mandibular body is difficult to segment because of inhomogeneous intensity distributions both within and outside it.
- Segmentation becomes more challenging when medical images are low contrast and noisy: e.g., tooth boundaries on a typical CBCT image in Fig. 2.8 are difficult to delineate even manually by a well trained dentist.

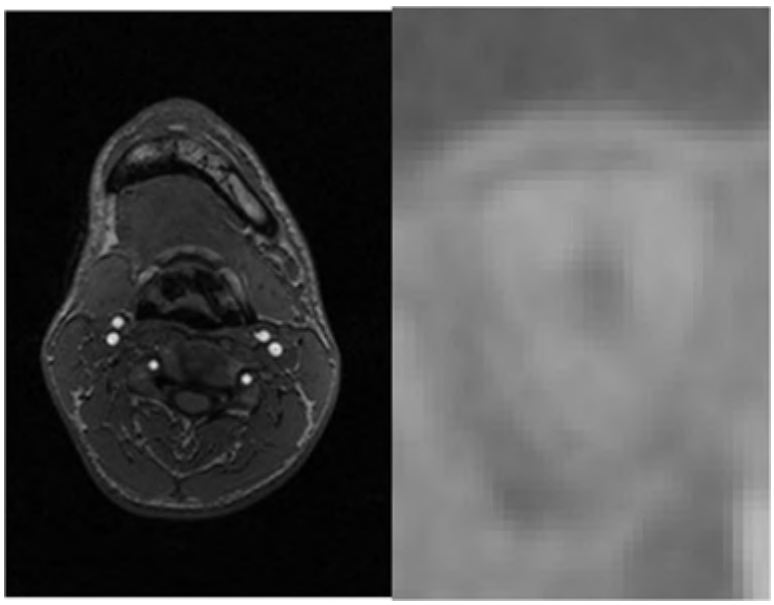

Figure 2.8: Segmentation difficulties: image inhomogeneity, low contrast and noise (Left image is a human mandibular body on an MRI; right image is a human tooth on a CBCT).

Many segmentation approaches have been developed and reported in the literature to overcome these challenges. Segmentation algorithms vary widely with demands of specific applications and imaging modalities. For instance, the segmentation of the mandibular body has different requirements from the segmentation of the tooth. Each imaging modality has specific characteristics which directly influence the performance of segmentation algorithms. Other common imaging artifacts like inhomogeneity, noise, partial volume effects also raise more challenges to the segmentation algorithms. Generally, no universal segmentation method works for all kinds of medical images, and various approaches with different segmentation accuracy, computing speed, and degree of complexity have been applied for different medical problems. General methods can be used in a variety of images. However, special methods designed according to specific medical demand usually perform better by taking advantage of prior knowledge like anatomical features.

2.3.2 Related segmentation approaches

Many reviews on image segmentation can be found in the literature, e.g. (Freixenet *et al.*, 2002; Haralick & Shapiro, 1985; Pal & Pal, 1993; Wirjadi, 2007). Specific surveys on medical image segmentation have already been reported (Bezdek *et al.*, 1993; Ma *et al.*, 2010; Pham *et al.*, 1997; Sharma & Aggarwal, 2010; Suetens *et al.*, 1993). In this subsection, segmentation methods in medical image segmentation with which the thesis is related will be described. We will give the definition, provide the scheme, and describe the advantages and disadvantages for each related approach. Each algorithm is separately intro-

duced, but many algorithms combine different methods to solve medical image segmentation problem in a proper manner.

We will review several types of segmentation methods: (1) rule-based segmentation, (2) segmentation by pattern classification models, (3) segmentation with active contour models, (4) active shape/appearance models. Rule-based segmentation includes two renowned segmentation approaches: (1a) thresholding and (1b) region growing (1c) watershed. Segmentation by pattern classification models covers two frequently used methods: (2a) classifiers and (2b) clustering.

Many segmentation algorithms can be formulated as an optimization problem where specific cost or energy functions defined by images features are minimized over certain regions of interest. Several approaches have been proposed to optimize the best segmentation. Global optimization approaches such as dynamic programming, annealing algorithm, or genetic algorithms are frequently used to solve such problems.

2.3.2.1 Gray Level thresholding

Gray level thresholding is one of the simplest and most frequently used approaches for medical image segmentation. The thresholding aims to find a value, called the "threshold", based on global intensity distributions. Local thresholding methods are also called adaptive thresholding (Chow & Kaneko, 1972; Zhang *et al.*, 2010). Thresholding is called bilevel thresholding when the image is required to partition into just the object (white) and the background (black). It is called multithresholding when the image is required to partition into more than two regions (Cao *et al.*, 2002; Jiang & Mojon, 2003; Papamarkos *et al.*,

2000; Sahoo *et al.*, 1988). If the region of interest has a distinct intensity level range, the histogram of the image will be bimodal with a obvious valley. Then the threshold can be easily selected as the bottom of the valley. However, the situation for most medical images are far from this simple and it is not trivial to select proper threshold. Various approaches have been proposed for such problems (Kittler & Illingworth, 1986; Nakagawa & Rosenfeld, 1979; Otsu, 1979; Pal & Pal, 1991; Perez & Gonzalez, 1987). Thresholding can be used as an initial step to obtain a rough shape of the region of interest. Its accuracy is limited when the image has noisy quality, uneven background or poor illumination. It will be difficult to find an effective threshold from the histograms of such images. This leads to the proposals of adaptive thresholding which takes advantage of information of connectivity and local intensities (C. Lee & Unser, 1998; Jiang & Mojon, 2003; Yanowitz & Bruckstein, 1989; Zhang *et al.*, 2010).

2.3.2.2 Region growing

The philosophy of the region growing approach (Adams & Bischof, 1994; Fabijaska, 2009; Kim *et al.*, 2006; Park & Lee, 2009; Sonka *et al.*, 1996) is that all pixels belonging to the region of interest are similar in terms of some predefined criteria. The main difference between various proposed region growing approaches lies in specifying the homogeneity criteria to guide the initial region to approach its final target region of interest (ROI). One of the most frequently used region growing criteria is that a pixel belongs to the ROI if its gray value is within a predefined range of the mean value of the ROI.

More advanced region growing techniques using both gray value homogeneity and shape prior are proposed (Modayur *et al.*, 1997). The philosophy behind

the method is to design the decision function using the region size adaptively: At early steps, the region have only small number of pixels, pixels are added as long as their gray value variances are within a homogeneity threshold. When the size of the ROI reaches a threshold, more pixels are added if their gray values are close to the mean gray value of the ROI. In the growing process, a weighting function depending on the size of the ROI is used to determine when the decision function switches from gray value variance mode to mean gray value mode (Modayur *et al.*, 1997).

The previously described region growing methods consider one connected region at a time. In contrast with them, the seeded region growing (SRG) approach was proposed to segment the image with disjoint subregions (Fan *et al.*, 2005). Given a set of seeds $(S_1, S_2, ..., S_n)$, in each step of SRG, pixels are added into one of the n seed sets. These seeds are gradually replaced by the centroids of these new generated subregions. The pixels lie in different regions are labeled with different symbols. The labeled pixels are named the "allocated pixels", and the unlabeled are named the "unallocated pixels". The unallocated pixels are added into different subregions according to some distance measures, such as the difference of the pixel's gray value to a subregions mean gray value. The SRG approach suffers from problems like seed generation and pixel labeling (Fan *et al.*, 2001; Mehnert & Jackway, 1997).

The unseeded region growing is a type of region growing without initialization of any seed point (Lin *et al.*, 2001). Initially, there is only one region containing just one randomly selected pixel. A pixel is added to a found region if it is within a threshold under a distance measure and the measure should be the minimum among all the found regions. If the pixel belongs to non of the exist-

ing regions, a new region will be generated. As the iteration number increases, the number of new generated regions will increase.

Region growing can be used either alone or with other image processing methods, especially for the segmentation of structures like brains, tumors and lesions (Gibbs *et al.*, 1996; Park & Lee, 2009; Pohlman *et al.*, 1996). Segmentation using region growing techniques may have holes or disconnected regions due to noise. Partial volume effects can cause "leakage" problem to connected regions which should be separated.

2.3.2.3 Watershed

The watershed algorithm is a rule-based technique which is widely used to segment medical images (Roerdink & Meijster, 2000; Vincent & Soille, 1991). It is usually used to divide the image into distinct regions even when the contrast is poor. In the watershed algorithm, the image is treated as a 3D chart, where each pixel in the image denotes the plane coordinates, and the height of each pixel on the plane is given by its corresponding intensity level. The algorithm starts by "pouring water" (increase threshold value) in the chart from the lowest basin to the highest peak. In the process, some peaks separating the catchment basins are detected. These peaks, which are the boundaries of neighboring catchment basins, are termed as the "watershed", and the catchment basins detected in the segmentation process are the boundaries of the targeted partitions. The segmentation process of the watershed algorithm is illustrated in Fig. 2.9.

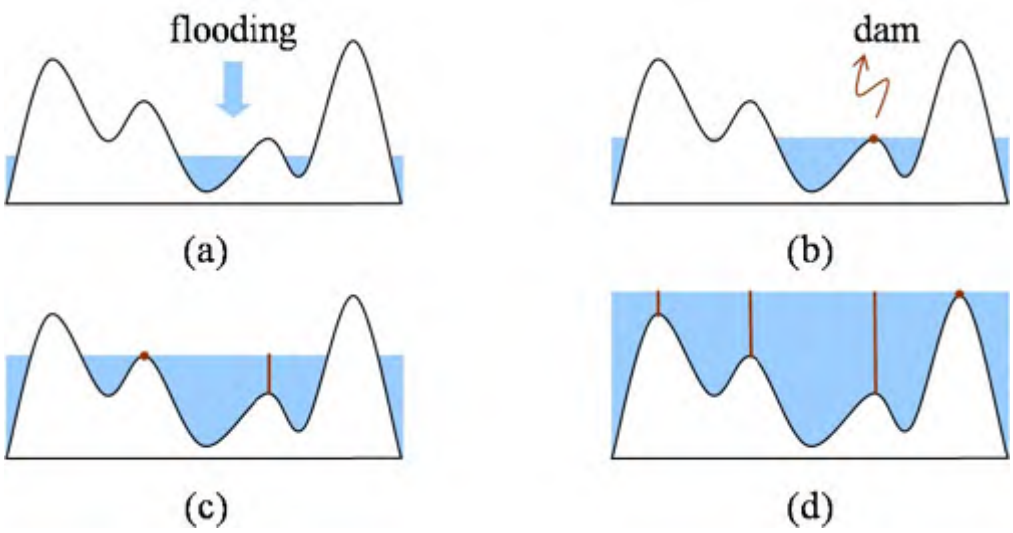

Figure 2.9: Flooding process in the watershed algorithm: (a) "pour water" in the chart; (b) a dam can be built when a local peak is detected; (c) more dams are built; (d) all the dams are built when all peaks are detected.

Despite its advantages, the watershed algorithm has some obvious shortcomings, such as over-segmentation and sensitivity to false edges. More specifically, watershed segmentation often leads to a large number of partitions, and such over-segmentation seriously reduces its effectiveness. Furthermore, the watershed technique is vulnerable to false edges due to noisy points and local variations of the image.

Numerous approaches have been proposed to improve the watershed technique for medical image segmentation. Tek & Aras (2004) proposed a three-layer basin filling watershed algorithm, which combines breadth-first basin filling and depth-first basin filling to improve the segmentation results. Ng (2008) used an improved watershed segmentation algorithm which implements a post-segmentation merging step, based on both intensity and spatial criteria, to reduce the number of partitions significantly.

Watershed algorithms have been applied in medical applications such as segmentation of masticatory muscles from MR images (Ng, 2008), lesion segmentation (Alush *et al.*, 2010) and lung lobe segmentation (Ukil & Reinhardt, 2009).

2.3.2.4 Classifiers

The problem of classification is actually inter-linked with the problem of segmentation (Bezdek *et al.*, 1993; Chyzhyk *et al.*, in press; Roy *et al.*, 2012; Schalkoff, 1992). Notify that we can assign a label of tissue to any pixel in a medical image, where the labels are selected in advance according to the medical applications. In the case of tooth segmentation, the classes could be tooth, alveolar bone, and other tissues. A feature space can be derived from such training data sets to segment the image into a set of regions. The feature space can be any function of the original or smoothed image. The most frequently used features are the intensity values, shapes and textures.

There are numerous classifier models available to train the samples. One of the simplest pattern recognition techniques, the k-nearest neighbor (k-NN) algorithm classifies objects using the closest distance training samples in a feature space (Duda *et al.*, 2000). The distance can be a function of the image features such as the pixel intensity.

Parzen windows classification is another nonparametric classifier (Babich & Camps, 1996). Given a kernel function, the Parzen windows classification can approximate the probability density function (PDF) of a training set through a linear combination of predefined kernels centered at the pixel intensities.

With respect to parametric classifiers, the maximum likelihood (ML) classifier is one of the most commonly-used models (Cam & Lucien, 1990; Rahmati

et al., 2012). The classifier groups each pixel using its probability of belonging to a particular class. It assumes that the PDF of pixel intensities are independent and follows the Gaussian distribution for each class. The parameters of the Gaussian models, such as the mean and the covariance matrix, can be estimated with expectation-maximization (EM) techniques. Although it is more computationally efficient than methods like k-NN, ML may not work in cases where there are huge overlaps between the Gaussian PDF for different classes. ML will cause many misclassifications for the segmentation task. Thus even a few noises can change influence the performance of the ML classification.

To overcome these problems, spatial information must be used. The Markov random field (MRF) can be used to address such issue. It assumes that probability of any class label depends only on the local neighboring or nearby pixels. Such local correlations can be used to model various image properties (Li, 1995). It can model the phenomena in medical imaging that most pixels have the same labels as their nearby pixels. MRFs are usually used to model the PDF of different tissues in medical images and correct the bias field occurring in MR brain images (Joshi *et al.*, 1997).

MRF is seldom used alone but often with other algorithms such as the K-means clustering and level set (Held *et al.*, 1997; Rajapakse *et al.*, 1997; Shahvaran *et al.*, 2012). The disadvantages of using MRF models are: (1) It's difficult to select proper parameters for the spatial interactions; (2) They usually ask for intensive computations to run the algorithms.

Classifiers can be used to segment medical structures that have quantifiable features. The labeled training sets can help the segmentation algorithms to recognize the interested structures in new data sets. However, the labeling pro-

cesses are usually obtained by manual segmentations which are both tedious and time consuming.

2.3.2.5 Clustering

As a unsupervised method, segmentation using clustering works in a similar way as classifiers except without predetermined classification labels. The basic idea is to develop all labels directly using the available images and features. K-means (Chen *et al.*, 1998; Ng *et al.*, 2006a) and fuzzy c-means (Chuang *et al.*, 2006; Mohamed *et al.*, 1999) are two frequently used clustering techniques for image segmentation. K-means clustering partitions pixels in the image into k clusters in which each pixel is labeled as one cluster with closest mean intensity via an iterative refinement for the mean intensity of each cluster. The fuzzy c-means method is similar to but more general than the K-means method. In fuzzy c-means clustering, each pixel can belong to more than one cluster and have a partition matrix to describe the degree to which a pixel belongs to which cluster (Bezdek *et al.*, 1993).

Clustering algorithms require an initialization of segmentation parameters which influence the performance of the segmentation. They are sensitive to intensity inhomogeneities because they usually ignore the spatial information in the images. Segmentation based on clustering techniques is more robust if the Markov random field is incorporated.

2.3.2.6 Active contour models and level set methods

Active contour models, also known as snakes, are model-based techniques for delineating an object outline using closed parametric contours which deform

via a combination of internal and external forces (Kass *et al.*, 1988). Firstly, a closed contour must be initialized close enough to the desired boundary. Then the contour can evolve towards the target object outline by means of energy minimization. In this framework, the active contour can be modeled as an energy minimization determined by both internal and external energy. The internal energy is minimized when the curve approaches a shape similar to the target object. The external energy is minimized when the regularized gradient near the contour reaches a peak value.

Mathematically, the snake model in Kass *et al.* (1988) can be characterized by the following functional:

$$J_{snake}(C) = \lambda_1 \int_0^1 |C_s(s)|^2 ds + \lambda_2 \int_0^1 |C_{ss}(s)|^2 ds \\ -\lambda_3 \int_0^1 |\nabla u_0(C(s))|^2 ds \tag{2.1}$$

where λ_1, λ_2, λ_3 are positive weighting parameters, $C(s)$ the parameterized curve representing the active contour, $C_s(s)$ the first order derivative of $C(s)$, $C_{ss}(s)$ the second order derivative of $C(s)$, $|\nabla u_0|$ the edge detector, usually defined as a positive and decreasing function $g(|\nabla u_0|)$ dependent on the gradient of the image. A typical example of such a function is

$$g(|\nabla u_0|) = \frac{1}{1 + |\nabla u_G|^2} \tag{2.2}$$

where $u_G = G_\sigma * u_0$, the convolution of the image with the Gaussian kernel of standard deviation σ, is a smoothed version of u_0.

The first-order and second order term controlled by λ_1 and λ_2 respectively,

serve as the internal energy which controls the smoothness of the active contour, while the third term serves as the external energy to attract the contour to approach the object in the image. The optimization of the contour evolution can be solved by the calculus of variations (Weinstock, 1952). Given a 2D function of the image $u(x, y) : \Omega \in R^2 \rightarrow R$ and an energy functional J,

$$J(u) = \iint_{\Omega} f\left(u, \frac{\partial u}{\partial x}, \frac{\partial u}{\partial y}, \frac{\partial u^2}{\partial x^2}, \frac{\partial u^2}{\partial y^2}\right) dxdy \tag{2.3}$$

where Ω is the set of all pixels in the image, $f : R^2 \rightarrow R$ is designed according to different segmentation problems. Usually the optimal segmentation is obtained when $J(u)$ is minimized. The Euler-Lagrange equation, which is the condition for the minimization problem, is given by:

$$\frac{\partial f}{\partial u} - \frac{d}{dx}\left(\frac{\partial f}{\partial u_x}\right) - \frac{d}{dy}\left(\frac{\partial f}{\partial u_y}\right) + \frac{d^2}{dx^2}\left(\frac{\partial f}{\partial u_{xx}}\right) + \frac{d^2}{dy^2}\left(\frac{\partial f}{\partial u_{yy}}\right) = 0 \tag{2.4}$$

The the left hand side of the above Euler-Lagrange equation is $\frac{\partial J}{\partial u}$, which is the Gateaux derivative (first variation) of the functional J.

The gradient flow of the function u with respect to step time t is defined as $\frac{\partial u}{\partial t}$. The iterative solution of the minimization problem is given by the relationship between the Gateaux derivative and the gradient flow:

$$\frac{\partial u}{\partial t} = -\frac{\partial J}{\partial u} \tag{2.5}$$

The active contour can also be implemented in other ways. One alternative is the GVF active contour (Paragios *et al.*, 2004; Xu & Prince, 1998), where

the snake is implemented using a new kind of external field, the gradient vector flow (GVF). GVF snakes converge to the object's boundary concavities and initialization of the contour is not required to be close to the boundary.

The second alternative is called the balloon snake (Cohen, 1991). In this model, the contour moves like a balloon. It modifies the external forces described by the traditional snake and introduces a new force to push the contour such that it moves like a balloon.

The third alternative is the diffusion snake (Cremers *et al.*, 2002) which is a modification of the Mumford-Shah functional. In this model, the segmentation is obtained by maximizing both the intensity homogeneity in different regions and the similarity between the contour and a set of shape priors.

The final one is the geometric active contour (Caselles *et al.*, 1997). Such models can be implemented using level sets (Gao & Chae, 2010; Li *et al.*, 2005; Osher & Sethian, 1988; Tsai *et al.*, 2003) and are extensively used in medical image segmentation. In the level set method, the active contour C is represented implicitly via a signed distance function (SDF) (Fig. 2.10) ϕ by $C(t) = \{(x, y) \in \Omega | \phi(t, x, y) = 0\}$. SDF is used in the level set framework to avoid "steep and flat gradients as well as rapidly changing features" as much as possible (Osher & Fedkiw, 2002). In this thesis, we define that ϕ is negative inside the contour and positive outside the contour.

Figure 2.10: Different types of representation for contours: The left image shows the original image of a maxillary anterior tooth, the red contour segment the tooth out from the background; The middle image shows the binary image of the segmented tooth; The right image shows the SDF of the contour of the tooth

Since the SDF is used to represent the contour in level set method, it is numerically necessary to keep the evolving function close to it. A new variational level set method is proposed by Li *et al.* (2005) to evolve the SDF ϕ without re-initialization. The energy functional of Li's method is given as follows:

$$J_{Li}(\phi) = \lambda_1 \int_\Omega \frac{1}{2}(|\nabla\phi| - 1)^2 dxdy + \lambda_2 \int_\Omega g\delta(\phi)|\nabla\phi| dxdy + \lambda_3 \int_\Omega gH(-\phi)dxdy \tag{2.6}$$

where $\lambda_1 > 0$, $\lambda_2 > 0$, λ_3 are weight coefficients, ∇ is the gradient operator, Ω is the domain of the 2D image, δ is the univariate Dirac function, and H is the Heaviside function

$$H(z) = \begin{cases} 1, \text{ if } z \geq 0 \\ 0, \text{ if } z < 0 \end{cases} \tag{2.7}$$

$$\delta(z) = \frac{d}{dz} H(z) \tag{2.8}$$

In practice, smoothed versions of both Dirac function and Heaviside function

are used:

$$H_\varepsilon(z) = \begin{cases} 1, & \text{if } z > \varepsilon \\ 0, & \text{if } z < -\varepsilon \\ \frac{1}{2}\left[1 + \frac{z}{\varepsilon} + \frac{1}{\pi}\sin\left(\frac{\pi z}{\varepsilon}\right)\right], & \text{if } |z| \leq \varepsilon \end{cases} \tag{2.9}$$

$$\delta_\varepsilon(z) = \begin{cases} 0, & \text{if } |z| > \varepsilon \\ \frac{1}{2\varepsilon}\left[1 + \cos\left(\frac{\pi z}{\varepsilon}\right)\right], & \text{if } |z| \leq \varepsilon \end{cases} \tag{2.10}$$

We use the smoothed Dirac function and the smoothed Heaviside function with $\varepsilon = 1.5$ for all our experiments in the thesis.

There are two advantages to use the active contour for medical image segmentation: (1) It is self-adapting to search for the minimal energy state; (2) the evolution of the contour can be controlled using self-designed external forces according to different medical applications. One of the disadvantages of the active contour method is the selection of a stable parameter value. The performance of the active contour may be sensitive to initialization of the contour.

2.3.2.7 Active shape/appearance models

Active shape models (ASM) are statistical shape models (SSM) of the shapes of objects that evolve iteratively to approach the targeted object in the image. It works as follows: (1) Search the neighbors of each point for a better position (usually near the edges of the image) for that point; and (2) update the model parameters to better fit to these new positions.

ASM has been widely applied in medical image segmentation problems,

e.g., the segmentation of heart ventricles (Cootes *et al.*, 1995), mandibles from low-dose CT data (Lamecker *et al.*, 2006) and maxilla from cone-beam computed tomography (Chang *et al.*, 2013).

However, one obvious disadvantage of ASM is that it only uses shape features of the ROI. The Active Appearance Model (AAM) is a more generalized version of ASM, which uses all the information (such as grey-level appearance and texture) in the region of interest (ROI) rather than just the shape information.

AAM has also been widely applied in medical segmentation problems, e.g., the segmentation of the knee from MRI (Cootes *et al.*, 1998), vertebral morphometry (Roberts *et al.*, 2003) and liver (Beichel *et al.*, 2001).

However, AAM shows some disadvantages in some practical applications. These disadvantages are mainly: (1) the tedious training process to build the statistical models of the objects, (2) failure to work in real-time systems, and (3) the lack of robustness under some circumstances.

Chapter 3

Mandibular body segmentation from magnetic resonance imaging

In this chapter, we present a two-stage rule-constrained seedless region growing approach for mandibular body segmentation in MRI. The proposed approach can solve one subproblem of bone segmentation in MRI as we described in Section 2.2.2. The details of the algorithm will be presented in the following sections.

3.1 Introduction

Magnetic resonance imaging (MRI) presents substantial health advantages to the patient, compared to multi-slice computed tomography (MSCT) and dental cone-beam computed tomography (CBCT) for dental and maxillo-facial imaging prescriptions. MRI has no ionizing radiation and provides visualization of internal soft tissue anatomy (such as muscles and cartilaginous joints) with a

high degree of clarity and detail that computed tomography does not possess. While MR imaging is not usually indicated for imaging of skeletal hard tissues, the value and usefulness of MR imaging can be enhanced with methods to define the bone shadows from the MR image field of view. This dimension of MR imaging is of particular importance in (1) children with the congenital defect of cleft lip and palate who require serial imaging of the internal facial structures to monitor developmental changes following early surgical reparative procedures, and (2) in the assessment of the pharyngeal airway and muscles of adults diagnosed with obstructive sleep apnea (OSA). While dental CBCT offers high quality images of the facial skeleton, it does so at the expense of the health of children; cumulative radiation exposures from serial CBCT prescriptions in children with cleft anomalies pose significant risks of developing stochastic effects. From the MR images of the neuromuscular pharyngeal anatomy of patients with OSA, computer-based methods which help visualize the size and shape of the mandible and the maxilla enable the treating clinician to prescribe appropriate strategies to manage the medical condition without the addition of ionizing radiation.

The segmentation of the shape of bones from MRI is a challenging engineering proposition due to several factors. Firstly, the partial volume effect and movement by the patient during MR imaging may result in poor image quality. Secondly, missing bone structures and the mixture of bone with air often exist in MR images. Fig. 3.1 shows the differences between an MSCT and MR image for the body of the mandible. Two types of bone tissue exist in the mandibular body: the trabecular bone (TB) and the cortical bone (CB) (Fig. 3.2). In MR images, the trabecular bones are seen as connected to soft tissues external to the

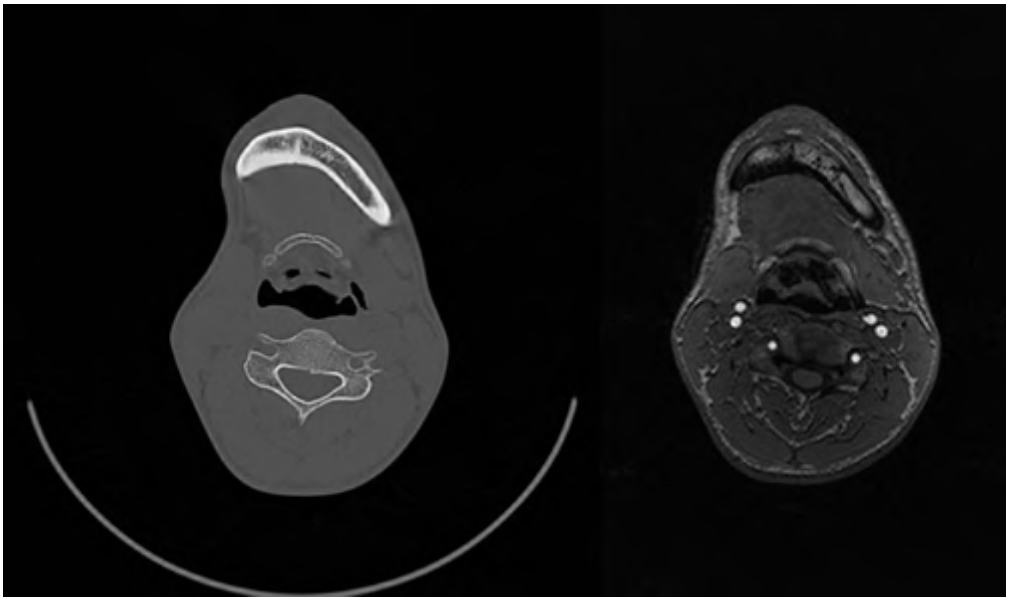

Figure 3.1: Image of the mandible from the same subject: CT (left), T1-Weighted MRI (right).

mandible where the cortical bones are missing or at regions where the cortical bones are unclear.

3.1.1 Bone segmentation in MRI

A number of MRI segmentation techniques to derive the shape of bones have been reported (Dokldal *et al.*, 2003; Park & Lee, 2009; Sadananthan *et al.*, 2010; Schmid *et al.*, 2011; Shan *et al.*, 2002; Smith, 2002; Zhang *et al.*, 2001). Rifai *et al.* (2000) used a deformable model to segment the skull in MRI volumes. Zoroofi *et al.* (2001) applied a histogram-based thresholding method, 3D-morphological operations, oblique data reconstruction and ellipse fitting to segment a region of non-vital bone from the femoral head in MRI. Dogdas *et al.* (2005) combined thresholding and a series of mathematical morphological operations to generate models of the skull, the scalp, and the brain. Lorigo *et al.*

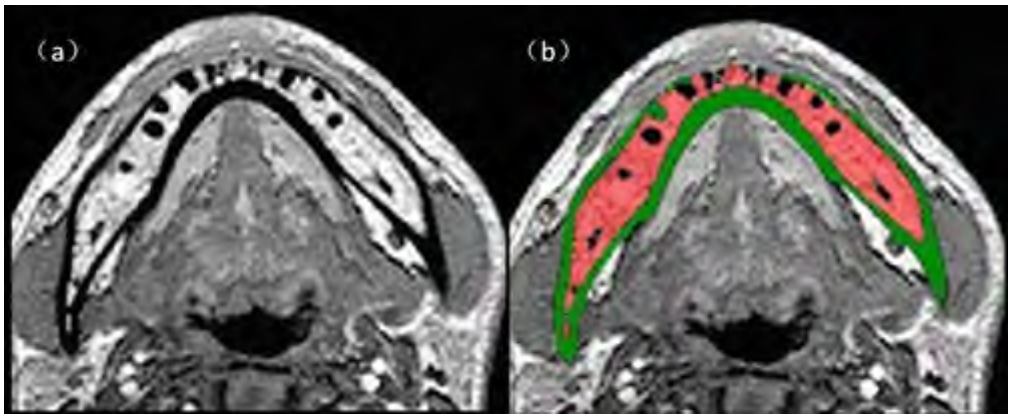

Figure 3.2: TB and CB are on a typical MRI slice: (a) raw mri image in axial view; (b) the red region is TB and the green region is CB.

(1998) proposed a texture-based geodesic active contour method to segment the knee in clinical MRI. Bourgeat *et al.* (2007a) used features extracted from the phase of the MRI to improve bone segmentation which is typically done using magnitude features. More recently, Schmid *et al.* (2011) proposed a robust multi-resolution statistical shape model algorithm with an adapted initialization to address the segmentation of MRI bone images. However, no study on the segmentation of the mandible from MR images has been reported.

3.1.2 Region growing and medical image segmentation

The seeded region growing (SRG) method was introduced by Adams & Bischof (1994) who used a rough multilevel thresholding technique to merge different anatomical regions in a CT image of a human head into three different classes - bone, soft tissue and air. Unfortunately, 2D or 3D region growing methods applied alone cannot lead to an accurate segmentation of a complete region of interest (ROI) from CT or MRI images. These methods are prone to cause "leakage" where the surrounding area has similar intensity values with the ROI

(Fabijaska, 2009; Park & Lee, 2009). To overcome this problem of "leakage", knowledge of human anatomy or technical rules are used as constraints on the iterative process or as stopping criteria of region growing (Fabijaska, 2009; Kim *et al.*, 2006; Park & Lee, 2009; Sonka *et al.*, 1996). Kim *et al.* (2006) proposed an automatic navigation path generation based on a two-stage adaptive region-growing for virtual angioscopy. They used 2D region growing to select a small ROI followed by applying a 3D growing technique to obtain a larger refined region under some predefined criteria. Park & Lee (2009) constrained region growing by using general knowledge of brain anatomy. Using a range of thresholds instead of a specific threshold, their method has been shown to detect more details of the brain than the basic region growing algorithm. In adopting the method of Park and co-workers to the facial region, this study aims to derive the shape of the body of the human mandible from magnetic resonance (MR) images of the head using an automated three-dimensional (3D) method of image segmentation.

3.2 Materials and Methods

3.2.1 Materials

Approval for the MR imaging of adult volunteers was given by the National Healthcare Group Domain Specific Review Board. The subsequent image processing and modeling of the MR images were approved by the National University of Singapore Institutional Biosafety Committee. All persons gave their informed consent prior to their inclusion in the study.

Twelve magnetic resonance image data sets were obtained using a 1.5 Tesla Siemens MR scanner with a T1 fast low angle shot (FLASH) imaging sequence (1mm thickness, 512×352 matrix with a resolution of 0.4883mm×0.4883mm, 240mm FOV, TR=9.93ms, TE= 4.86ms).

3.2.2 Method

A two-stage rule-constrained region growing approach is applied to the MR image data sets to determine the shape of the body of the mandible. The sequence starts with 3D seedless region growing for the purpose of detecting a large portion of the trabecular bone[1] (TB) regions of the mandible after an initial threshold. This stage is followed by a rule-constrained 2D segmentation of each MR axial slice to merge the remaining portions of the TB regions previously undetected at lower intensity levels. The preceding two steps were repeated with different thresholds to detect the cortical bone[2] (CB) regions. The pen-ultimate step involved the merging of TB and CB regions to further define the shape of the body of the mandible. A series of morphological processes rounds up this approach to complete the definition of the mandibular body.

3.2.2.1 Detecting TB regions

TB regions in a single axial MR slice are difficult to segment in 2D slices because (1) they are interspersed with the CB regions; (2) the intensity levels vary too substantially to be detected using the single threshold and adaptive threshold techniques; (3) they appear to be connected to regions external to the body of

[1] Trabecular bone (also called cancellous or spongy bone) fills the interior of the bone.
[2] Cortical bone is the hard outer layer of bones composed of compact bone tissue.

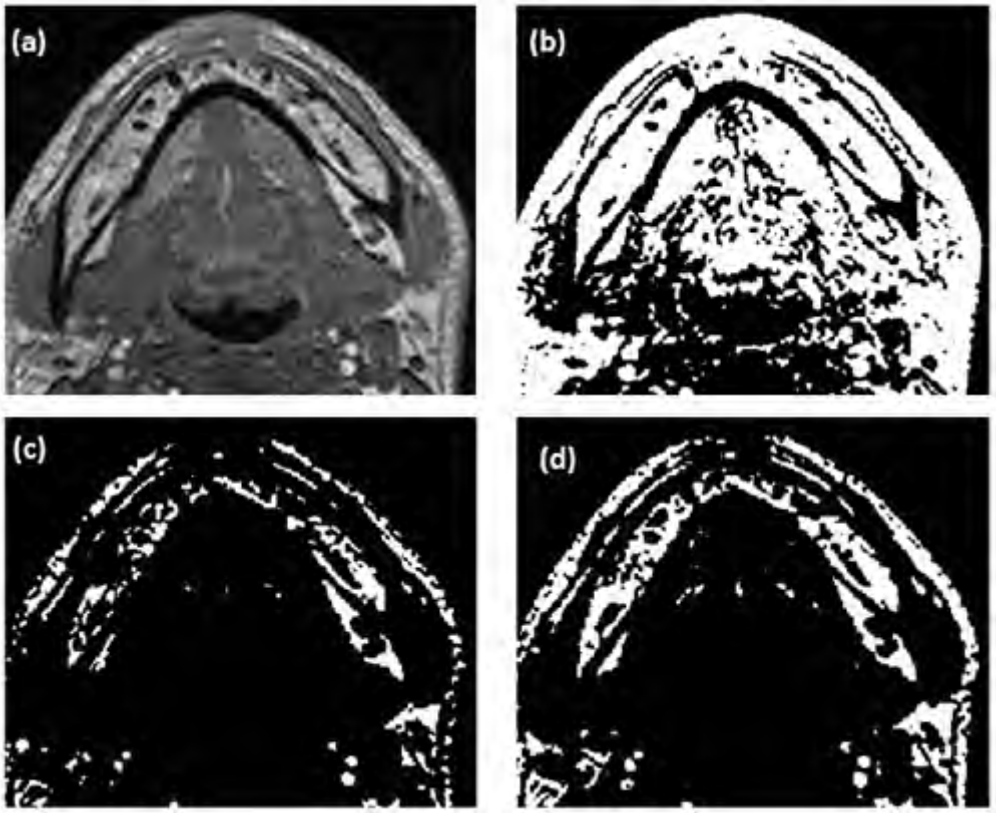

Figure 3.3: TB segmentation difficulties: (a) original image (b) binary image after a low intensity thresholding, TB is connected with the outside regions (c) binary image after a high intensity thresholding, TB is separated into too many small parts (d) binary image after proper initial thresholding.

the mandible in areas where the CB is missing. Thus a proper threshold has to be selected to detect the raw unconnected TB regions. A low initial threshold might cause the TB to connect with regions external to the mandible, while a high threshold might result in the TB regions splitting into too many fragmented parts (Fig. 3.3). The method on how to find the proper threshold is described in Section. 3.2.2.3.

3.2.2.2 Connecting raw TB regions

Although the binary images obtained after initial thresholding are still fragmented in 2D slices, they are actually connected in 3D. Fig. 3.4 shows how TB regions are connected with each other in consecutive slices. More importantly, we do not have to select a seed point manually. Instead we can use the anatomical information that the raw mandibular body TB obtained after the initial threshold is the second largest connected 3D region in the image. The 3D model of the connected largest region and TB region is shown in Fig. 3.5.

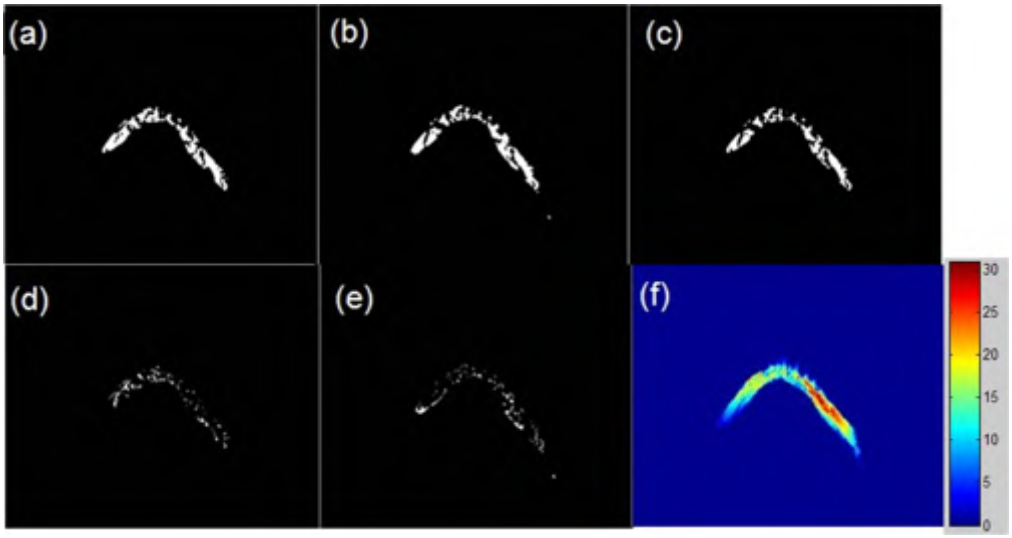

Figure 3.4: A sample to show connections between consecutive slices: (a) TB in the 12th slice (b) TB in the 13th slice (c) intersection between the two slices (d) points exist only in the 12th slice (e) points exist only in the 13th slice (f) TB intersection times in different slices (the colorbar shows how many times each point in slices intersects with the corresponding point in its neighboring slices).

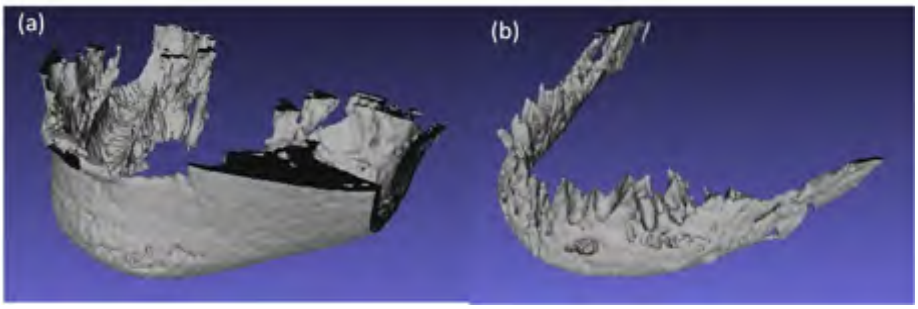

Figure 3.5: 3D model of the connected components after initial threshold: (a) The largest connected component in 3D (b) The second largest connected component (TB) in 3D.

3.2.2.3 Refining TB region

Since only a fraction of TB regions are segmented from the MR axial slices from regions with relatively high image thresholding intensities, the next step is to detect other TB regions in each slice with lower intensities. As it is easier for the TB region to "leak out" in 3D compared to 2D, the 3D region growing method is not used here to evolve the TB region. Instead, the method proposed by Park & Lee (2009) is adopted to merge the remaining TB regions in each slice. It initially divides each slice into two regions: region ROI (R_R), region of non-ROI (R_N) by the initial threshold. To avoid the connection between the two regions, the algorithm introduces an additional region named "undetermined region" (R_U) to serve as a "fire wall" between the ROI and the outside regions. The initial undetermined region is set to null. Throughout the region growing process, there will be three regions: R_R, R_N and R_U. The next step is to evolve the three regions with the following steps:

- Select a upper bound T_u and lower bound T_l for the intensity range. De-

crease the intensity from T_u one by one until T_l. Each time when the intensity decrease one unit, additional points will appear in each slice. The algorithm will assign the new added points into the three regions by the voxel assignment rules (VAR).

- Assign some of these components of R_U to R_R or R_N according to the component assignment rules (CAR).

We will use the following notation in the descriptions of VAR and CAR:

- t is the threshold value in each iteration.
- $R_R(t)$ is the ROI region when the threshold is t; $R_N(t)$ is the region of non-ROI when the threshold is t; $R_U(t)$ is the undetermined region when the threshold is t.
- $P(t)$ is the ensemble of all the new points appear in the slice due to the decreasing of the threshold from $t+1$ to t and p is one element of this ensemble.
- q_c is one connected component that belongs to region $R_U(t)$

VAR are rules given by the following conditions:

1. If p is connected to $R_N(t)$ with 4-connectivity, we assign it to $R_N(t)$.
2. If condition 1 does not hold, and if p is connected to $R_R(t)$, then we assign it to $R_R(t)$.
3. If neither of condition 1 nor 2 holds, then we assign it to $R_U(t)$.

CAR are rules given as the following conditions:

1. If q_c is connected to $R_N(t)$, then we assign it to $R_N(t)$.

2. If condition 1 does not hold, and if q_c is connected to $R_R(t)$, then we assign it to $R_R(t)$.

3. If neither condition 1 nor 2 holds, then it still belongs to $R_U(t)$.

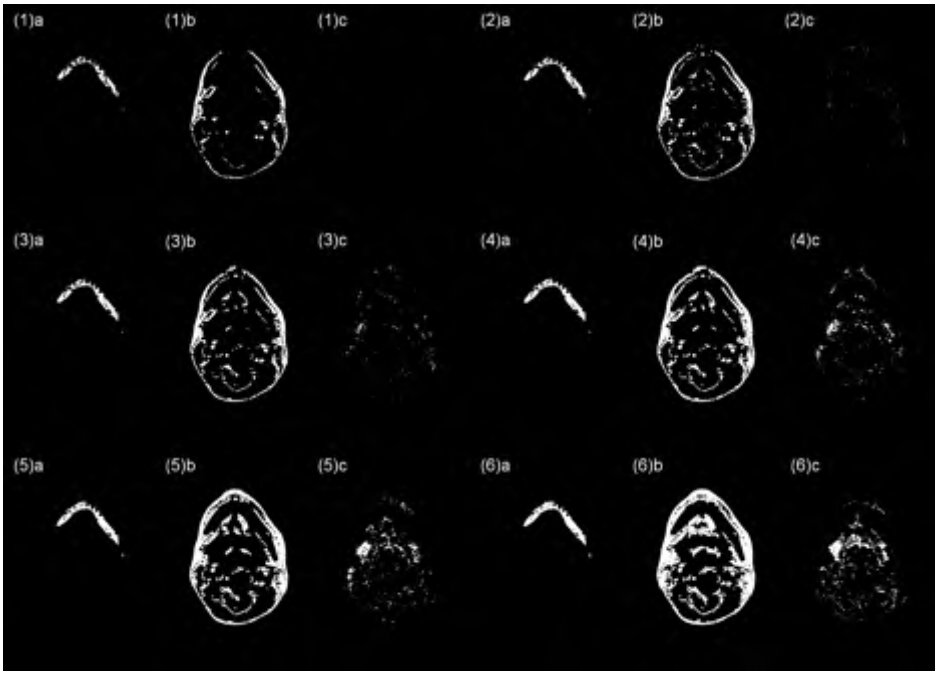

Figure 3.6: Detect TB by decreasing the threshold from $t = 0.45 \times$ MI to $t = 0.45 \times$ MI $- 100$: (a) $R_R(t)$; (b) $R_N(t)$; (c) $R_U(t)$. (1) threshold value $t = 0.45 \times$MI. (2) $t = 0.45 \times$MI$- 20$. (3) $t = 0.45 \times$MI$- 40$. (4) $t = 0.45 \times$MI$- 60$. (5) $t = 0.45 \times$ MI $- 80$. (6) $t = 0.45 \times$ MI $- 100$.

For TB segmentation, the upper bound threshold T_u was not set as a fixed value at the beginning. Instead we set a possible range for T_u from 0.4×MI to 0.6×MI, where MI is the maximum intensity of the data set. The value of T_u was determined by selecting a best performance threshold empirically, with T_l fixed at $T_l = T_u - 100$. The region growing procedure for one slice is shown in

Figure 3.6. Using the rule-constrained 2D region growing method, we gradually detect more details of the TB regions lying at relatively lower intensity levels.

3.2.2.4 Segment CB of the mandibular body

Similar to the above procedures of TB segmentation, we use the following steps to segment CB of the mandibular body:

1. Detect raw CB regions in different slices.
2. Connect raw CB regions in different slices.
3. Refine CB regions with 2D rule-constrained region growing.

CB regions can be easily segmented from the background because their intensity levels are much lower than those of TB regions and the external soft tissues. Finally the segmentation of CB regions will not encounter the "leak out" problem. For CB segmentation, the thresholds are fixed at $T_u = 180$, $T_l = T_u - 100$.

3.2.2.5 Combine TB and CB regions

After determining the TB and CB regions, morphological dilation is applied to the TB region to ensure the connection between TB and CB. The structuring element applied here is the 5-connected neighborhood structuring element. A hole-filling algorithm is then used to fill the holes in each axial slice.

3.2.3 Validation

The manual segmentation of each mandibular body performed by a clinician serves as the ground truth. The accuracy is validated by comparing automatic

segmentation results with manual segmentation results. The Jaccard and the Dice indexes are used to assess the agreement between automatic and manual segmentation approaches. These two metrics are defined by:

$$Jaccard : J(V_1, V_2) = \frac{|V_1 \bigcap V_2|}{|V_1 \bigcup V_2|}, \tag{3.1}$$

$$Dice : D(V_1, V_2) = \frac{2|V_1 \bigcap V_2|}{|V_1| + |V_2|}. \tag{3.2}$$

where V_1 represents the voxel set of automatic segmentation results and V_2 represents the voxel set of the ground truth.

There are 21 candidate pairs of T_u and T_l. Accordingly, each MR image data set consists of 21 candidate combinations of TB and CB regions. The best performance candidate pairs will be selected by choosing the pair with the highest Jaccard or Dice index value.

The mean surface distances (MSD) are calculated to assess the qualities of 3D models obtained by different algorithms. A second time manual segmentation is applied to show the variability of the manual segmentation using the Jaccard and Dice indexes compared with the first time manual segmentation.

3.3 Experiments and Results

The performance results were investigated when $T_u = \alpha \times$ MI, where α is a coefficient that ranges from 0.4 to 0.6 with a step of 0.01. T_l is fixed as $T_l = T_u - 100$ (Table 3.1 and Table 3.2). As discussed in subsection 3.2.2.1, if T_u is too small, the segmented image suffers from the "leak out" (LO) problem, while

if T_u is too large, the segmented image will be fragmented and suffers from the "not connected" (NC) problem. The proper values of T_u should be selected to avoid LO and NC. We can easily find the proper range of T_u, by setting a threshold, say 0.8, on the Jaccard index (JI). If the value of JI is smaller than 0.8, the threshold will lead to either the LO or NC problem. The proper range of T_u usually lies in the middle of the interval [0.4,0.6]. Then if T_u is less than the range of proper thersholding it is labeled by LO or else it is labeled by NC.

The best performance T_u can be found in Table 3.1 by checking which value of C has the largest JI.

3.3.1 Comparison study

The proposed method is compared with the conventional region growing (CRG) method. The parameters selected for TB are given as follows: the initial threshold T_u is fixed at $T_u = \alpha \times \text{MI}$ for the proposed method; in the CRG method, the single threshold t is fixed at $t = \alpha \times \text{MI}$, where α is selected from α in Table 3.1 with the largest JI.

The proposed method is then compared with a user-guided 3D level set method installed in ITK-SNAP 2.2 (Yushkevich *et al.*, 2006). Initially, manually selected 3D bubbles are placed in several TB regions. The active contours then evolve depending on the edge and region information. Finally, the evolution process stops when a proper shape of the mandibular body is obtained. The level set method may cause a "leak out" problem in segmentation as shown in Fig. 3.7.

Table 3.1: Jaccard index (JI) of segmentation results on 12 data sets with variable T_u.

Parameters selection for TB: $T_u = \alpha \times$ MI[1] with $T_l = T_u - 100$												
Dataset	1	2	3	4	5	6	7	8	9	10	11	12
α												
0.400	LO[2]	LO	LO	LO	LO	LO	LO	LO	LO	LO	LO	LO
0.410	LO	LO	LO	LO	LO	LO	LO	LO	LO	LO	LO	LO
0.420	LO	LO	LO	LO	LO	LO	0.948	LO	0.926	LO	LO	LO
0.430	0.961	LO	LO	LO	LO	LO	0.951	LO	0.927	LO	LO	0.913
0.440	0.960	0.958	LO	0.959	0.975	LO	0.949	LO	0.927	LO	0.932	0.909
0.450	0.959	0.956	0.966	0.953	0.974	0.978	0.950	0.976	0.927	0.975	0.960	0.903
0.460	0.959	0.952	0.966	0.952	0.974	0.978	0.951	0.975	0.926	0.974	0.960	0.895
0.470	0.957	0.949	NC	0.949	0.973	0.977	0.948	0.974	0.925	0.974	0.961	0.885
0.480	0.955	0.940	NC	0.951	0.970	0.974	0.946	0.974	0.923	0.973	0.957	0.864
0.490	0.953	0.930	NC	0.955	NC	0.971	0.945	0.971	0.922	0.972	0.956	NC
0.500	0.950	0.918	NC	NC	NC	0.970	0.940	0.968	0.920	0.972	0.950	NC
0.510	0.941	0.906	NC	NC	NC	0.966	0.938	0.965	0.917	0.971	0.948	NC
0.520	0.936	NC	NC	NC	NC	0.958	0.936	0.961	0.912	0.970	0.943	NC
0.530	NC[3]	NC	NC	NC	NC	0.956	0.935	0.959	NC	0.968	0.935	NC
0.540	NC	NC	NC	NC	NC	NC	0.929	0.951	NC	0.967	0.932	NC
0.550	NC	NC	NC	NC	NC	NC	0.926	0.932	NC	0.967	NC	NC
0.560	NC	NC	NC	NC	NC	NC	0.922	NC	NC	0.964	NC	NC
0.570	NC	NC	NC	NC	NC	NC	0.918	NC	NC	0.963	NC	NC
0.580	NC	NC	NC	NC	NC	NC	NC	NC	NC	0.962	NC	NC
0.590	NC	NC	NC	NC	NC	NC	NC	NC	NC	0.961	NC	NC
0.600	NC	NC	NC	NC	NC	NC	NC	NC	NC	0.957	NC	NC

[1] MI : Maximum intensity of the image data

[2] LO: Leak out

[3] NC: Not connected

[4] The largest JI of each dataset is boxed. Using the corresponding C value, the optimal value of T_u can be calculated.

Table 3.2: Dice index of segmentation results on 12 data sets with variable T_u.

Parameters selection for TB: $T_u = \alpha \times$ MI[1] with $T_l = T_u - 100$												
Dataset	1	2	3	4	5	6	7	8	9	10	11	12
α												
0.400	LO[2]	LO	LO	LO	LO	LO	LO	LO	LO	LO	LO	LO
0.410	LO	LO	LO	LO	LO	LO	LO	LO	LO	LO	LO	LO
0.420	LO	LO	LO	LO	LO	LO	0.973	LO	0.962	LO	LO	LO
0.430	0.980	LO	LO	LO	LO	LO	0.975	LO	0.962	LO	LO	0.955
0.440	0.979	0.977	LO	0.979	0.987	LO	0.974	LO	0.962	LO	0.965	0.952
0.450	0.979	0.977	0.983	0.976	0.987	0.989	0.974	0.988	0.962	0.987	0.980	0.949
0.460	0.979	0.976	0.983	0.975	0.987	0.989	0.975	0.988	0.962	0.987	0.979	0.945
0.470	0.978	0.974	NC	0.974	0.986	0.988	0.973	0.987	0.961	0.987	0.980	0.939
0.480	0.977	0.969	NC	0.975	0.985	0.987	0.972	0.987	0.960	0.986	0.978	0.927
0.490	0.976	0.964	NC	0.977	NC	0.985	0.972	0.985	0.959	0.986	0.977	NC
0.500	0.974	0.957	NC	NC	NC	0.985	0.969	0.984	0.959	0.986	0.974	NC
0.510	0.970	0.951	NC	NC	NC	0.983	0.968	0.982	0.957	0.985	0.973	NC
0.520	0.967	NC	NC	NC	NC	0.979	0.967	0.98	0.954	0.985	0.971	NC
0.530	NC[3]	NC	NC	NC	NC	0.978	0.966	0.979	NC	0.984	0.966	NC
0.540	NC	NC	NC	NC	NC	NC	0.963	0.975	NC	0.983	0.965	NC
0.550	NC	NC	NC	NC	NC	NC	0.961	0.965	NC	0.983	NC	NC
0.560	NC	NC	NC	NC	NC	NC	0.959	NC	NC	0.982	NC	NC
0.570	NC	NC	NC	NC	NC	NC	0.957	NC	NC	0.981	NC	NC
0.580	NC	NC	NC	NC	NC	NC	NC	NC	NC	0.981	NC	NC
0.590	NC	NC	NC	NC	NC	NC	NC	NC	NC	0.98	NC	NC
0.600	NC	NC	NC	NC	NC	NC	NC	NC	NC	0.978	NC	NC

[1] MI : Maximum intensity of the image data

[2] LO: Leak out

[3] NC: Not connected

[4] The largest DI of each dataset is boxed.

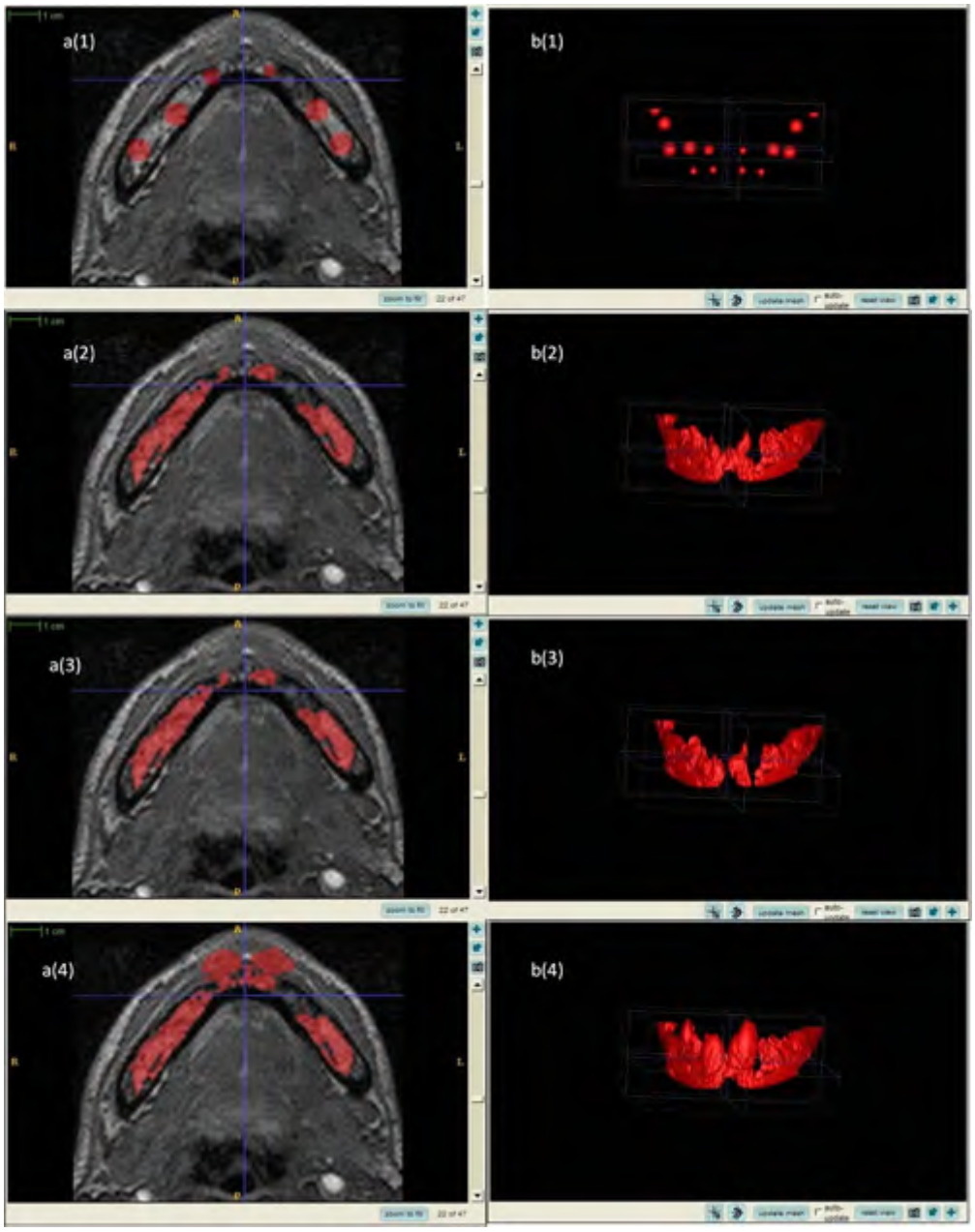

Figure 3.7: Leak out problems in 3D level set method. a(1)-a(4) are shown in the axial view. a(1): initial regions defined manually; a(2): evolved regions after 100 iterations; a(3): evolved regions after 200 iterations; a(4): evolved regions after 300 iterations; b(1)-b(4) are the segmented 3D shapes at corresponding iterations (shown in front view).

3.3.2 Results

The algorithm was tested on a desktop computer with an Intel(R) Core (TM) 2 Duo CPU 2.65 GHz and 2.72 GB memory. The program is implemented in Matlab 7.11.0 (R2010b) installed in Microsoft Windows XP Professional. The average time consumed for one experiment is 128 seconds with 99 seconds spent on segmentation of TB, 26 seconds lapsed for segmentation of CB and 3 seconds lapsed for the combination of TB and CB.

The examples of final segmentation results of the proposed method are provided in Fig. 3.8 (axial view). The 3D segmentation results of the proposed method, CRG and 3D level set are shown in Fig. 3.9

The comparison results between the proposed method, CRG and 3D level set are shown in Table 3.3. The mean accuracy of the second time manual segmentation is 0.998 ± 0.002 (0.998 is the mean value and 0.002 is the standard deviation) for Jaccard index (JI), 0.999 ± 0.001 for Dice index (DI). The large JI and DI means the variability of the manual segmentation is very small, and can be considered to be reliable. The mean accuracy of the proposed method is 0.958 ± 0.020 for JI, 0.979 ± 0.011 for DI, 0.204 ± 0.127mm for MSD. The mean accuracy of CRG is 0.782 ± 0.080 for JI, 0.876 ± 0.053 for DI, 0.417 ± 0.073mm for MSD. The mean accuracy of the 3D level set method is $0.874 \pm 0.0.051$ for JI, 0.645 ± 0.306 for DI, 0.645 ± 0.306mm for MSD. The proposed method shows an improvement in accuracy over the CRG and 3D level set methods.

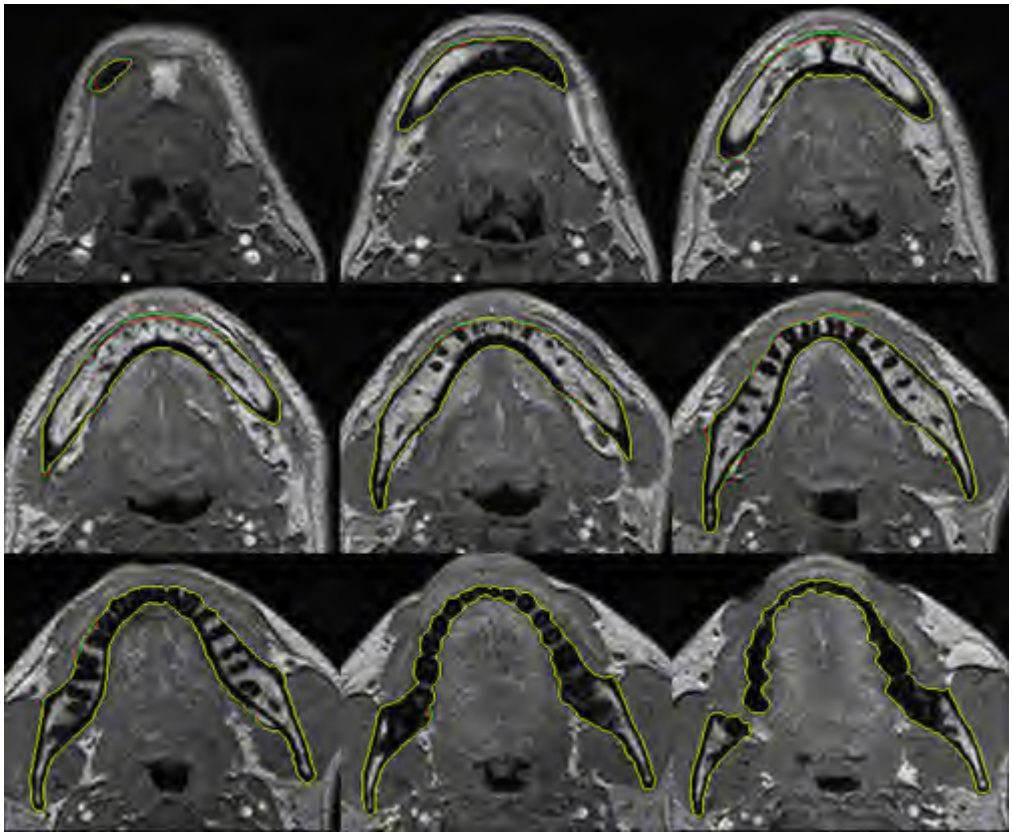

Figure 3.8: Segmentation results of the proposed method: The green lines are the ground truth; the red lines are automatic segmentation results; yellow lines are the intersections between the ground truth and automatic segmentation results.

Table 3.3: Performance comparison between the proposed method, CRG and 3D Level set.

		Proposed method			CRG			Level set			SMS[1]	
	α	Jaccard	Dice	MSD[2](mm)	Jaccard	Dice	MSD	Jaccard	Dice	MSD	Jaccard	Dice
1	0.43	0.961	0.980	0.209	0.760	0.864	0.347	0.704	0.827	0.532	0.995	0.997
2	0.44	0.958	0.977	0.232	0.638	0.779	0.465	0.782	0.877	0.716	0.996	0.998
3	0.45	0.966	0.983	0.087	0.830	0.907	0.49	0.828	0.906	0.374	0.997	0.998
4	0.44	0.959	0.979	0.187	0.808	0.894	0.359	0.806	0.893	0.479	0.999	0.999
5	0.44	0.975	0.987	0.095	0.885	0.939	0.411	0.886	0.940	0.571	1.000	1.000
6	0.45	0.978	0.989	0.073	0.777	0.874	0.297	0.864	0.927	0.473	1.000	1.000
7	0.43	0.951	0.975	0.340	0.828	0.906	0.379	0.800	0.889	0.481	0.999	1.000
8	0.45	0.976	0.988	0.064	0.824	0.903	0.421	0.826	0.905	0.572	0.999	1.000
9	0.44	0.927	0.962	0.355	0.791	0.883	0.380	0.757	0.862	1.285	0.999	1.000
10	0.45	0.975	0.987	0.090	0.856	0.923	0.428	0.613	0.760	1.268	0.999	1.000
11	0.47	0.961	0.980	0.268	0.768	0.869	0.457	0.814	0.898	0.464	0.997	0.999
12	0.43	0.913	0.955	0.443	0.621	0.767	0.571	0.689	0.816	0.531	0.999	0.999
	mean	0.958	0.979	0.204	0.782	0.876	0.417	0.781	0.874	0.645	0.998	0.999
	SD[3]	0.020	0.011	0.127	0.080	0.053	0.073	0.078	0.051	0.306	0.002	0.001

[1] SMS :Second manual segmentation
[2] MSD : Mean surface distance
[3] SD: Standard deviation

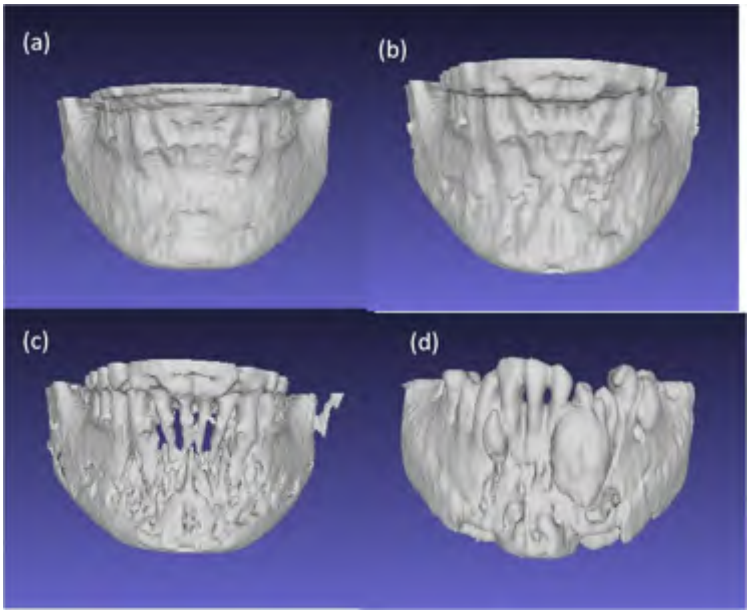

Figure 3.9: 3D segmentation results of the different methods: (a) manual segmentation (ground truth); (b) segmentation result of the proposed method; (c) segmentation result of CRG; (d) segmentation result of 3D level set

3.4 Discussion

3.4.1 Analysis of experimental design

The proposed two-stage rule constrained seedless region growing approach is different from the method introduced by Park & Lee (2009). Segmentation of brain MR images requires the ROI to be already connected in 2D after initial thresholding. In contrast, mandibular body segmentation of the TB regions in the mandibular body commonly leaves the TB regions separated in each slice after an initial thresholding. Thus Park & Lee (2009)'s method cannot be directly used in mandibular body segmentation because it is not feasible to manually select the seed point in each MR axial slice. Hence, using the knowledge of the spatial location of TB, the segmented TB regions become the second largest

connected component after initial thresholding.

A simple single threshold method is vulnerable to either over-segmentation or under-segmentation. In the mandibular body segmentation from MRI, both situations may happen due to the anatomical features of the mandibular body and the image quality of bone tissues from the MRI. Park's brain segmentation experiments fixed both the T_u and T_l values. However, in mandibular body segmentation, a fixed selection of T_u value may cause either an over-segmentation problem or an under-segmentation problem. Hence, to find the best T_u value, the present study sets a fixed range of testing values and selected the best performance value as the final threshold selection. The selection of T_l is much less important and we set it as a function of T_u instead.

3.4.2 Comparison of current and previously published results

The reason why the accuracy of CRG is lower is that it can only find a relative smaller portion of the TB region. The 3D level set easily causes the leak-out problem because it does not work well when TB has similar intensity values as the surrounding regions. This similarity causes the detected active contour to expand beyond the TB region and develop into a big bubble.

3.4.3 Clinical significance

The ability to derive an accurate shape of the body of the mandible from the non-ionising radiation imaging modality of MRI presents to clinicians a value-added visualization option of viewing both the hard and soft tissues in one visual environment. Spatial relationships between the soft tissue muscles (masticatory

and pharyngeal muscles) and the mandibular body can be determined efficiently without the need for additional volumetric imaging with CBCT to obtain skeletal information when high definition skeletal information is unnecessary. Patients who have undergone MR imaging but do not require CT imaging of the face stand to benefit from this approach without the need for x-ray radiation from CBCT or MSCT imaging. While the two-stage rule-constrained seedless region growing approach generated realistic shapes of the mandibular body, additional work is needed to generate the shapes of the thinner ascending mandibular ramus with its coronoid process and the condylar anatomy from MR imaging.

The three-dimensional shape of the mandibular body obtained from MR imaging is a first step to understanding the three-dimensional spatial relationship of the position and morphology of the mandible to the morphology and dimension of the airway. When applied to the study of patients with OSA who will need mandibular advancement methods to manage the OSA, MR imaging at the pre-treatment, in-treatment, and post-treatment phases provide the visual and dimensional information of the mandibular body and airway for analyses which could form the basis for treatment-specific effectiveness. This application eliminates the associated risks of radiation in children and adults with OSA.

3.5 Conclusion

This chapter presents a two-stage rule-constrained seedless region growing image processing approach for segmentation of the body of the mandible. The proposed framework starts with an initial thresholding, followed by a 3D seedless region growing algorithm to detect a large portion of the TB regions of the

mandible. This stage is followed with a rule-constrained 2D segmentation of each MR axial slice to merge the remaining portions of the TB regions with lower intensity levels. The two-stage approach was replicated to detect the CB regions of the mandibular body. The TB and CB regions detected from the preceding steps were merged and subjected to a series of morphological processes for completion of the mandibular body region definition. The experimental results have demonstrated that our method is able to prevent the leakage problem and is more accurate than the conventional region growing method and the level set method.

Chapter 4

A pilot study on the accuracy of reconstruction of mandibular shape

The results from experimental work carried out in Chapter 3 hypothesised that the mandible segmented from MRI accurately represented the anatomic shape of the subjects mandible. However, this hypothesis has not been validated before in the literature. In this chapter, we test the underlying hypothesis that the 3D anatomic model of the mandible reconstructed from in vivo magnetic resonance (MR) images was comparable to that obtained from CT imaging, which is commonly regarded as the reference standard for bone and hard tissue imaging. The details of this experimental study are presented in the following sections.

4.1 Introduction

For a more comprehensive study of the human mastication apparatus, an accurate three-dimensional (3D) representation of both the muscles and the mandible

has to be reconstructed from medical images. In practice, the shapes of the muscles are usually obtained from magnetic resonance imaging (MRI), while the shape of the mandible is usually obtained from computed tomography (CT). The use of multi-slice spiral computed tomography (MSCT) to obtain images of the jaws exposes patients to high amounts of ionizing radiation that pose a heightened risk of developing cancers (Loubele *et al.*, 2009; Rice *et al.*, 2007). In recent years, diagnostic cone beam computed tomography (CBCT) has gained popularity in dentistry for 3D imaging of facial bones due to its high spatial resolution for the bone tissues and subjecting patients to a relatively lower radiation exposure than MSCT (Kapila *et al.*, 2011; Loubele *et al.*, 2009; Scarfe *et al.*, 2006). However, CBCT still exposes patients to radiation (Palomo *et al.*, 2008), with children bearing a greater burden of these effects as they are likely to have repeated CBCT images taken during the course of treatment from childhood through adulthood. Ionizing radiation exposure to the facial structures poses risk of tissue damage to radio-sensitive tissues such as the thyroid gland, the salivary glands, the mucosal lining of the oral and naso-maxllary complex, the eye and the brain (ICRP, 2007).

In contrast with computed tomography, MRI employs no ionizing radiation to image soft and hard tissues (Burstein & Gray, 2003; Farina *et al.*, 2009). Diagnostic utility is dependent on the accuracy of MR imaging in representing anatomic structures (Burstein & Gray, 2003). In developing models that could accurately represent the anatomic structures, the technique of segmentation is critical to defining key anatomic structures in clinical images. While the accuracy of segmentation and 3D reconstruction for bone has been assessed extensively for CBCT and MSCT (Maret *et al.*, 2010), few studies on anatomic seg-

mentation have been carried out on MR images to derive hard-tissue anatomic models (Bourgeat *et al.*, 2007b; Schmid *et al.*, 2011). Currently, computed tomography (CT) (CT as CBCT or MSCT) scanners can produce higher resolution and better quality images for hard tissue compared to MRI scanners. However, we hypothesize that the 3D anatomic model of the mandible reconstructed from a living human's MRI data is comparable with that obtained from CT data.

In this investigation, the quality of 3D mandible models generated from MRI data was compared with the models generated from the corresponding CT data. The volumetric differences of the two models were measured using the CT model as the reference standard and the 3D surface differences were calculated and visualized for assessment of 3D reconstruction results. The bone dimension calculations were carried out for the body of the mandible at corresponding sites, which were automatically generated after a rigid registration of MRI and CT data sets.

4.2 Materials and Methods

4.2.1 Image data acquisition

Computed tomography (CT) scanning and magnetic resonance imaging (MRI) of the mandible were carried out on three healthy adult male volunteers aged 30 years, 47 years, and 25 years, with the data sets numbered 1 to 3, respectively (Table 4.1). All experimental procedures were approved by the Institutional Review Board of National University of Singapore. The raw image data were stored in DICOM format.

Table 4.1: Imaging devices and protocols of data acquisition in this study.

Data Set 1	Device	Spatial Resolution (mm)	Dimension
MSCT	SOMATOM Sensation, Siemens, Germany	$0.467 \times 0.467 \times 1$	$512 \times 512 \times 188$
MRI	MAGNETOM Symphony 1.5T, Siemens, Germany	$0.488 \times 0.488 \times 1$	$352 \times 512 \times 160$
Data Set 2			
CBCT	3D eXam 2nd Generation, KaVo, Germany	$0.3 \times 0.3 \times 0.3$	$768 \times 768 \times 576$
MRI	Signa HDx 1.5T, General Electric, USA	$1 \times 0.7 \times 1$	$256 \times 248 \times 256$
Data Set 3			
CBCT	Pax-Reve3D, Vatech, Korea	$0.25 \times 0.25 \times 0.25$	$592 \times 592 \times 600$
MRI	Signa HDx 1.5T, General Electric, USA	$1 \times 0.7 \times 1$	$256 \times 248 \times 256$

4.2.2 Image data format, segmentation, 3D registration and 3D reconstruction

The mandibles were segmented from the CT and MRI raw images data sets using a user-guided 3D active contour segmentation method implemented in ITK-SNAP (Yushkevich *et al.*, 2006) (Fig. 4.1).

After segmentation, pairs of the segmented mandibular images were exported in GIPL format for further comparison analyses. The surface point clouds of the paired segmented mandibular images were exported in STL format. The three pairs of point clouds were co-registered using the iterative closest point (ICP) algorithm[1] in Matlab (Zhang, 1994) (Fig. 4.2). The transformation ma-

[1]Iterative closest point is a general algorithm used to minimize the overall distance between

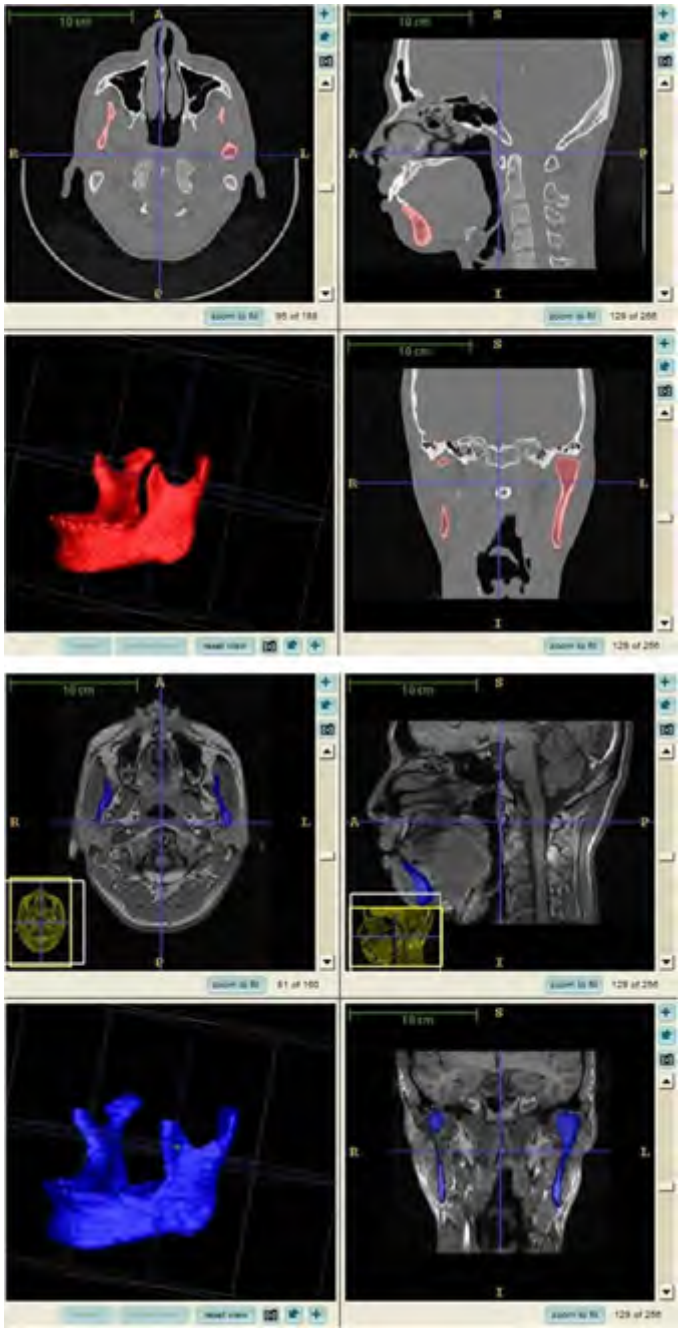

Figure 4.1: Segmentation result in CT and MRI. The top image is the segmentation result in CT and the bottom image is the segmentation result in MRI.

Figure 4.2: Registration result. The white points are the surface points of the mandibular model obtained from CT, and the green points are the co-registered surface points of the mandibular model obtained from MRI.

trix of the registration is used to transform the volumetric MR image into a new realigned matrix using the MedINRIA software (Fig. 4.3). The co-registered mandibular image data sets were then exported in GIPL format for further analyses.

4.2.3 Reliability of the segmentation

To test the intra-operator reliability of the segmentation, 3 data sets were re-segmented after an interval of 5 days and compared with former segmentation

two point clouds.

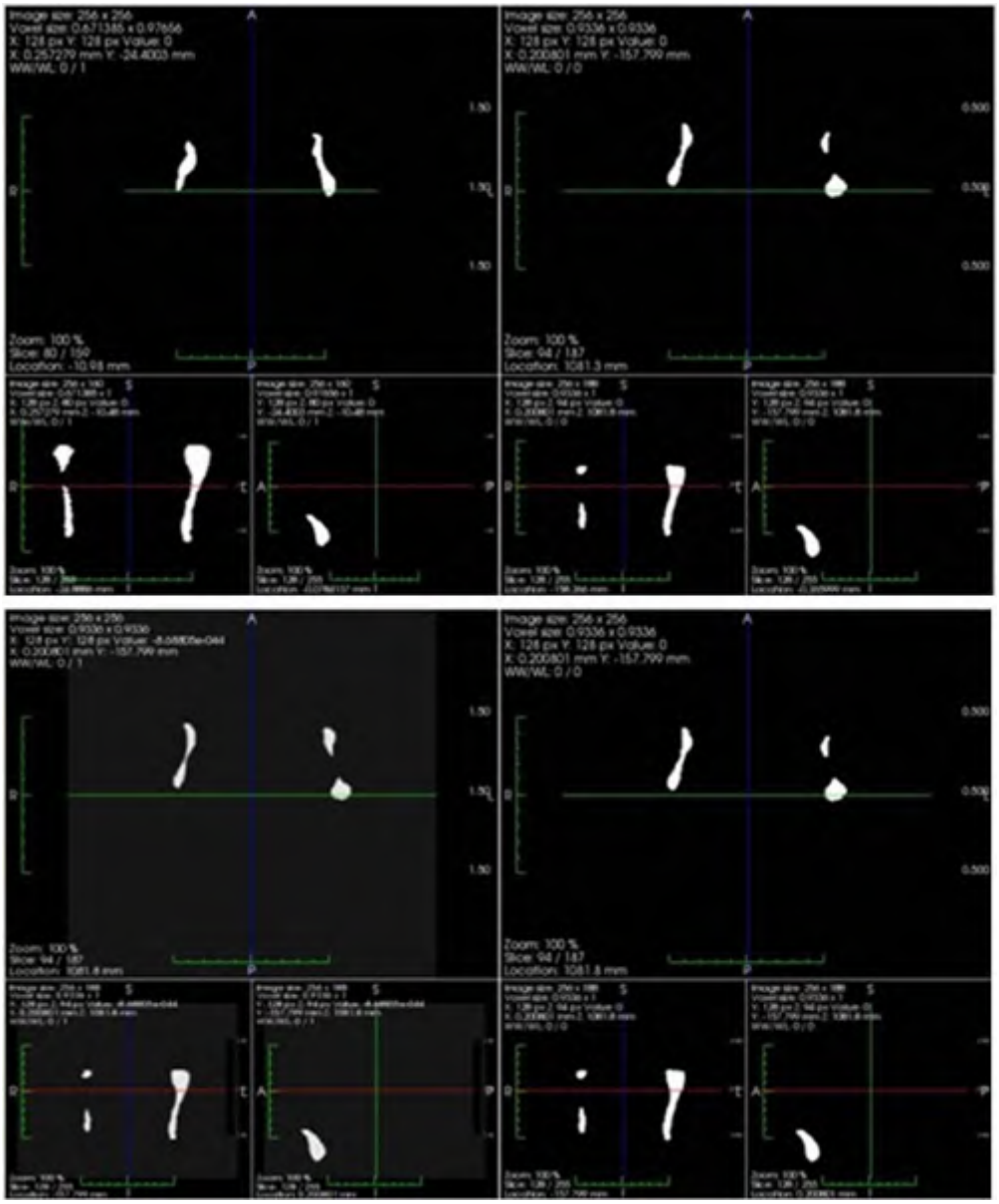

Figure 4.3: Realigned pairs of volumetric images before and after registration. The upper image shows the pairs of segmented images before registration. The lower image shows the pairs of segmented images after registration.

results, using Pearson correlation coefficient. The inter-operator reliability was also checked with 3 sets using Pearson correlation coefficient. Two operators were trained to use ITK-SNAP to segment before any operation was performed.

4.2.4 Volumetric calculation, volumetric similarity measurement, 3D surface difference calibration and visualization

The volumes of the co-registered mandibular images were calculated by multiplying the total number of voxels within the mandibular image volume and the voxel size. To determine if the volume of the mandibular model generated from MRI is similar to that obtained from CT scanning, the Dice index was used to assess the two-dimensional agreement of the paired volumes slice by slice (Dice, 1945). In Chapter 2, we have introduced the Dice index, which we restate here for convenience:

$$\text{Dice index} : D(V_1, V_2) = \frac{2|V_1 \bigcap V_2|}{|V_1 + V_2|} \tag{4.1}$$

where V_1 and V_2 represent the voxel set of the segmented mandibular image obtained from two different imaging modalities. This index measures the amount of overlap between the paired volumes, followed by a calculation of the distances between a large number of surface points of MRI models and the corresponding points of CT model. Using the 3D visualization toolbox in Matlab, a 3D color map was used to visualize these distances.

4.2.5 Determination of bucco-lingual thickness of mandibular bone shape

The bucco-lingual thickness of the shape of the body of the mandible, viewed in the axial plane, was carried out by calculating the distance of automatic generated points on paired slices. The automatic calculation procedures (a to f) are shown in Fig. 4.4, and the steps are described as follows:

- The shape of the mandible (Fig. 4.4b) was segmented from the CT image (Fig. 4.4a).
- Morphological functions in the Matlab software were used to find the one pixel thick skeleton of the binary mask of the segmented mandibular image.
- 2D connectivity analysis was applied to automatically remove the short branches in the skeleton (Fig. 4.4c) to obtain the representative curve of the mandibular shape (Fig. 4.4d).
- Equidistant points from the representative curve were sampled, and an orthogonal line of the curve was found at each sampling point. The intersections of the orthogonal line and the boundary of the binary mask were the two border points of the mandible surface. The distance between each pair of border points was calculated to determine the bucco-lingual thickness of the mandibular shape (Fig. 4.4e).
- The sampling points obtained in previous step were used to find the corresponding border points in the binary mask of same slice in the MR image of the mandible.

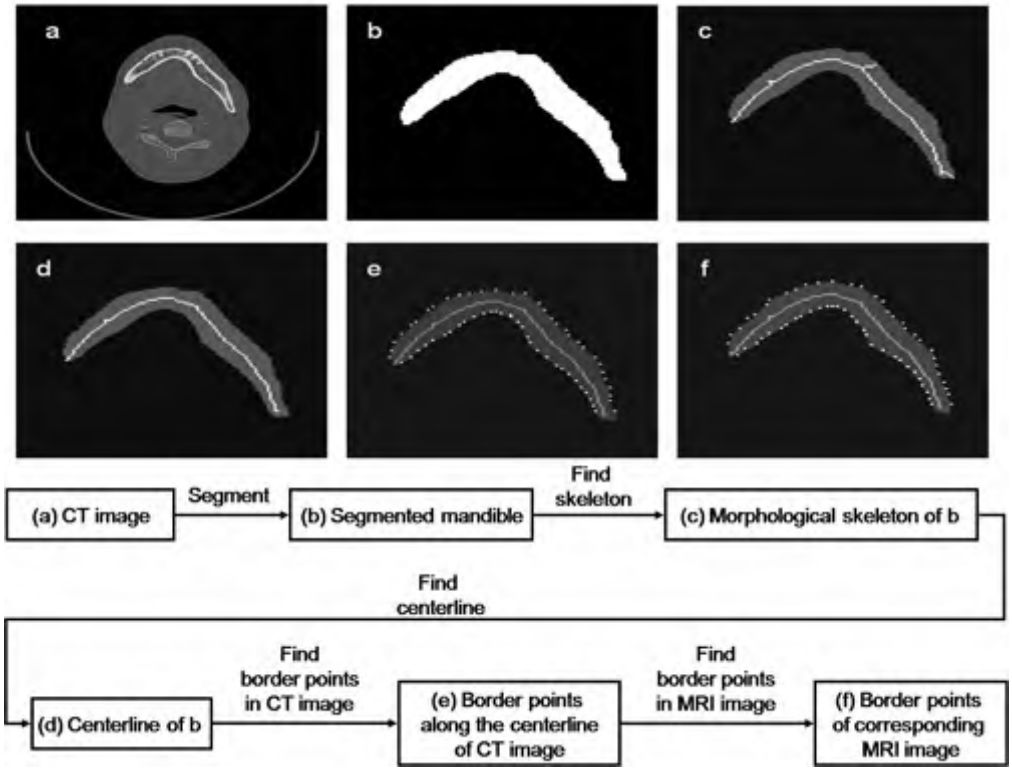

Figure 4.4: Procedures for determining the bucco-lingual thickness of the mandibular bone shape: (a) Original CT image; (b) Segmented binary image of the mandibular body; (c) Morphological skeleton of the mandible in (b); (d) Representative curve of the mandibular body; (e) Group pairs of border points along the representative curve; (f) Corresponding border points in segmented binary image from MRI.

4.3 Experiments and Results

The intra-operator reliability of segmentation was very high, with Pearson correlation coefficient of 0.986 and 0.998 for MRI and CT, respectively. The inter-operator reliability of segmentation was also very high, with Pearson correlation coefficient of 0.982 and 0.992 for MRI and CT.

The volumetric calculations were carried out between the paired models. The volume differences between MRI models and CT models were -807.1mm^3

(-0.91%), -3997.9mm^3 (-5.07%), and -2451.1mm^3 (-3.06%) for the three data sets respectively (Table 4.2). The Dice indexes of the paired models of data set 1 and data set 2 were 0.927 and 0.923. The Dice index of the third data set was higher than 0.841.

Surface point distances between MRI and CT were measured and shown in the second part of Table 4.2, the mean surface distances of the three data sets were all less than 1mm. The surface distance is presented at the colormap (in mm) in Fig. 4.5. In Fig. 4.5, most surface points of the MRI mandible were less than 1mm away from those of the CT mandible. But the surface points of the coronoid process and the temporomandibular joint (TMJ) of the mandible in MRI models were not close to those in CT models.

The bone thickness of the mandibular body was measured for the paired models. The thickness difference of the three data sets were 0.458 ± 0.324mm, -0.664 ± 0.116mm and -0.762 ± 0.440mm respectively.

4.4 Discussion

This study was carried out to assess the quality of a reconstructed mandible obtained from MRI data compared with CBCT and MSCT data, which are regarded as the reference standard due to the higher resolution and better imaging of hard tissues. Since there is no way to obtain an absolute standard reference to assess the in vivo hard tissue imaging quality with MRI scanners, the images obtained from the MSCT and CBCT scanners were chosen as the clinically established ground-truth in this study.

Since the mandibular shape is complex, the similarity between the mandibu-

Table 4.2: Measurement difference between the MRI model and the CT model.

Volumetric Measurements				
No.	MRI Volume (mm^3)	CT Volume (mm^3)	Dice	
1	88139.7	88946.8	0.927	
2	74804.1	78802.0	0.923	
3	65427.6	67878.7	0.841	
Surface Difference Calibration				
No.	NSP[1]	Surf Dis[2] (mm) Mean$\pm$ SD[3]	$pvalue$	
1	37476	0.642$\pm$ 0.378	$<$0.001	
2	55898	0.626 $\pm$0.361	$<$0.001	
3	74581	0.861 $\pm$0.777	$<$0.001	
Bucco-lingual Thickness				
No.	NVS[4]	MRI BT[5] (mm)	CT BT (mm)	p value
1	663	13.384$\pm$3.530	12.926$\pm$3.205	0.002
2	1572	13.581$\pm$3.445	14.245$\pm$3.562	$<$0.001
3	984	17.360$\pm$4.406	18.121$\pm$3.966	$<$0.001

[1] NSP : number of surface points .
[2] Surf Dis: surface distance .
[3] SD: standard deviation
[4] NVS: number of valid sites
[5] BT: bucco-lingual thickness

Figure 4.5: Visualization of the surface distance (in mm) after a rigid registration. The result of data set 2 is shown here. The range of the distance is shown in the color bar of the maps. This color map ranged from blue (minimum distance) to red (maximum distance). (a), (b) are left view and right view. (c), (d) are top view and bottom view.

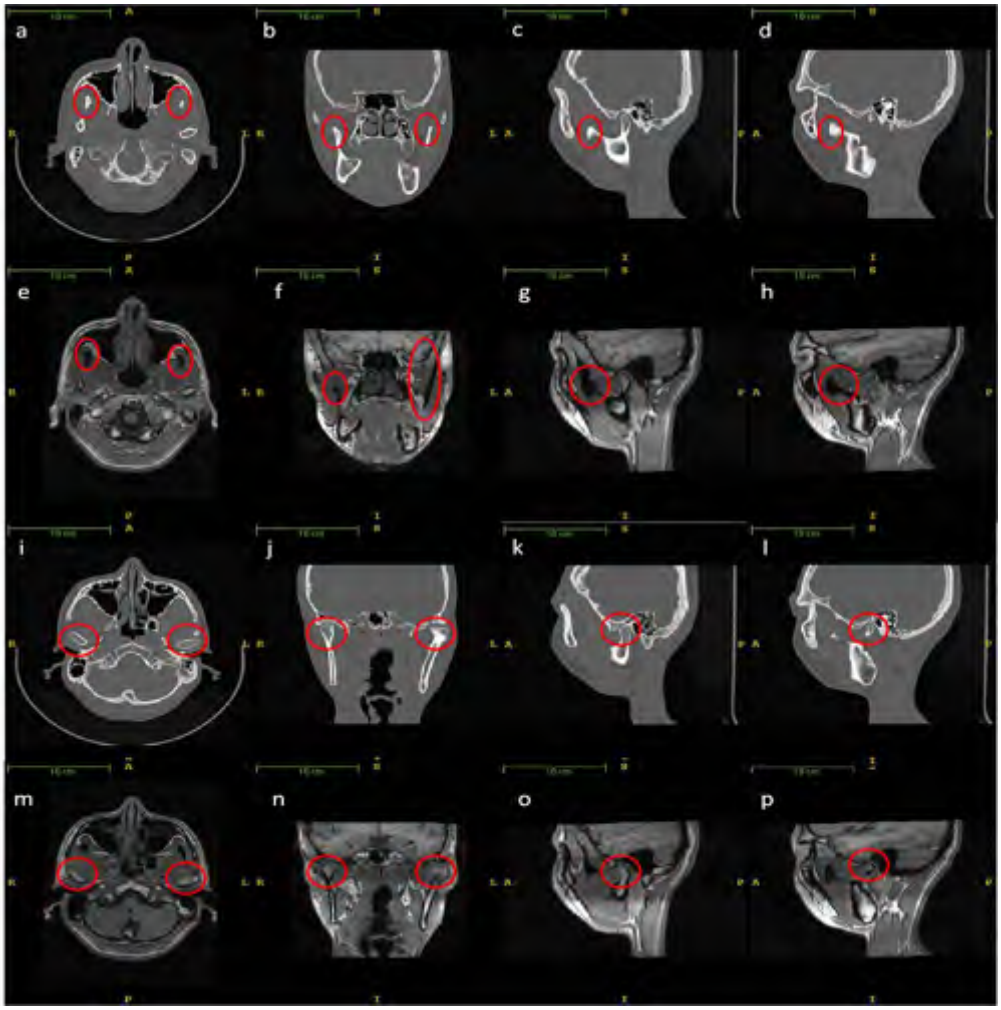

Figure 4.6: Image quality differences between MSCT and MRI data. The red circles are the regions of interest. (a)-(d) shows coronoid process in MSCT in transverse view, coronal view, sagittal view from left side, sagittal view from right side respectively; (e)-(h) shows coronoid process in the corresponding paired MRI. (i)-(l) shows TMJ in MSCT in transverse view, coronal view, sagittal view from left side, sagittal view from right side); (m)-(p) shows TMJ in in the corresponding paired MRI.

lar models obtained from MRI and CT was measured using different metrics. The volumetric measurements were carried out to assess the volumetric similarity between the mandibular models obtained from MRI and CT implicitly. Objects with different shapes may have very similar volumes. Accordingly, the volumetric measurement would not be convincing enough to reveal the similarity between the two models. Thus, the Dice indexes of the paired models were used to reveal the similarity of the co-registered models more explicitly. Then the surface distances between the co-registered models were calculated and visualized to reveal the surface similarity of the co-registered models. Finally, the accuracy of the mandibular body was assessed through the bucco-lingual thickness measurements.

Studies comparing the accuracy of hard-tissue shadows generated from MRI presented a contrasting approach to the problem. Clinically-driven studies, utilising human cadavers or phantom heads, relied on comparative linear measurements of the generated images and the physical object to assess the accuracy of MR imaging. However, linear measurements are prone to landmark-based inter-operator and intra-operator errors (Ludlow *et al.*, 2007). In contrast, studies that assume the fidelity of MR imaging examined the accuracy of algorithms used for image segmentation and registration. Hence, the value proposition in our in-vivo study is that the reliability of MRI-generated hard-tissue shadows of the mandible is examined against CT imaging using automated algorithms that have been proven to be accurate.

The volume differences between MRI models and CT models were -807.1mm^3 (-0.91%), -3997.9mm^3 (-5.07%), and -2451.1mm^3 (-3.06%) for the three data sets respectively (Table 4.2). This result showed the calculated volume differ-

ences between the paired models are small. The Dice indexes of the paired models of data set 1 and data set 2 were 0.927 and 0.923. The Dice index of the third data set was higher than 0.841. The high Dice index values showed the paired models were aligned accurately. The average surface distance between the mandible generated from MRI scanners and that generated from CT scanners were less than 1 mm. Since the experiments were carried out on the whole mandible which is a large and complex object, the accuracy of match between the image data is likely to vary across the entire body of the mandible. According to Figure 4.5, all the sites in MRI mandible were very close to those of MSCT or CBCT mandible except the two areas: coronoid process and TMJ of the mandible.

The Dice indexes of the paired models of data set 1 and data set 2 were higher than that of the third data set. This difference may be due to image resolution difference between MRI and CT data of data set 3 is slightly larger than the other two sets (Table 4.1). Another possible reason may be due to the shape differences between the three volunteers' mandibles. If the volume ratio between the area with larger errors, say the coronoid process and TMJ, and the area with smaller errors, say the mandible body, is larger, the Dice index may be lower.

With respect to the the anatomic part of the mandible located at the coronoid process, the larger difference between the MRI generated bone shadow and that of the CT bone shape is due to the thinness of the coronoid process, which is near the limit of the spatial resolution of MRI scanners used in this study. The other reason for the poor imaging quality for this part is its similar intensity level compared with nearby soft tissues, which is due to the partial volume effect

(Figure 4.6, (a)-(h)). The third reason is the patient movement effect. The above three reasons make it difficult to capture the coronoid process of the mandible by MRI scanners. From this study, the MRI quality for the coronoid process of the mandible is currently not reliable.

Regarding the TMJ, in Figure 4.6, (i)-(p), the overall shape of the TMJ was well captured in MRI, but the area near the condyle was more than 1 mm away from the CT model. The boundary of the condyle was partially missing in MRI. That is because this area is always a mixture of bone tissue, soft tissue and air, and the partial volume effect makes it difficult to define the boundary of TMJ. Another reason is the patient movement effects during the long imaging process, which typically lasts more than five minutes. The segmentation difficulty of the TMJ is also influenced by the spatial resolution of MR imaging used in this study.

Segmentation accuracy of the study is very high (the value of the Pearson correlation coefficients are greater than 0.98 for both the interclass correlation and the intraclass correlation), which means the segmentation results are reliable. The influences of registration algorithm, image resolution and field of view (FOV), which are potential factors of biases, are not investigated in this study.

It is difficult to obtain clinically indicated paired CT and MRI data from the same patient as clinicians usually prescribe only one imaging modality for diagnostic evaluation of oral and facial conditions. This study was based on three pairs of datasets, which were taken with different MSCT, CBCT and MRI scanners with different imaging parameters (resolution, field of view). In recognition of the different image datasets, this study did not aim to give an accuracy com-

parison between different scanners; instead it served to show the applicability and utility of magnetic resonance imaging for bone tissues. On the basis that the overall surface distance between MRI and CT models were acceptable, MRI may be applicable for a common clinical application in orthodontics as in the assessment of mandibular position changes in younger patients on growth modification of the facial jaw bones, since anatomic information within the jaw bones is not required for diagnostic and simulatory treatment effects. As MRI poses no risk of ionizing radiation exposure to children and younger patients, its use as the default imaging modality for these patients requiring pre- and post growth modification treatment imaging investigations becomes a value proposition. The value proposition of MR imaging comes into a sharp focus where the muscles of mastication such as the masseters, the medial pterygoids, the lateral pterygoids, and the temporalis muscles can be easily segmented (Ng *et al.*, 2006b) to generate the anatomic models of these muscles together with the mandibular shape for these young patients from a diagnostic and treatment evaluation perspective without subjecting these patients to any form of ionizing radiation.

With more paired image data sets from one pair of MRI and CT scanners under same imaging parameters, it is logical to assume that the models of the mandibular jaw bone generated from MRI data can be more appropriately compared to those from CT data. In conclusion, this study showed that 3D mandible model generated from MRI data was similar with those from CT data in terms of volumetric calculations, surface points distance and bone dimension. Certain anatomic regions of the mandible such as the coronoid process and the temporomandibular joint of the mandible in MRI data was less reliable compared with identical regions defined in the CT data.

Chapter 5

Segmentation of anterior teeth in CBCT

In this chapter, we present a level-set based approach for the segmentation of anterior teeth in CBCT images. The proposed approach can solve another sub-problem of bone segmentation in the oral and maxillofacial region as we described in Chapter 1. The details of the algorithm are presented in the following sections.

5.1 Introduction

5.1.1 Motivation

The roots of teeth in the mouth are invisible to the naked eye since roots are buried within the jaw bones. Traditional dental x-rays provide a 2D uni-planar view of these roots. Unfortunately, these 2D views do not give the accurate spatial orientation of these roots in relation to neighbouring structures. When teeth

need to be moved in individuals who require orthodontic treatment to correct malaligned teeth, the accurate representation of the roots of teeth is critically important to ensure that teeth can be moved through bone and parked into predetermined positions within the jaw bone before treatment commences. Hence, accurate image segmentation of the 3D images of the jaw bones and tooth roots plays an important role in aiding clinical decision making through simulation of tooth movement. The use of multi-slice computed tomography (MSCT) to obtain 3D images of the jaws and teeth exposes patients to high amounts of ionizing radiation that pose a heightened risk of developing cancers (Brenner *et al.*, 2001; Longstreth *et al.*, 2004; Memon *et al.*, 2010). In recent years, dental CBCT has gained popularity in dentistry for 3D imaging of facial bones due to its high resolution for bone tissues and relatively lower radiation exposure (Schulze *et al.*, 2004). However, tooth segmentation in CBCT is more challenging than that in CT because the image is noisier (Fig. 5.1), and the image contrast between the tooth root and the alveolar bone in CBCT is lower. The tooth boundary is too ambiguous to be exactly defined especially at the root. In clinical studies, tooth segmentation is usually performed manually by trained dentists, which is a very time consuming and tedious process. The availability of automatic or semiautomatic tooth segmentation methods will greatly assist the clinician in this task. The aim of this study was to develop a more accurate and robust framework to semi-automatically define contours of the roots for the six front teeth (also known as anterior teeth) in CBCT images and evaluate its accuracy against other methods and manual segmentation.

Figure 5.1: Image quality comparison between traditional MSCT and CBCT.

5.1.2 Related work

Several image segmentation algorithms have been proposed to segment objects from CT images. An adaptive thresholding method has been proposed by Heo & Chae (2004) to segment the tooth. However, due to the nonhomogeneous intensity distribution inside each tooth, as well as the surrounding alveolar bones, thresholding usually leads to under segmentation or over segmentation problems.

Conventional active contour methods for medical image segmentation are either edge-based or region-based. Both methods have serious limitations. Edge-based segmentation approaches, like the active contour (Xu & Prince, 1998), use local edge information to evolve the contour to the edges. These methods fail at boundaries where the edges between the ROI and the background are not clear. Region based segmentation (Chan & Vese, 2001), which uses different intensity distributions of ROI and background to separate each other, fails in areas where

the region inside the ROI has similar intensity levels to those of the background. Therefore, neither edge-based nor region-based methods are suitable for tooth segmentation in CBCT.

Hybrid segmentation methods (Chen & Metaxas, 2005) can overcome the limitations of the above methods by combining the intensity distribution and the edge information into one energy functional for optimization. However, without the aid of shape priors, such a method still fails to avoid the "shrinking" and "leaking" problems in areas where the ROI and the background have similar intensity distributions. 2D or 3D shape priors (Tsai *et al.*, 2003) have been developed for segmentation, but these methods are not suitable for shapes with large variations such as human teeth. Building such shape priors requires large training sets and tedious training processes.

A recent tooth segmentation method using level set with shape and intensity prior has been proposed by Gao & Chae (2010). They propose to segment the crown and the root separately with two level-set based algorithms. This method generates a shape prior with intensity and boundary features and combines the three terms into one energy functional to be minimized. Although their method can segment the tooth crown in CBCT, it fails to segment the tooth root due to the following reasons. First, its calculation of intensity distribution is not accurate because the area inside the tooth contour actually consists of two different regions (the tooth dentine and the tooth pulp) and the area outside the tooth contour also consists of two different regions (the jaw bone and other soft tissues). Second, its shape prior is not robust. Third, it does not have any energy term to prevent leakage or shrinking problems during the segmentation process.

5.1.3 Our approach

To address the problems in the segmentation of tooth roots in CBCT images, we propose to segment the tooth root in two steps: (1) segment the tooth pulp first instead of segmenting the tooth root directly and (2) segment the tooth dentine using the segmented tooth pulp to obtain a more accurate intensity density function of the tooth dentine and build a leakage-preventing energy term. The proposed method is novel in three aspects: we propose a more accurate intensity model, a new shape prior, and a new tooth dentine wall thickness constraint for preventing shrinking and leakage.

5.1.4 Chapter organization

Following the introduction, Section 5.2 describes the acquisition of CBCT tooth images and the proposed algorithm. Section 5.3 presents the experiments and results, followed by the discussion in Section 5.4 and the conclusion in Section 5.5.

5.2 Materials and Methods

5.2.1 Materials

CBCT image data sets are obtained using a Kavo 3D eXam 2nd Generation CBCT scanner with a 0.2mm$\times$0.2mm$\times$0.2mm spatial resolution (400$\times$400 matrix per slice of image, with the number of slices ranging from 213 to 256). Ten CBCT image data sets are used in our study. Forty-five teeth from the ten pa-

tients are used for the final test, with thirty are incisors and fifteen canines[1].

5.2.2 Methods

5.2.2.1 Crown segmentation

Segmentation of tooth crown is much less challenging than segmentation of tooth root, and crown segmentation has been well solved by Gao & Chae (2010). In this study, we use their algorithm to segment the crown from the adjacent teeth in CBCT images. We will not present the implementation of the coupled level set for crown segmentation, as the reader may easily refer to the article.

5.2.2.2 Root segmentation

Given a CBCT tooth image, our aim is to develop a semiautomated method that can define a contour separating the image into two groups: the tooth root and the background. The method consists of two phases: image preprocessing and contour initialization, and tooth dentine contour evolution. The evolution of the tooth dentine contour is designed with five objectives:

- Penalizing energy: the contour is penalized with a signed distance function (SDF).
- Region energy (intensity distribution energy): we assume that the intensity distributions inside and outside the tooth follow different models. We propose a more accurate way to estimate the intensity distribution of the dentine.

[1]Some images cover only half the maxilla or mandible of the patient and thus not all the teeth of the patients are used in the study.

- Edge energy: An external energy is defined to move the curve towards prominent edges of the object.
- Shape prior energy: we do not directly use the SDF of the final contour in the previous slice, which is used in Gao & Chae (2010) to serve as our shape prior. Instead, we assign larger weights to pixels with positive curvature and smaller weights to those with negative curvature.
- Dentine wall thickness energy: we use the interaction between the tooth pulp contour and the tooth dentine contour to prevent shrinking and leakage.

5.2.2.3 Image preprocessing

The original CBCT images are first normalized to the intensity range from 0 to 255, followed by a filtering with a rotationally symmetric Gaussian filter of size 15×15 with standard deviation 1.5 to suppress noise (Fig. 5.2).

5.2.2.4 Level set definition and initialization

In the proposed level set method, the tooth (tooth pulp and tooth dentine) contour C is represented by the zero value of a level set function

$$C(t) = \{(x, y) \in \Omega | \phi(t, x, y) = 0\} \tag{5.1}$$

where Ω is the set of pixels in the image, and ϕ is the SDF from the tooth contour. In this paper, all the SDFs are defined as negative inside the contour

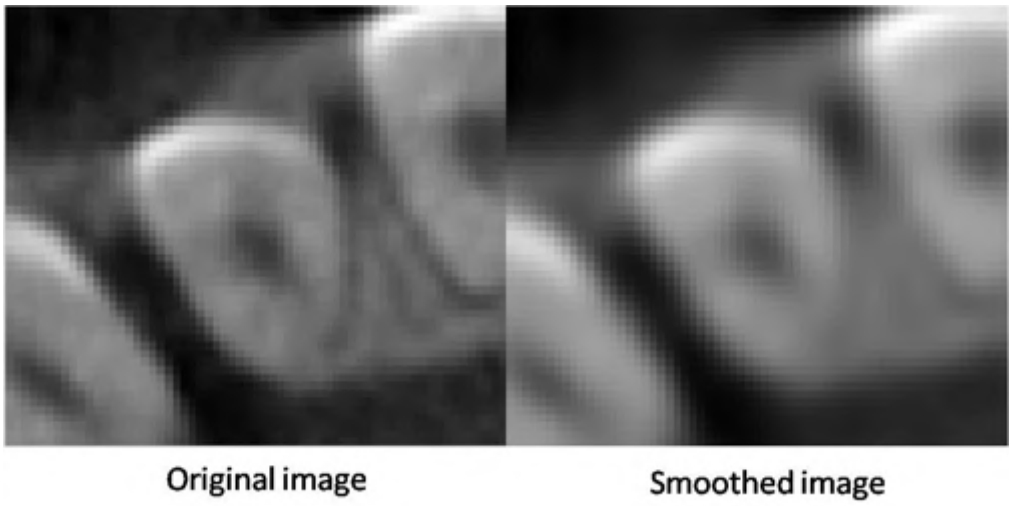

Figure 5.2: Original image and smoothed image.

and positive outside the contour. The region of the tooth is defined as

$$\Omega = \{(x, y) \in \Omega : \phi(x, y) \leq 0\} \tag{5.2}$$

The tooth dentine contour initialization process is the same as that defined in Gao (2010). Observing from the tooth anatomy (Fig. 5.3), we find that the crown touches neighboring teeth, while the root touches the surrounding alveolar bone. For convenience, three typical slices are to be determined: S_1, S_2 and S_3. S_1 is the slice where the area of tooth crown is maximal in the axial plane. S_3 is the slice where the jaw bone starts to appear. S_2 lies midway between S_1 and S_3, and is selected as the initial slice of the tooth root segmentation.

The initial slice can be easily segmented with the traditional level set framework described in Li *et al.* (2005), because the tooth does not touch the adjacent tooth or the jaw bone. As described in Gao & Chae (2010), we only need to segment one single slice of the image set. For any slice other than this initial slice,

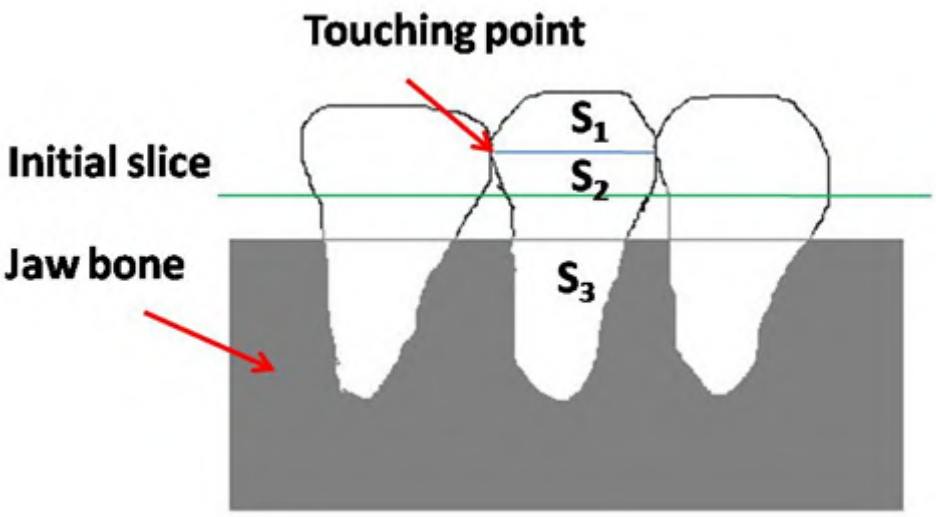

Figure 5.3: Illustration on how to select the initial slice.

the shape prior and intensity distribution energy functionals can be derived from the final evolution contour of the previous slice, because the ROI boundaries in the consecutive two slices are very similar to each other. The procedure of the tooth segmentation in adjacent images is illustrated in Fig. 5.4.

5.2.2.5 Energy functionals

We can combine the five objectives into one functional $J(C)$ with five energy terms as follows:

$$\begin{aligned} J_R(C) = \lambda_1 J_1(C) + \lambda_2 J_2(C) + \lambda_3 J_3(C) \\ +\lambda_4 J_4(C) + \lambda_5 J_5(C) \end{aligned} \tag{5.3}$$

where $J_R(C)$ is the total energy term to segment the tooth root, $J_1(C)$ the penalizing energy term, $J_2(C)$ region energy term, $J_3(C)$ the edge energy term,

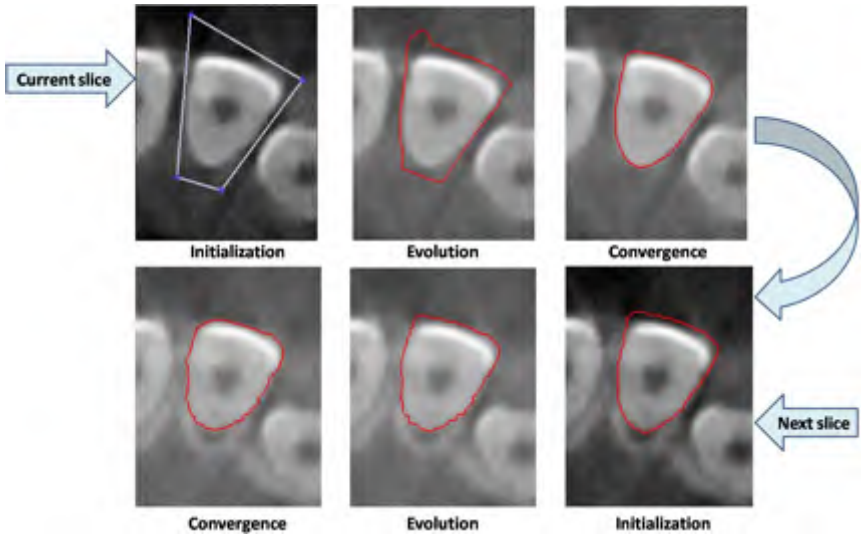

Figure 5.4: Illustration on how the active contour works to segment two consecutive slices.

$J_4(C)$ the shape prior energy term, $J_5(C)$ the dentine wall thickness energy term, and λ_i the weight for the ith energy term. Compared with Eq. (2) in Gao & Chae (2010), our energy functional has a new term $J_5(C)$,a more accurate way to calculate the intensity distribution in $J_2(C)$ and a more accurate representation of shape prior in $J_4(C)$. According to Eq. (5.1), the energy function can be rewritten as

$$\begin{aligned} J(\phi) = \lambda_1 J_1(\phi) + \lambda_2 J_2(\phi) + \lambda_3 J_3(\phi) \\ + \lambda_4 J_4(\phi) + \lambda_5 J_5(\phi) \end{aligned} \tag{5.4}$$

We describe the details of each term now.

(1) Penalizing energy: The definition of the penalizing term is the same as

Eq. (2) in Li *et al.* (2005), which is

$$J_1(\phi) = \int_\Omega \frac{1}{2}(|\nabla\phi| - 1)^2 dxdy \tag{5.5}$$

where ∇ is the gradient operator. This term penalizes the deviation of ϕ from a SDF during evolution.

(2) Region energy: The final goal is to separate the region Ω of the image into two regions, the object region Ω_1 and the background region Ω_2 by one contour C. The region-based model usually separates these two regions using intensity distribution differences. The framework for the region-based term is similar to that described in Pluempitiwiriyawej *et al.* (2005). Assume a pixel with intensity value $u_1 = \{u_{xy} : (x, y) \in \Omega\}$ belongs to the object, which has an intensity distribution with a statistical model $\boldsymbol{M}_1$, and a pixel with intensity value $u_2 = \{u_{xy} : (x, y) \in \Omega\}$ belonging to the object, which has an intensity distribution with a statistical model $\boldsymbol{M}_2$. The contour can approach an optimal curve by maximizing the likelihood function

$$J_0(C) = p(u|C, \boldsymbol{M}_1, \boldsymbol{M}_2) \tag{5.6}$$

where $p(u|C, \boldsymbol{M}_1, \boldsymbol{M}_2)$ is the joint probability density function (PDF) for intensities u given the contour C and the two models. Suppose the two models are statistically independent, Eq. (5.6) can be rewritten as

$$J_0(C) = p_1(u_1|C)p_2(u_2|C) \tag{5.7}$$

where p_1 and p_2 are the PDFs related with $\boldsymbol{M}_1$ and $\boldsymbol{M}_2$. Taking the negative log,

Eq. (5.6) becomes

$$J_0(C) = -\ln(p_1(u_1|C)) - \ln(p_2(u_2|C)) \tag{5.8}$$

Assuming the intensity distributions within each region are statistically independent and the contour C is the zero level of the SDF ϕ, then Eq. (5.8) becomes

$$\begin{aligned} J_2(\phi) &= \int_{\Omega_1} -\ln(p_1(u(x,y)|\Omega_1)dxdy + \int_{\Omega_2} -\ln(p_2(u(x,y)|\Omega_2)dxdy \\ &= \int_{\phi\leq 0} -\ln(p_1(u(x,y)|\Omega_1)dxdy + \int_{\phi>0} -\ln(p_2(u(x,y)|\Omega_2)dxdy \\ &= \int_{\Omega} -\ln(p_1(u(x,y)|\Omega_1)H(-\phi)dxdy \\ &+ \int_{\Omega} -\ln(p_2(u(x,y)|\Omega_2)\left(1 - H(-\phi)\right)dxdy \end{aligned} \tag{5.9}$$

The only difficulty left is to obtain an accurate PDF for intensities within each region. Generally, the image can be separated into two regions: the tooth root and the background. In Gao & Chae (2010), they only use a single histogram for each region to calculate the tooth root and the background. In actual fact, the region within the tooth root (Ω_1) can be separated into two subgroups: the dark region tooth pulp Ω_p and the bright region tooth dentine Ω_d. The background Ω_2 also contains two different clusters: the dark region (Ω_s) which are the soft tissues and the bright region (Ω_a) which is the jaw bone (alveolar bone). We illustrate the differences between the proposed model and that used in Gao & Chae (2010) in Fig. 5.5.

To obtain an intensity model that can represent the tooth pulp and the tooth

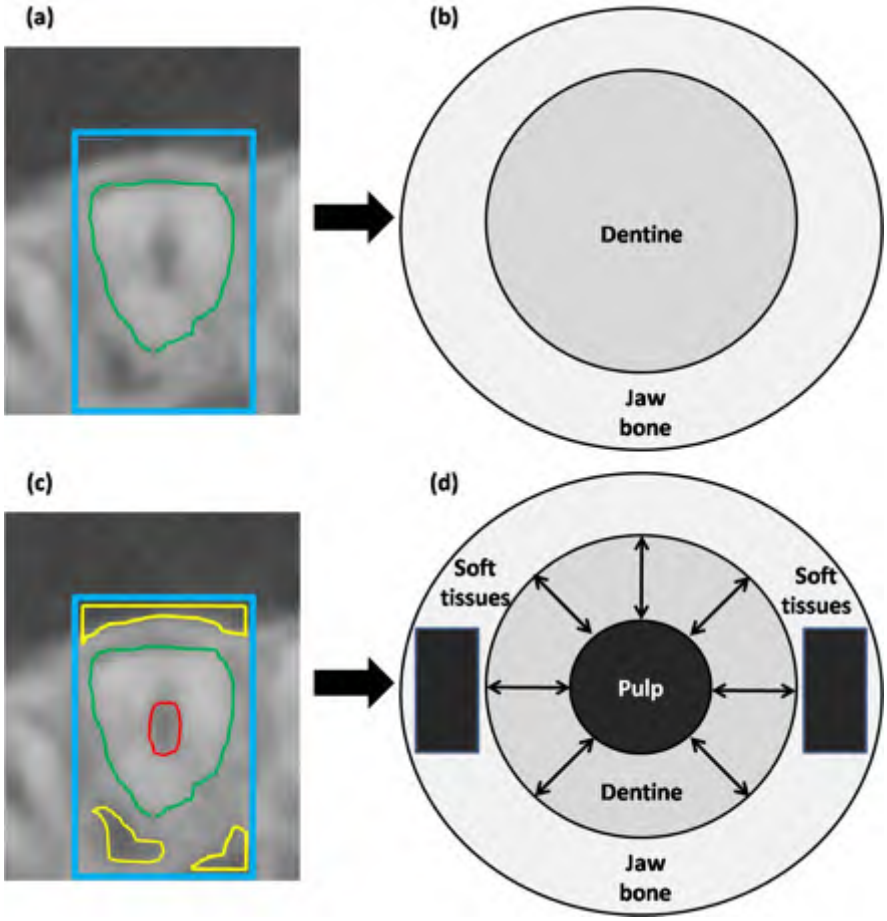

Figure 5.5: Illustration of the differences between the proposed model and that used in Gao & Chae (2010): (a) and (b) are Gao & Chae (2010)'s model, while (c) and (d) are our model. (a) The region within the box defined with blue line is divided into two different regions: the tooth root and the background; (b) The simplified model of the tooth root and the background; (c) The region within the box defined with blue line is divided into four different regions: (1) the tooth pulp which lies in the red contour, (2)the tooth dentine which lies between the red and green contour, (3) the other soft tissues which lie in the yellow contours, and (4) the jaw bone which lie in the region within the blue contour excluding the above three regions; (d) The simplified model of the tooth root and the background: the black arrows show the thickness of the tooth dentine wall.

dentine, we divide Ω_1 into two subregions:

$$\begin{aligned} \Omega_p &= \{(x,y)|u(x,y) < t_1\} \\ \Omega_d &= \{(x,y)|u(x,y) \geq t_1\} \end{aligned} \tag{5.10}$$

where t_1 is a threshold partitions the tooth regions into two clusters. Its value can be obtained using K-means clustering (Hartigan & Wong, 1979) by choosing the maximum and minimum intensity values within the tooth region as the initial cluster centroid positions.

Then, the PDF of tooth region p_1 can be rewritten as:

$$p_1(u(x,y)|\Omega_1) = \begin{cases} p(u(x,y)|\Omega_p) \text{ if } u(x,y) < t_1 \\ p(u(x,y)|\Omega_d) \text{ if } u(x,y) \geq t_1 \end{cases} \tag{5.11}$$

If the active contour works effectively, it will always evolve outside the tooth dentine Ω_d. Thus we can exclude the PDF of the tooth pulp Ω_p and use only Ω_d to represent the tooth. Eq. (5.11) can be rewritten as

$$p_1(u(x,y)|\Omega_1) = p(u(x,y)|\Omega_d) \tag{5.12}$$

where $p(u(x,y)|\Omega_d)$ can be estimated using the histogram of the tooth dentine (the region between the green contour and the red contour shown in Fig. 5.5). The main difference between our method and that of Gao & Chae (2010) is that we estimate and exclude the tooth pulp region and use the tooth dentine to represent the tooth. As shown in Fig. 5.6, the new PDFs of the tooth and the background have much less overlap compared with the PDFs estimated in Gao & Chae (2010).

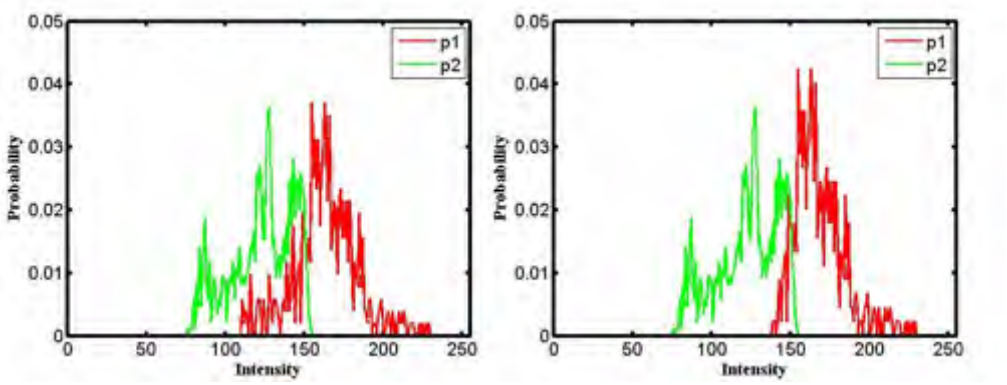

Figure 5.6: Intensity probability distribution estimated from histograms of the tooth and background intensities of Gao's method and the proposed method: The left image shows the probability distribution in Gao & Chae (2010); The right image shows the probability distribution of the proposed method. P_1 is the probability distribution of the tooth, P_2 is the probability distribution of the background

Similarly, the background Ω_2 also contains two different clusters: the dark region (Ω_s) contains soft tissue and air while the bright region (Ω_a) contains alveolar bone. We divide Ω_2 into two subregions:

$$\begin{aligned} \Omega_s &= \{(x,y)|u(x,y) < t_2\} \\ \Omega_a &= \{(x,y)|u(x,y) \geq t_2\} \end{aligned} \tag{5.13}$$

where t_2 is a threshold partitions the background regions into two clusters. Its value can be obtained using K-means clustering (Hartigan & Wong, 1979) by choosing the maximum and minimum intensity values within the background region as the initial cluster centroid positions. Since the region outside the tooth is large, the histogram of the background is only computed in a 5-pixel wide band outside the tooth contour. The width of the band is actually flexible as long as it does not touch the tooth dentine of neighboring teeth. The PDF of the

tooth region p_1 can be rewritten as

$$p_2(u(x,y)|\Omega_2) = \begin{cases} p(u(x,y)|\Omega_s) \text{ if } u(x,y) < t_2 \\ p(u(x,y)|\Omega_a) \text{ if } u(x,y) \geq t_2 \end{cases} \tag{5.14}$$

where $p(u(x,y)|\Omega_s)$ and $p(u(x,y)|\Omega_a)$ can be estimated using the histogram of the background.

(3) Edge energy: The edge-based term forces the contour C to approach the edges in the image. This is realized by minimizing the following functional:

$$J_3(\phi) = \int_C g ds \tag{5.15}$$

where ds represents the Euclidean arc length of C. Note that ϕ is the SDF of C, we have

$$J_3(\phi) = \int_\Omega g\delta(\phi)|\nabla\phi| dxdy \tag{5.16}$$

where g is a positive and decreasing function serving as an edge detector, δ is the smoothed Dirac function (introduced in Section 2.3.2.6), and ∇ is the gradient operator. We use Eq. (9) in Gao & Chae (2010) as our edge indicator function

$$g = \begin{cases} 1, & \text{if } -\nabla\phi \cdot \nabla u_G \leq 0 \\ \dfrac{1}{1+|\nabla u_G|^2}, & \text{if } -\nabla\phi \cdot \nabla u_G > 0 \end{cases} \tag{5.17}$$

where $u_G = G_\sigma * u_0$, the convolution of the image u_0 with the Gaussian kernel of standard deviation σ (fixed at 1.5), is the smoothed image. Note that g is calculated only once for each image slice in the segmentation process.

(4) Shape prior energy: The shape prior term is added into the functional by

forcing the evolving contour C to approach the final segmentation contour C_0 of the previous slice:

$$J_4(C) = \int_C \phi_0^2(x,y)ds \tag{5.18}$$

where ϕ_0 is the SDF of the segmented tooth region of previous slice. Note that ϕ is the SDF of C, we have

$$J_4(\phi) = \int_\Omega \phi_0^2(x,y)\delta(\phi)|\nabla\phi|ds \tag{5.19}$$

Gao & Chae (2010) gives equal weights to all the pixels on the shape prior. However, we notice that pixels with negative curvature C_{0-} are less likely to be a portion of the tooth contour compared to those with positive curvatures C_{0+}, where

$$\begin{aligned} C_{0+} &= \{(x,y) : (x,y) \in C_0 \text{ and } \kappa > 0\} \\ C_{0-} &= \{(x,y) : (x,y) \in C_0 \text{ and } \kappa \leq 0\} \end{aligned} \tag{5.20}$$

In the above equation, $\kappa = \nabla\left(\frac{\nabla\phi_0(x,y)}{|\phi_0(x,y)|}\right)$ is the curvature of the contour, and $\phi_0(x,y)$ is the SDF of the contour C_0. Since we have more confidence in a contour with positive curvature, we can assign larger weights to pixels with positive curvature and smaller weights to those with negative curvature. So we modify $\phi_0(x,y)$ to give $\hat{\phi}_0(x,y)$:

$$\hat{\phi}_0(x,y) = \begin{cases} \phi_0(x,y) \text{ if } \kappa > 0 \\ \omega\phi_0(x,y) \text{ if } \kappa \leq 0 \end{cases} \tag{5.21}$$

where $0 < \omega < 1$. We have the fourth term in the energy functional:

$$J_4(\phi) = \int_\Omega \hat{\phi}_0^2 \delta(\phi) |\nabla \phi| dxdy \tag{5.22}$$

(5) Dentine wall thickness energy: The tooth dentine wall is the area between the boundaries of the tooth pulp and the tooth (Fig. 5.5)). We observe that the active contour C is easy to shrink in regions where the dentine wall is thin. Because the contour of the tooth pulp C_p is easy to segment, the tooth pulp contour is used to refine the tooth contour by controlling the tooth dentine thickness where the dentine wall is thin.

Define $D((x, y), C_p)$ as the distance between a point (which is located on C) and the curve C_p, and $D(C, C_p)$ as the collection of all such distances of points on C. $D(C(x, y), C_p)$ can then be divided into two groups $D_{thick}(x, y)$ and $D_{thin}(x, y)$ using K-means clustering. D_{avg} denotes the average value of $D_{thin}(x, y)$. This enables us to define

$$\phi_t(x, y) = \phi_p(x, y) - D_{avg} \tag{5.23}$$

where $\phi_p(x, y)$ is the SDF of the contour of the tooth pulp C_p, $\phi_t(x, y)$ is the SDF of the shape which is a enlarged version of the tooth pulp. Based on the definition of $\phi_p(x, y)$, we have the fifth term in the energy functional:

$$J_5(\phi) = \int_\Omega \phi_t (H(\phi_t) - H(\phi)) dxdy \tag{5.24}$$

where H is the smoothed Heaviside function (introduced in Section 2.3.2.6). Fig. 5.7 illustrates the effectiveness of the new term to overcome the "over-

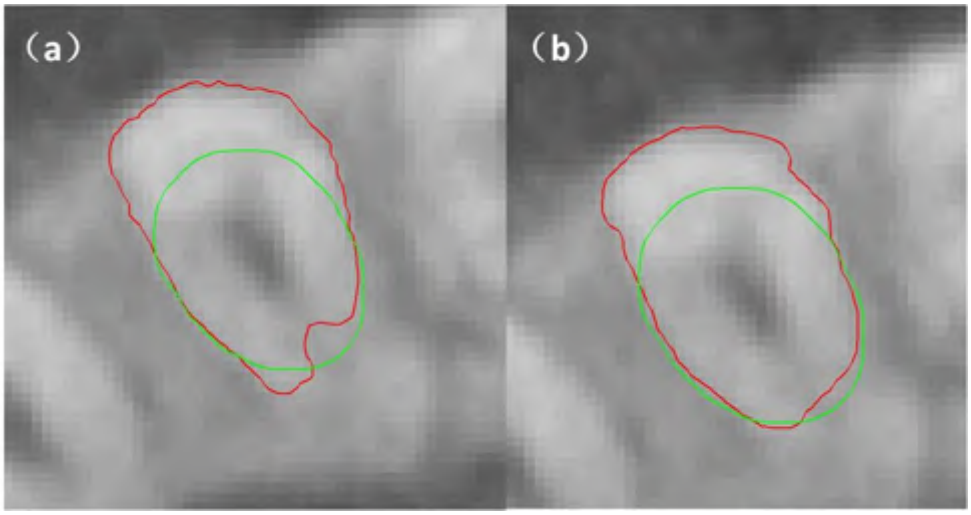

Figure 5.7: Comparison between (a) without tooth dentine thickness constraint and (b) with the constraint. The red line represents the current evolving tooth contour, and the green line represents the tooth dentine thickness constraint.

shrinking" problem.

(5) Overall energy functional: Replacing Eq. (5.5), Eq. (5.9), Eq. (5.16), Eq. (5.22), and Eq. (5.24) in Eq. (5.4), we have the proposed energy functional

$$\begin{aligned} J(\phi) = & \lambda_1 \int_\Omega \frac{1}{2}(|\nabla\phi| - 1)^2 dxdy \\ & + \lambda_2 \left(\int_\Omega -\ln(p_1) H(-\phi) dxdy + \int_\Omega -\ln(p_2)\left(1 - H(-\phi)\right) dxdy \right) \\ & + \lambda_3 \int_\Omega g\delta(\phi)|\nabla\phi| dxdy \\ & + \lambda_4 \int_\Omega \hat{\phi}_0^2 \delta(\phi)|\nabla\phi| dxdy \\ & + \lambda_5 \int_\Omega \phi_t (H(\phi_t) - H(\phi)) dxdy \end{aligned} \tag{5.25}$$

5.2.2.6 Energy functionals minimization

To minimize the energy functional $J(\phi)$, ϕ has to be updated as follows (derived in Appendix A):

$$\begin{aligned}\frac{\partial \phi}{\partial t} &= \lambda_1 \left[\Delta\phi - \mathtt{div}(\frac{\nabla\phi}{|\nabla\phi|}) \right] + \lambda_2 \delta(\phi) \ln\left(\frac{p_2}{p_1}\right) \\ &+\delta(\phi)\left(\mathtt{div}\left((\lambda_3 g + \lambda_4 \hat{\phi}_0^2) \frac{\nabla\phi}{|\nabla\phi|} \right) \right) + \lambda_5 \delta(\phi)\phi_t\end{aligned} \tag{5.26}$$

where p_1 and p_2 are given in Eq. (5.12) and Eq. (5.14), g is given in Eq. (5.17), $\hat{\phi}$ is given in Eq. (5.21), ϕ_t is given in Eq. (5.23), and λ_1, λ_2, λ_3, λ_4, λ_5 are weighting coefficients that have to be tuned. Because the shape prior is close to the real tooth contour, 25 rounds of iterations were enough for segmenting tooth contours.

Since the area of the initial contour of the tooth is the largest one in the entire tooth in the axial plane and the area of the tooth tends to decrease gradually from the initial slice to the root tip, the active contour should shrink rather than expand during the contour evolution process. Similar to Eq. (11) in Gao & Chae (2010), we use the following equation to replace λ_2:

$$\lambda_2 = \begin{cases} \lambda_s \text{ if } \log\left(\frac{p_2}{p_1}\right) > 0 \\ \lambda_e \text{ if } \log\left(\frac{p_2}{p_1}\right) \leq 0 \end{cases} \tag{5.27}$$

where λ_s and λ_e represent the shrinking coefficient and the expanding coefficient, respectively. These two parameters drive the contour as follows:

- if $p_2 \geq p_1$, which means the pixel is more likely to lie in the background, then it should shrink and move inward to the object;

- if $p_2 < p_1$, which means the pixel is more likely to lie in the object, then it should expand and move outward to the background.

Note that neither p_1 nor p_2 should be 0; when computing these two terms, a small value is added. To make the contour shrink more than expand, the value of λ_s should be set larger than λ_e.

5.2.2.7 Parameter analysis

An adult human usually has thirty-two teeth, with sixteen teeth in the maxilla, sixteen teeth in the mandible. The sixteen teeth in either jaw are symmetrically located in both half of the dental arch. Thus the shape of eight teeth in either side can represent all the other twenty-four teeth. The eight teeth can be further classified into: incisors, canines, premolars and molars. Both the incisors and the canines are classified as anterior teeth. These three teeth usually have only one root. The topological similarity of these anterior teeth in both jaws enable us to set the same parameters for all the anterior teeth. Empirically, we found that the six parameters can be set as: $\lambda_1 = 1$, $\lambda_s = 0.1$, $\lambda_e = 0.05$ $\lambda_3 = 0.8$, $\lambda_4 = 0.2$, $\lambda_5 = 0.1$. Note that all patient data are acquired with the same CBCT scanner using the same resolution but with different field of views. Thus there is no need to tune the weighting coefficients for different patients.

5.2.2.8 Validation

(1) Qualitative validation: We first qualitatively compared the segmentation performance of the proposed method against the manual segmentation and two other segmentation methods: the variational formulation method in Li *et al.*

(2005), and the level set method proposed in Gao & Chae (2010).

(2) Quantitative Validation: The manual segmentations of tooth root performed by a clinician serves as the ground truth. A second manual segmentation of tooth root performed by another clinician is applied to show the variability of the manual segmentation using Jaccard and Dice index values compared with the first time manual segmentation. The accuracy of different approaches are calculated by comparing the automatic segmentation results with the manual segmentation results. The Jaccard (Jaccard, 1912) and the Dice (Dice, 1945) similarities are used to assess the agreement between automatic and manual segmentation approaches. These two metrics are defined by:

$$Jaccard : J(V_1, V_2) = \frac{|V_1 \bigcap V_2|}{|V_1 \bigcup V_2|}, \tag{5.28}$$

$$Dice : D(V_1, V_2) = \frac{2|V_1 \bigcap V_2|}{|V_1| + |V_2|}. \tag{5.29}$$

where V_1 represents the voxel set of automatic segmentation results and V_2 represents the voxel set of the ground truth.

Besides the overlapping measures through the Jaccard and Dice indexes, the mean surface distance (MSD) is also calculated to assess the qualities of 3D models obtained by different algorithms.

5.3 Experiments and Results

Since the proposed method aims to improve the segmentation accuracy for the tooth root in CBCT, we only carried out comparison studies on the segmentation performances for this region of the tooth.

(1) Qualitative comparison: We first compared the segmentation performance of the proposed method with manual segmentation and two other segmentation methods: the variational formulation method in Li *et al.* (2005), and the level set method proposed in Gao & Chae (2010). Fig. 5.8 shows the results.

Compared with manual segmentation (Fig. 5.8(d)), even though the initial contours are the same, different methods yield different results. More specifically, the variational formulation method fails at places where information at the edge and intensity distribution are not able to drive the contour to the desired place. The level set method with shape and intensity prior fails by shrinking into the tooth pulp region. Compared with the previous two methods, our method is more accurate. The examples of final segmentation results in different slices of the proposed method are provided in Fig. 5.9 (axial view). The 3D tooth models reconstructed from segmented tooth root slices are shown in Fig. 5.10. Note that the crowns are segmented using the coupled level set method proposed by Gao & Chae (2010), and the roots are segmented using the proposed method.

(2) Quantitative validation: The algorithm was tested on a desktop computer with a Intel(R) Core (TM) 2 Duo CPU 2.65 GHz and 2.72 GB memory. The program was implemented in Matlab 7.11.0 (R2010b) installed in Microsoft Windows XP Professional. The average time consumed per tooth is 336 seconds. The quantitative performance comparison results between the proposed method, Gao's method and Li's method are shown in Table 5.1 and Fig. 5.11. The mean accuracy of the second time manual segmentation is 0.998 ± 0.002 (0.998 is the mean value and 0.002 is the standard deviation) for Jaccard index (JI), 0.999 ± 0.001 for Dice index (DI). The large JI and DI means variability of the manual segmentation is very small. The manual segmentation results are

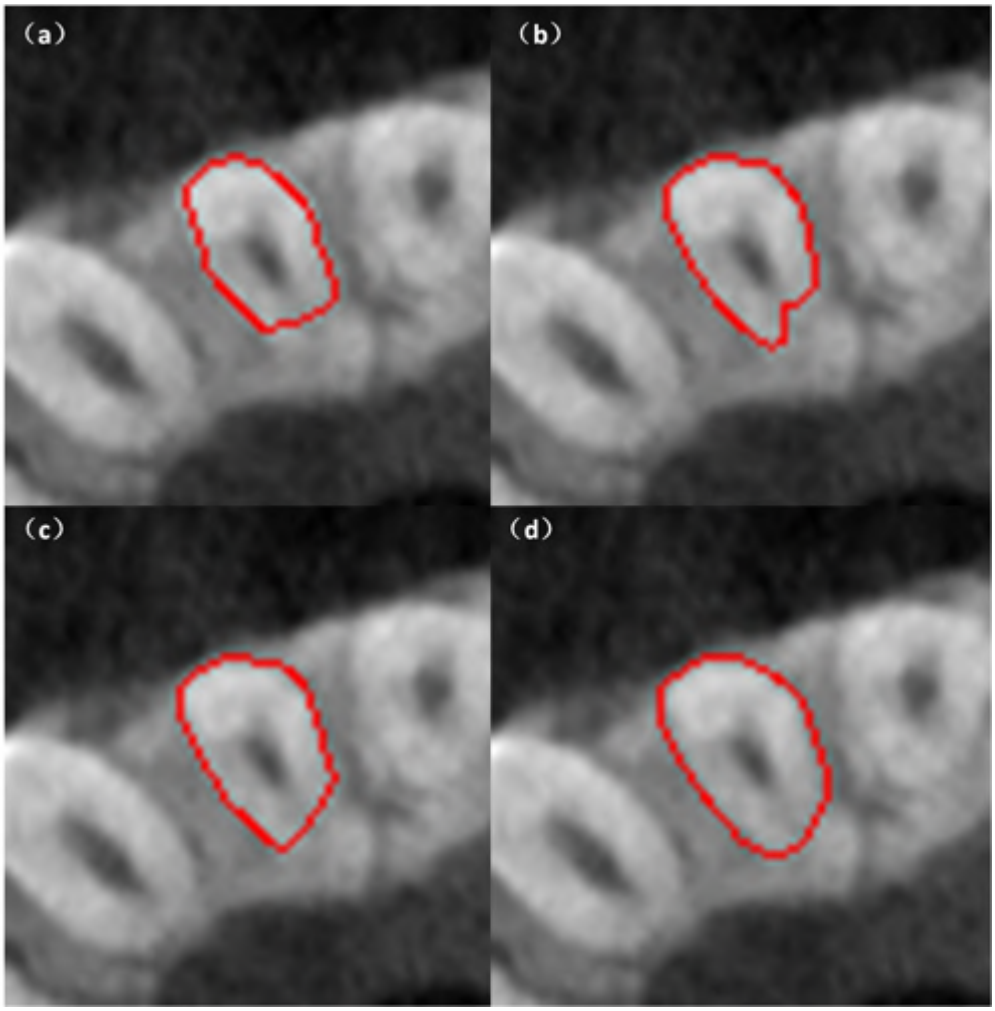

Figure 5.8: Comparison between the different segmentation methods: (a) variational formulation method, (b) level set method with shape and intensity prior, (c) our segmentation framework, (d) manual segmentation.

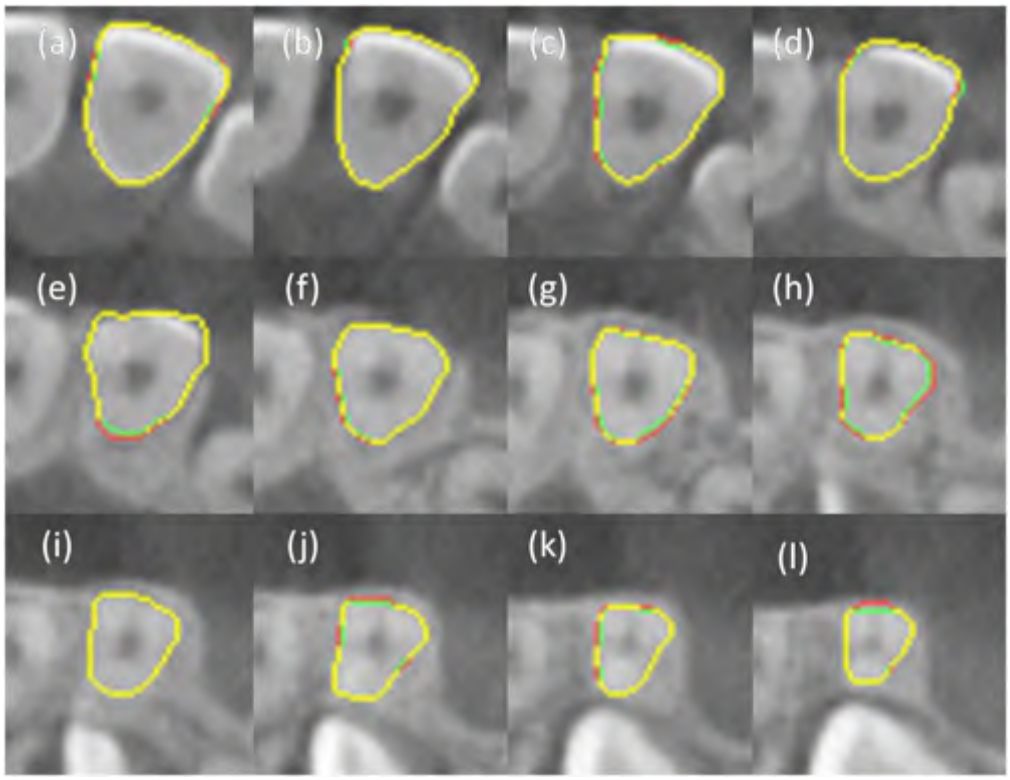

Figure 5.9: Tooth root segmentation result of the proposed method: Images (a)-(l) are the segmentation result selected from the initial slice to the root tip. The green lines are the ground truth; the red lines are automatic segmentation results; yellow lines are the intersections between the ground truth and automatic segmentation results.

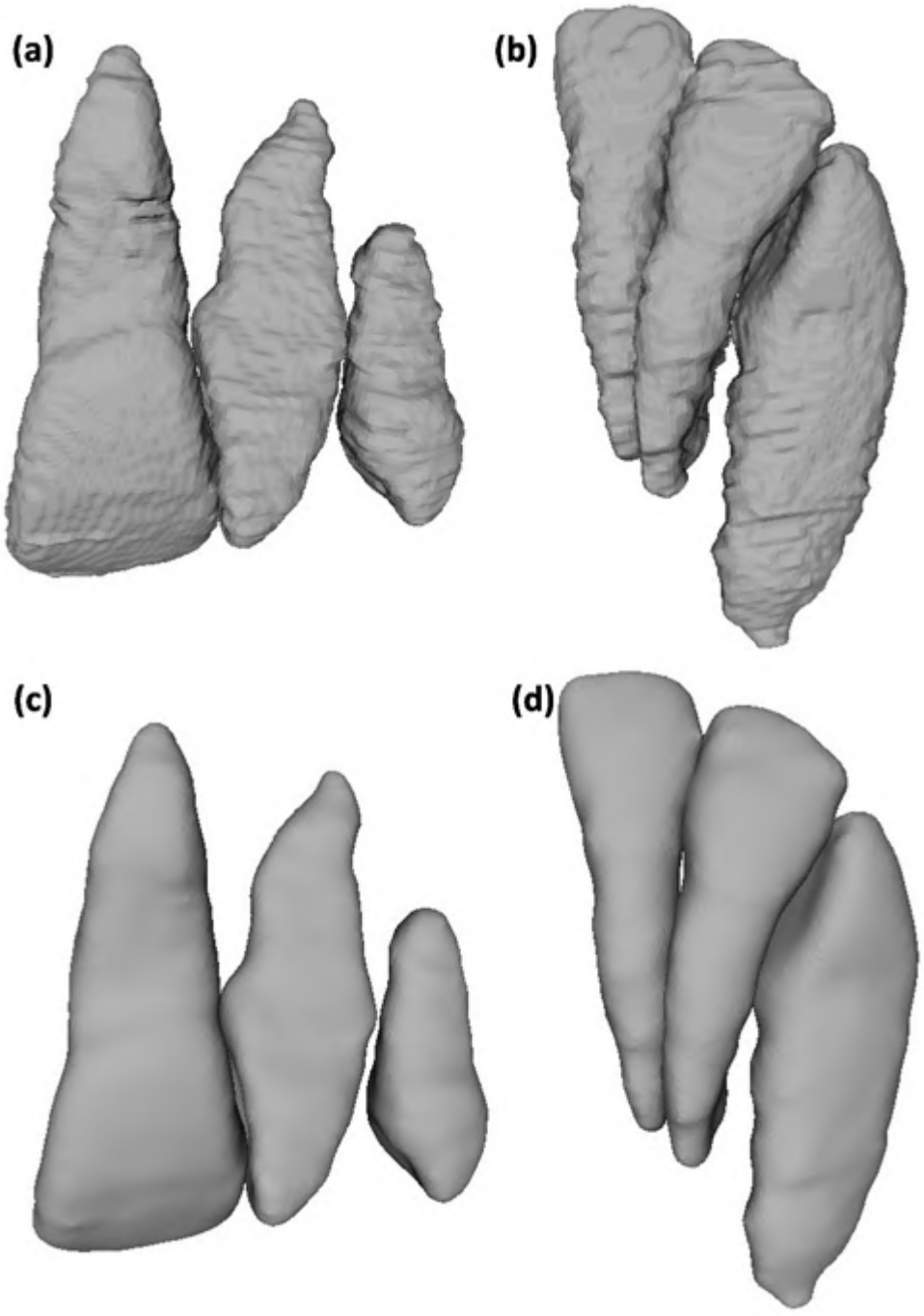

Figure 5.10: 3D segmentation results of the proposed method: (a) shows three maxillary anterior teeth segmented from a patient; (b) shows three mandibular anterior teeth segmented from another patient; (c) and (d) show the smoothed version of (a) and (b) respectively

reliable. The mean accuracy of the proposed method is 0.964 ± 0.011 for JI, 0.981 ± 0.008 for DI, 0.113 ± 0.057 mm for MSD. The mean accuracy of Gao's method is 0.884 ± 0.019 for JI, 0.938 ± 0.011 for DI, 0.229 ± 0.030 mm for MSD. The mean accuracy of Li's method is 0.787 ± 0.079 for JI, 0.879 ± 0.053 for DI, 0.319 ± 0.061 mm for MSD. The proposed method shows an improvement in accuracy over Gao's and Li's level set methods.

5.4 Discussion

5.4.1 Analysis of the functional design

The proposed level set approach is could be used for segmentation of anterior teeth in CBCT. The functionals in Gao & Chae (2010) and Li *et al.* (2005) and new functionals were integrated to improve its segmentation performance. The proposed method has several advantages over other methods. First, a more accurate estimation of intensity distributions inside and outside the tooth is used to drive the contour to approach a more accurate tooth region. Secondly, a more robust shape prior is used to add a more reasonable shape constraint to the contour evolution. Thirdly, the thickness of the tooth dentine wall is used as a new constraint to avoid the leakage problem in the segmentation process. One limitation of this method is that the shape prior provided in the first slice is obtained manually.

Table 5.1: The quantitative performance comparison results between proposed method, Gao's method and Li's method.

	Proposed method			Gao			Li			SMS[1]	
Dataset	Jaccard	Dice	MSD[2](mm)	Jaccard	Dice	MSD	Jaccard	Dice	MSD	Jaccard	Dice
1	0.961	0.980	0.133	0.864	0.927	0.261	0.704	0.827	0.385	0.995	0.997
2	0.959	0.979	0.164	0.878	0.935	0.247	0.806	0.893	0.302	0.999	0.999
3	0.947	0.962	0.187	0.851	0.920	0.289	0.757	0.862	0.362	0.999	1.000
4	0.958	0.977	0.163	0.885	0.939	0.217	0.782	0.877	0.323	0.996	0.998
5	0.976	0.988	0.054	0.884	0.938	0.224	0.826	0.905	0.287	0.999	1.000
6	0.975	0.987	0.063	0.905	0.950	0.195	0.886	0.940	0.231	1.000	1.000
7	0.966	0.983	0.083	0.880	0.936	0.231	0.828	0.906	0.276	0.997	0.998
8	0.978	0.989	0.043	0.917	0.957	0.191	0.864	0.927	0.257	1.000	1.000
9	0.975	0.987	0.061	0.896	0.945	0.221	0.613	0.760	0.431	0.999	1.000
10	0.951	0.975	0.174	0.878	0.935	0.211	0.800	0.889	0.331	0.999	1.000
mean	0.964	0.981	0.113	0.884	0.938	0.229	0.787	0.879	0.319	0.998	0.999
SD[2]	0.011	0.008	0.057	0.019	0.011	0.030	0.079	0.053	0.061	0.002	0.001

[1] SMS :Second manual segmentation
[2] MSD : Mean surface distance
[3] SD: Standard deviation

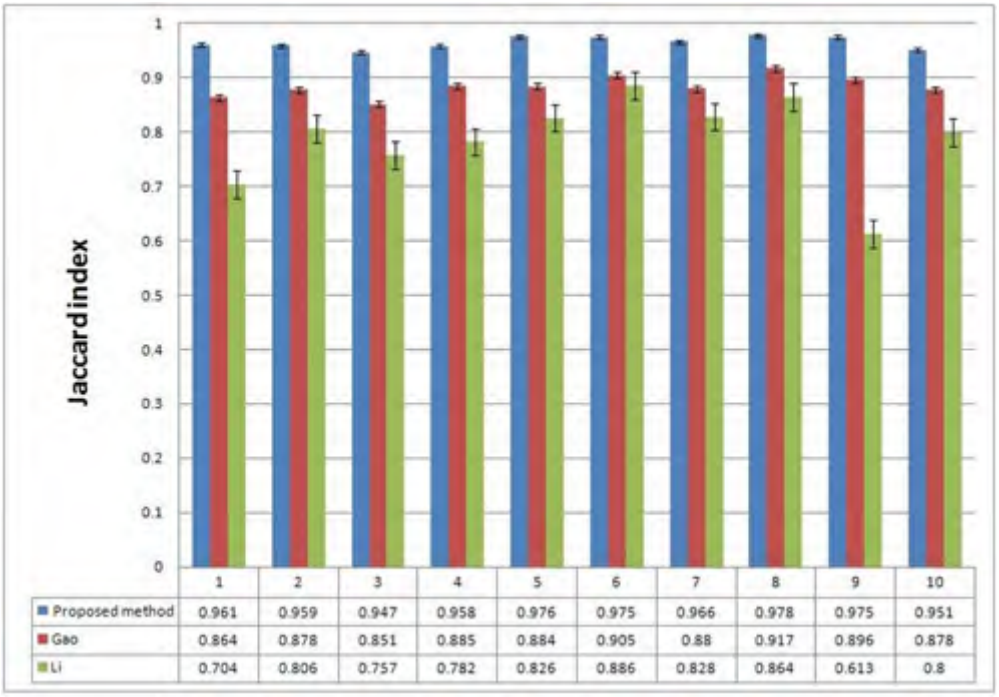

	1	2	3	4	5	6	7	8	9	10
Proposed method	0.961	0.959	0.947	0.958	0.976	0.975	0.966	0.978	0.975	0.951
Gao	0.864	0.878	0.851	0.885	0.884	0.905	0.88	0.917	0.896	0.878
Li	0.704	0.806	0.757	0.782	0.826	0.886	0.828	0.864	0.613	0.8

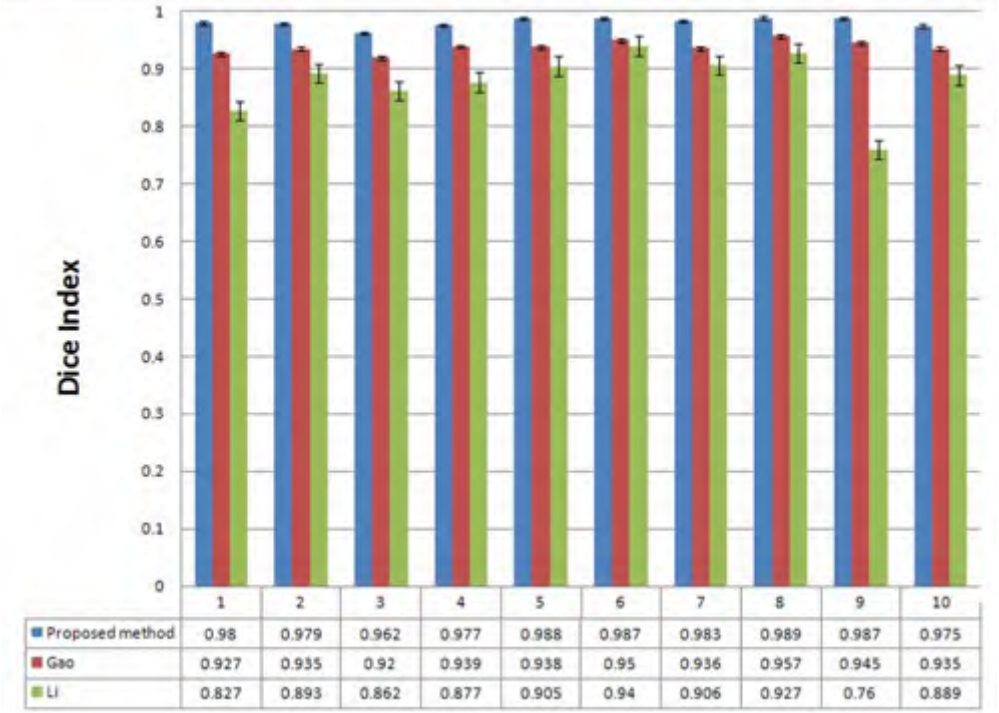

	1	2	3	4	5	6	7	8	9	10
Proposed method	0.98	0.979	0.962	0.977	0.988	0.987	0.983	0.989	0.987	0.975
Gao	0.927	0.935	0.92	0.939	0.938	0.95	0.936	0.957	0.945	0.935
Li	0.827	0.893	0.862	0.877	0.905	0.94	0.906	0.927	0.76	0.889

Figure 5.11: Performance comparison between different methods: top image shows results in terms of the Jaccard index; bottom image shows results in terms of the Dice index

5.4.2 Clinical significance

The ability to visualize the exact spatial orientation of the roots of teeth within the dental arch is an important diagnostic advantage. This advantage is leveraged for teeth which are not visible in the mouth but are buried within the jaw bone. The clinical decision to move a buried tooth into its rightful place within the dental arch or to surgically excise it depends on the clear representation of the positions of the buried tooth and the neighbouring structures. For example, the accurate segmentation of the root of a buried tooth such as a buried upper canine and the neighbouring teeth structures provides orthodontists a clear three-dimensional anatomic map for simulating trajectories and pathways for moving the buried canine into the dental arch. Should the simulations show that the pathways are blocked by neighbouring structures, the surgical option becomes a clinically viable approach to remove the buried canine.

5.4.3 Limitation of the study

Our proposed tooth segmentation is designed for anterior teeth which usually have one single root. For posterior teeth like the premolars or the molars which have multiple roots, segmentation difficulty increases because the topology of the tooth changes when the tooth roots split into different branches. In Gao & Chae (2010), they have to manually select the slice where the tooth splits into multiple branches and decrease the weights on shape prior to allow larger movement of the contour to approach the tooth shape. The parameters in their algorithm have to be manually setup again which is not convenient. Thus both Gao's method and our proposed method suffer from this problem. In future

research, an automatic detection technique could be added into the segmentation algorithm to detect where the topology of tooth shape changes.

5.5 Conclusion

This chapter presents a new level set algorithm to detect the contour of the anterior tooth. We segment the tooth pulp first to obtain a more accurate intensity density function of the tooth dentine. The proposed method also integrates the functionals of existing level set methods (Gao & Chae, 2010; Li *et al.*, 2005) with a dual intensity model for the background, a new shape prior, and a new tooth dentine wall thickness constraint for preventing shrinking and leakage. The experimental results show that the proposed method is more accurate than Gao's method and Li's method for the region of tooth root.

Chapter 6

A 3D interactive tooth movement and collision detection system

In last chapter we presented an approach for anterior teeth segmentation from CBCT images. In this chapter, we present a 3D interactive tooth movement and collision detection system built on the segmented anterior teeth to assist the simulation of tooth movement for clinical cases with impacted upper canine teeth. The details of the system and the case study will be presented in the following sections.

6.1 Introduction

An impacted tooth is a tooth which is blocked so that it is unable to function properly. The maxillary canine is the second most commonly impacted tooth. However, impacted canines are critical to the support of the corners of the upper lip and important in guiding how the upper and lower teeth come together.

Hence, impacted maxillary canine teeth require dental treatment to disimpact the tooth. To move, extract or leave the impacted canine is not a trivial decision for the orthodontist especially when the impacted canine is near to the neighboring teeth. Cone beam CT images are often taken for patients who are diagnosed with impacted canines. Although the raw 3D image can provide the clinicians a rough position of the impacted canine, it is usually difficult for them to carry out a realistic visualisation of the tooth movement needed. Thus, despite the availability of 3D CBCT images, visualising the trajectory for moving the impacted canine into the mouth is difficult without a simulation system that takes into account the structures adjacent to the impacted canine that could obstruct the path of the impacted canine. The motivation is to build a 3D interactive tooth movement and collision detection system. The system can help the clinicians to make orthodontic treatment plans for specific patient especially in impacted canine cases.

6.2 Materials and Methods

6.2.1 Image Data Acquisition

CBCT scanning of the anterior teeth in maxilla were carried out on an anonymous adult female patient. The CBCT image data set was obtained using a Kavo 3D eXam 2nd Generation CBCT scanner with a 0.2mm$\times$0.2mm$\times$0.2mm spatial resolution. The raw image data were stored in DICOM format.

6.2.2 Image Data Format, Segmentation, and 3D surface generation

The level-set-based anterior teeth segmentation presented in Chapter 5 was applied to the CBCT raw image. The total six teeth, including the impacted canine, are segmented. The maxilla was segmented semi-automatically using ITK-SNAP. After segmentation, the triangular surface mesh of the segmented volumetric image was generated using the "isosurface" function in Matlab. The "isosurface" function creates a surface mesh represented by a structure "FV" which contains the faces "FV.faces" and vertices "FV.vertices" of the isosurface. The surface mesh were exported to an STL file for further analyses.

6.2.3 Coordinate system

The 3D CBCT image of the patient can be displayed in a mode called multiplanar reformatting (MPR) which refers to the reconstruction of the image in the coronal and sagittal planes in conjunction with the original axial data set. In the 3D CBCT image, each voxel is assigned a world coordinate relative to the origin which is located in the left upper corner of the first slice in axial plane. The X axis of the system orientate from right of the head to the left, the Y axis from anterior to posterior, the Z axis from inferior to superior (Fig. 6.1).

6.2.4 Camera position and orientation in Matlab

A figure can be viewed in different scenes interactively by using the camera toolbar in Matlab. We will present several key terminologies: (1) The principal axis defines the direction pointing upward on the screen. In Matlab, the principal

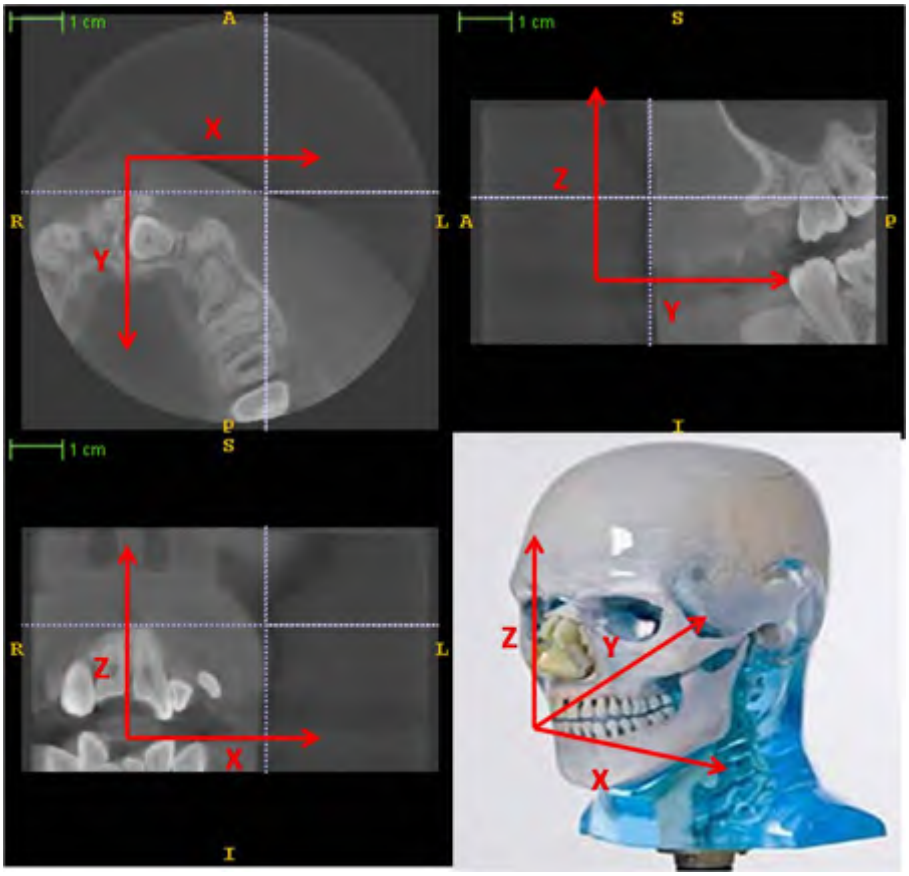

Figure 6.1: The orientation of the CBCT image: the X axis of the system points from right of the head to the left, the Y axis from anterior to posterior, the Z axis from inferior to superior (The six orientations of the head are labeled by six capital letters: A (Anterior), P (Posterior), L (Left), R (Right), S (Superior), I (Inferior).)

axis is typically aligned with the positive Z axis. (2) The camera target defines the point the camera is aiming at. By default, Matlab defines the centroid of the plot box as the camera target. (3) The camera position defines where the camera views the figure. Given the camera position and the camera target, we can calculate the camera direction:

$$camDir = camPos - camTgt \tag{6.1}$$

where $camDir$ is the camera position, $camPos$ is the camera target and $camTgt$ is the camera target. We can then build an orthogonal frame based on the viewing direction and the up vector (the "view frame") as follows:

$$\begin{aligned} zAxis &= \frac{camDir}{|camDir|} \\ upAxis &= \frac{camUpVect}{|camUpVect|} \\ xAxis &= upAxis \times zAxis \\ yAxis &= zAxis \times xAxis \end{aligned} \tag{6.2}$$

where $camUpVect$ and $upAxis$ are in the same direction as the principal axis of the camera and both are vectors, and "$\times$" denotes the cross product between two matrices. The view rotation matrix can be obtained by combining the three axial vectors $xAxis$, $yAxis$ and $zAxis$ into a view rotation matrix:

$$rot = \begin{bmatrix} xAxis \\ yAxis \\ zAxis \end{bmatrix} \tag{6.3}$$

where rot denotes the view rotation matrix.

6.2.5 Point selection with mouse

The tooth movement has two major modes: translation and rotation (which consists of rotation around the long axis of the object body, tipping and torquing). In the translation mode, the point obtained by mouse is directly used as the selected point. In the rotation mode, the point selected by the mouse can not be used directly. The selected point and all the vertices of the object should be transformed into the viewing frame.

$$\begin{aligned} rotatedPointCloud &= V \cdot rot \\ rotatedPointFront &= point \cdot rot \end{aligned} \tag{6.4}$$

where V, a $n \times 3$ matrix, denotes the XYZ positions of the point clouds of the object, $point$ is the position of the point selected by mouse, $rotatedPointCloud$ and $rotatedPointFront$ denotes the transformed positions of the point cloud and the selected point respectively, and "$\cdot$" denotes dot product (scalar product) between two matrices.

Finally, the Z coordinate in this frame is ignored. The X and Y coordinates of all the object points are compared with the mouse click location and the closest point is selected.

6.2.6 Long axis and rotation point of the tooth

The four modes of tooth movement are illustrated in Fig. 6.2. All the four modes of tooth movement are related by a rotation axis, the long axis of the tooth. The

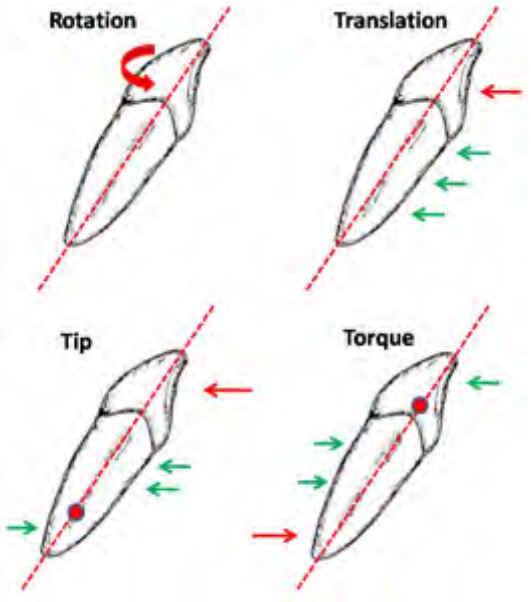

Figure 6.2: Four modes of orthodontic tooth movement.

long axis is an imaginary line that extends through the center of the tooth around which the substance of the tooth is most symmetrically distributed (Fig. 6.3).

In the rotation mode, the tooth is turned around its long axis. In the translation mode, the tooth is pushed by a collection of evenly distributed forces on the same direction so that the vertices of the tooth are moved by a same distance. In the tipping mode, a force is applied to the crown of the tooth, and the crown is moved more than the root around a center of resistance which is located about 1/4 of the whole tooth length (1/3 of root length) from the root apex (Fig. 6.4). In the torquing mode, a force is applied to the root of the tooth, and the root is moved more than its crown around a center of resistance which is located about 1/4 of the whole tooth length from the tooth cusp (Fig. 6.4). To calculate the center of resistance for the tipping and torquing mode, we have to determine the two intersection points on the tooth surface (the tooth root apex and the tooth

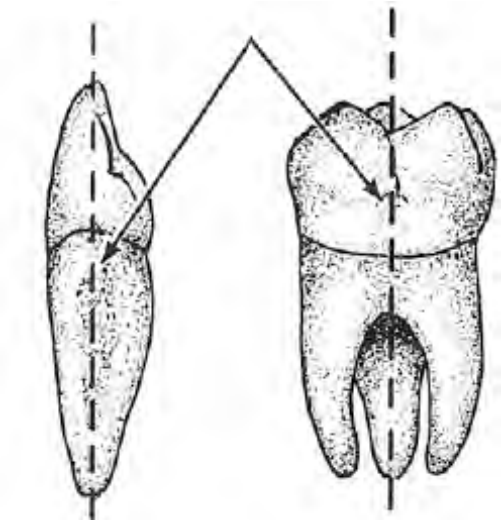

Figure 6.3: Long axis of a tooth.

crown cusp) through which the long axis passes. The two points can be calculated by obtaining the nearest point to the long axis of the vertices at both ends. The two centers of resistance are located 1/4 of the whole tooth length from the root apex and the tooth cusp.

The direction of the long axis can be calculated applying principal component analysis (PCA) (Jolliffe, 2005) to the vertices of the tooth. Consider a dataset X with n samples, each sample is an m-dimensional vector:

$$X = \begin{bmatrix} x(1) \\ \vdots \\ x(n) \end{bmatrix} \text{ where } x(i) = [x_1(i) \dots x_m(i)] \tag{6.5}$$

The covariance matrix Cov is obtained by the following equation

$$Cov = \frac{1}{n-1}(X - \overline{X})^T \cdot (X - \overline{X}) \tag{6.6}$$

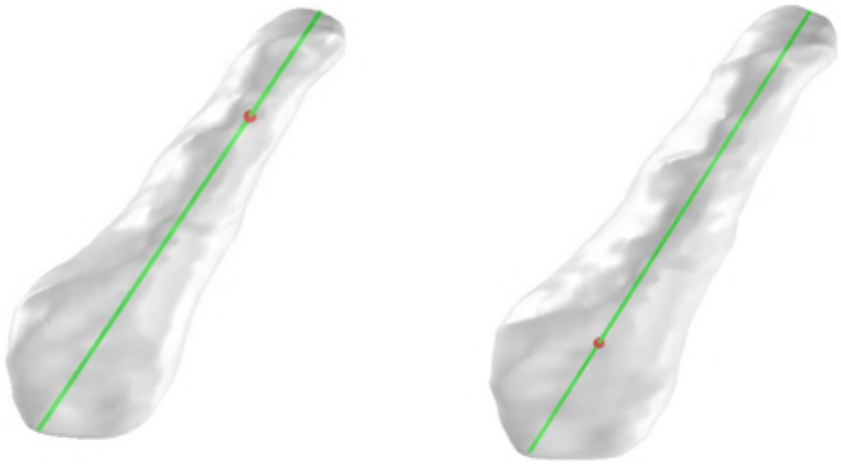

Figure 6.4: The long axis of tooth and rotation points. The left image shows the long axis (in green) and the rotation point (in red) in the mode of tipping; The right image shows the long axis (in green) and the rotation point (in red) in the mode of torquing

where $\overline{X}$ is the mean of value of X. The $m \times m$ matrix Cov may have at most m pairs of eigenvectors and eigenvalues if Eq. (6.7) is satisfied:

$$Cov \cdot V = V \cdot \Lambda \tag{6.7}$$

where V is an $m \times m$ matrix constructed by the m eigenvectors of Cov in the columns, Λ is an $m \times m$ diagonal matrix constructed by the m eigenvalues of Cov in the diagonal entries. The eigenvector corresponding to the maximal eigenvalue of the m eigenvalues gives the first principal component. The first principal component gives the direction in which the variation of the data is maximized.

In this study, the coordinates of the tooth surface points are in 3D space,

and thus m equals to 3. n is the total number of the surface points of the tooth. Using PCA, we compute the eigenvectors and eigenvalues of the dataset, and the eigenvector corresponding to the maximal eigenvalue gives the first principal component. The direction of the long axis of the tooth should be the direction that accounts for the largest proportion of the distance variation. Thus the first principal component calculated using PCA gives the direction of the long axis.

According to its definition, the long axis should go through the center of the tooth, which is approximately the mean coordinate of the surface points. The long axis can then be fixed by the direction calculated using PCA and the position of the tooth center. After fixing the long axis, the two rotation points in the mode of tip and the mode of torque can be calculated along the long axis (Fig. 6.4).

6.2.7 Collision detection

In the simulation of the movement of an impacted canine, we want to know whether the moving tooth contacts a neighboring tooth. If it does, then the impacted tooth is stuck and can't be moved further in this direction, which is a common situation in clinical practice. Collision detection is a technique to find the existence of contact between pairs of objects in simulation (Ericson, 2004). We use the "coldetect" function implementing the V-COLLIDE collision detection algorithm distributed by Kochenderfer (Hudson *et al.*, 1997). V-COLLIDE is a collision detection library designed to operate on triangulated meshes. A three-phase hierarchical architecture is used by V-COLLIDE: an initial n-body test to detect possible contacting pairs of objects, oriented bounding box trees

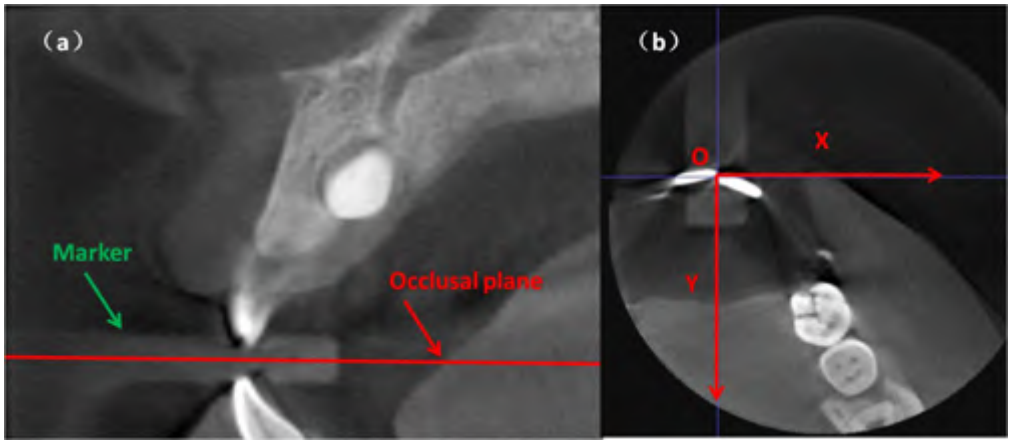

Figure 6.5: Occlusal plane: (a) Sagittal view; (b) Axial view

(OBBTree) (Gottschalk *et al.*, 1996) are used to detect possible contacting pairs of triangles, and a final test to detect the overlapping of pairs of triangles.

6.2.8 Validation

We evaluated the result of the tooth movement by the average distance (AD) between the dental cusps and the maxillary dental arch line. The AD of the pre and planned treatment were calculated and compared.

6.2.8.1 Calculation of AD

Before the calculation of the AD, we have to generate the occlusal plane (OP), which separates the upper and lower jaw. A rectangular marker was bitten by the patient as shown in Fig. 6.5 (a). The OP is the plane which passes through the middle of the marker. The X axis of the OP points from the right of the head to the left, the Y axis from anterior to posterior, and the origin of the OP is determined after we find out the maxillary dental arch line (Fig. 6.5 (b)).

The maxillary dental arch line is calculated as follows. We select an axial slice where the image includes most part of maxillary teeth, which is located above the OP. To obtain the maxillary dental arch line, we have to define a region of maxillary dental arch, which covers the maxillary teeth in the slice (Fig. 6.6 (a)). Morphological functions in the Matlab software are used to find the one pixel thick skeleton of the binary mask of the region of maxillary dental arch (Fig. 6.6 (b)). 2D connectivity analysis is then applied to automatically remove the short branches in the skeleton to obtain the representative maxillary dental arch line (Fig. 6.6 (c)). The upper left point of the maxillary dental arch line is set as the origin of the OP (Fig. 6.6 (d)).

To obtain the cusps of the maxillary teeth, we move the OP upward. The cusps could be easily identified as the points where the plane touches each tooth. The detected cusps of the teeth are then projected back onto the OP. Finally, the distances between the projected cusps and the maxillary dental arch line are calculated.

6.3 Experiment and results

6.3.1 The system

The 3D interactive tooth movement and collision detection system has three major functions:

- Collision detector “COLDETECT version 1.0”;
- Interactive object movement function “objmove.m”;
- Graphical user interface (GUI) function “toothmove.m”.

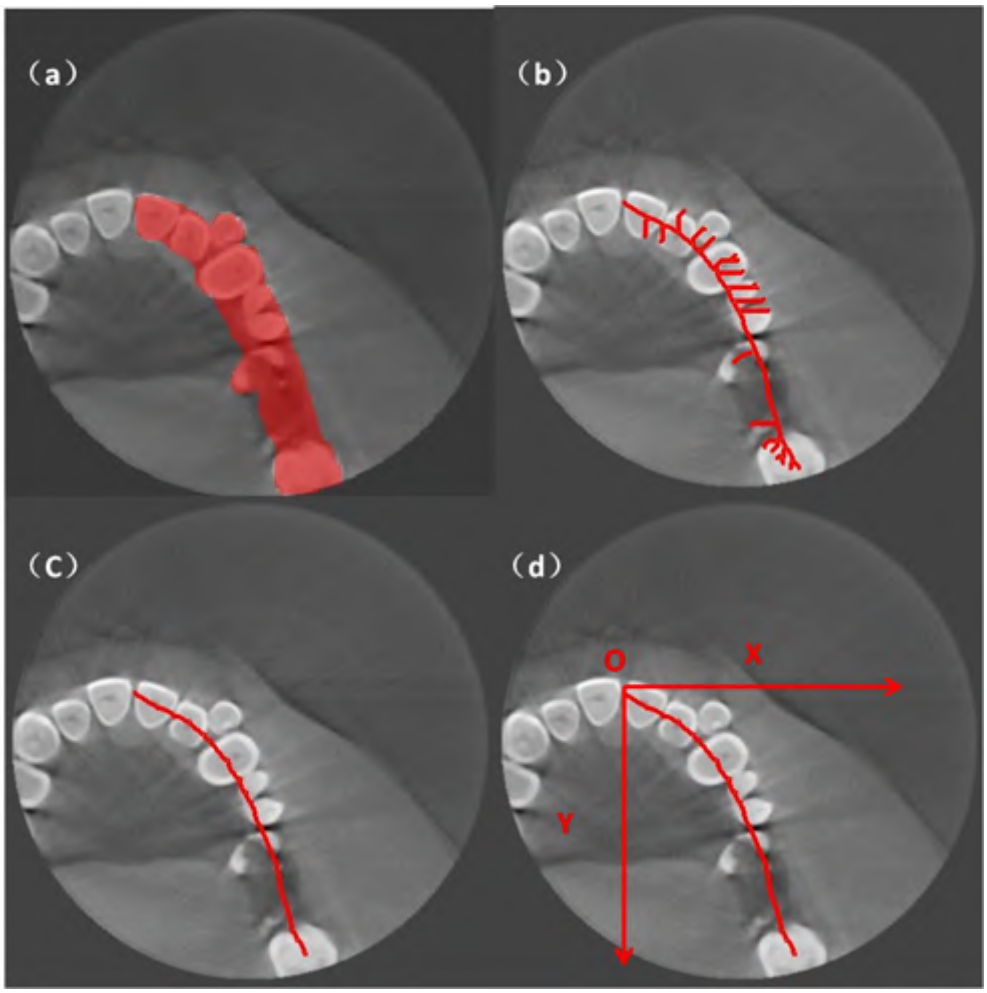

Figure 6.6: Steps to find the maxillary dental arch line. (a) define a region of maxillary dental arch; (b) skeletonize the region; (c) remove the short branches; (d) set the origin of the OP

The final GUI and four modes of tooth movement are shown in Fig. 6.7. The user can use the mouse to control the movement of the impacted canine. In the system, the user can select one of the four modes to translate or rotate the tooth. The collision detector detects whether the impacted canine come into contact with any of the four anterior teeth. When collision happens, the flag of the detector will turn from the value "0" to "1" and warn the user that the impacted canine can't be moved any further.

6.3.2 A case study

The segmented teeth and the maxilla are shown in Fig. 6.8. An extra canine is stuck behind the anterior teeth of the patient. We will show how to use the 3D interactive system to find a path for the impacted canine movement. Other solutions for this impacted canine cases are: to remove the impacted canine or leave it in its original position, both of which will not be discussed in this thesis. The sequence of actions is:

- The lateral incisor and the canine are removed to create space for the impacted canine movement (Fig. 6.9).
- Find the desired position for the impacted canine (Fig. 6.10).
- Move the impacted tooth gradually into the desired position with the interactive system. The interval steps are shown in Fig. 6.11.

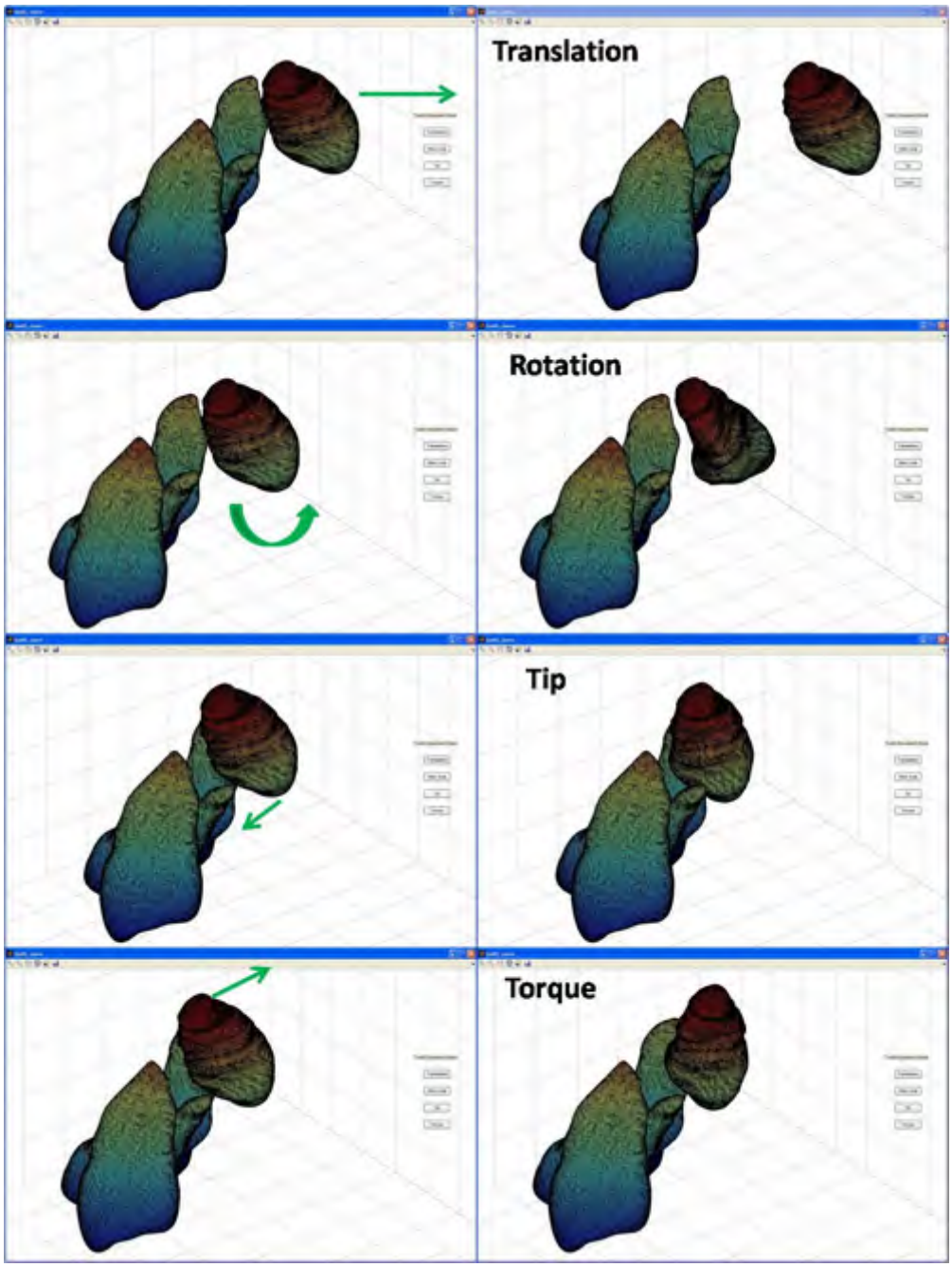

Figure 6.7: GUI of the system and four modes of tooth movement.

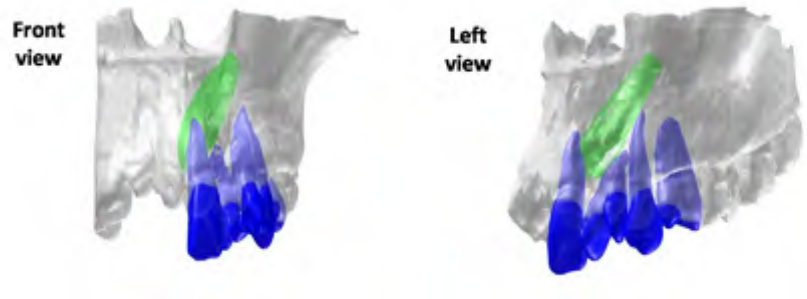

Figure 6.8: The segmented teeth and the maxilla. The anterior teeth are shown in blue and the impacted canine is shown in green. The maxilla is shown as a relative transparent grey body.

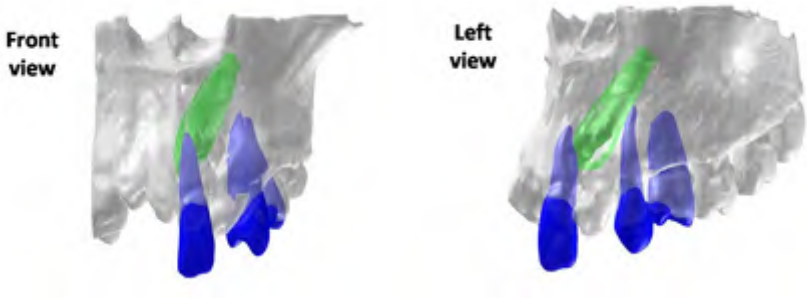

Figure 6.9: The lateral incisor and the canine are removed.

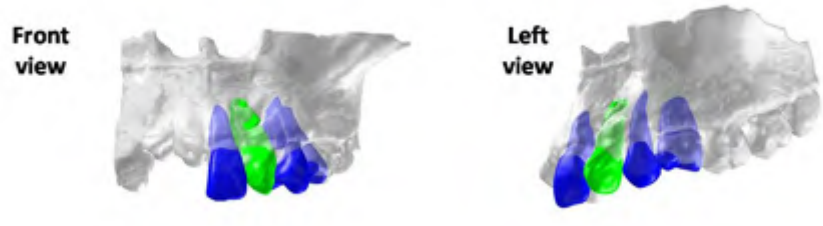

Figure 6.10: The desired position for the impacted canine.

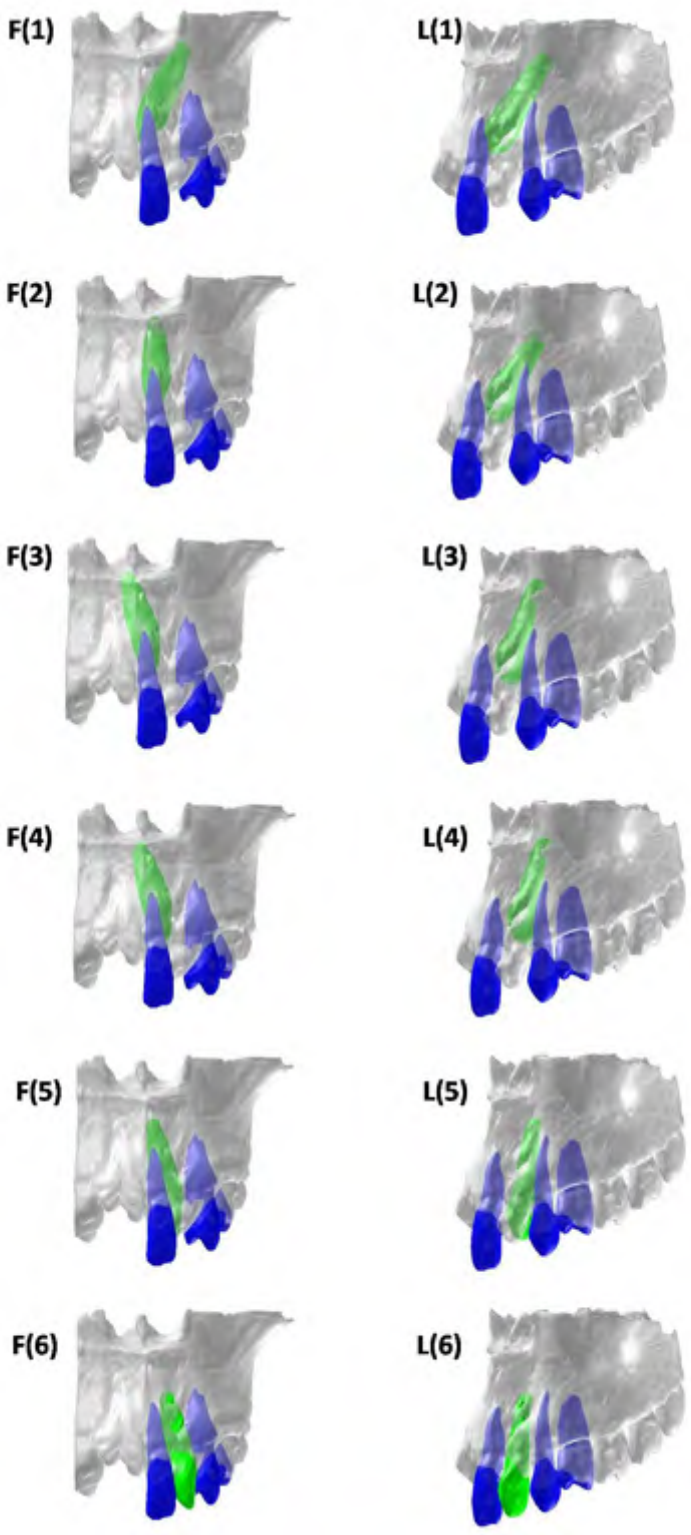

Figure 6.11: Tooth movement process. F(1)-F(6) shows the front view of the movement process; L(1)-L(6) shows the left view of the movement process.

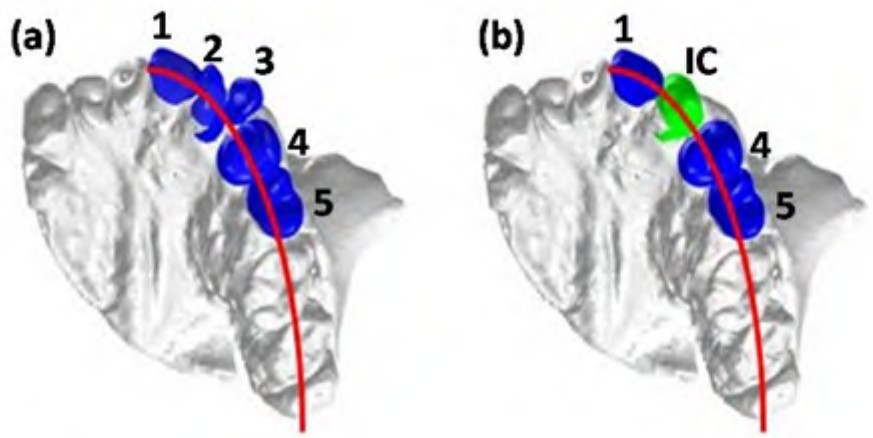

Figure 6.12: Result of the planned treatment (bottom view). (a) pre treatment; (b) planned treatment. The red line is the maxillary dental arch line.

6.3.3 Tooth movement results

In the treatment plan given above, the maxillary lateral incisor, the impacted canine and the impacted canine are involved. Thus we first calculate the average distance between the projected cusps of the first two removed teeth and the maxillary dental arch line. The distance between the projected cusp of the moved impacted canine and the maxillary dental arch line is also calculated. The distances between the projected cusps of the first two removed teeth and the maxillary dental arch line are 0.849mm and 4.968mm giving an average distance 2.908mm. The distance between the projected cusp of the moved impacted canine and the maxillary dental arch line is 1.414mm. The moved impacted canine is fitted better to the maxillary dental arch line than the two removed teeth (Fig. 6.12).

6.4 Discussion and conclusion

A 3D interactive tooth movement and collision detection system was built to provide clinicians a realistic anatomic simulation system to plan the trajectory for moving the impacted canine into the mouth. The system can also be used to educate dentistry students by showing a 3D environment of the impacted canine movement case. In contrast with raw CBCT images, the system offers the user a 360 degree view of the 3D environment. The four modes of tooth movement can well simulate the orthodontic tooth movement in practice. The system can be used for any specific patient as long as his teeth can be segmented from CBCT images.

Chapter 7

Conclusion and Future Work

In this chapter, we conclude the thesis with an overview of achievements and suggestions for future work.

7.1 Overview

We have presented a region-growing based method for hard-tissue segmentation from MR images and a level-set based method for hard-tissue segmentation from CBCT images in this thesis. The region-growing based method is chosen to segment the mandible from MR images because it regards the mandibular shape as a set of connected sub-regions and segments these multiple regions from the surrounding tissue. Region-growing based methods are more suitable than level-set based methods for segmentation problems where the ROI has multiple regions. The level-set based method is chosen to segment the anterior teeth from CBCT images because it is more suitable than the region growing method for segmentation problems where the ROI is a single region. The level-set based method can be combined easily with the shape prior of the ROI, which could increase the accuracy of the segmentation. Such shape priors play a vital role in

the tooth segmentation problem from CBCT images.

The rule-constrained seedless region growing framework should also be applicable for other hard tissue segmentation from MR images where the ROI to be segmented is relatively large but fragmented into several sub-regions. The improved level-set-based method should also be applicable for other image segmentation problems where the ROI to be segmented has relatively weak edges but whose shape does not change much in consecutive slices.

7.1.1 Segmentation of mandibular body

We have presented a two-stage rule-constrained seedless region growing image processing approach for segmentation of the body of the mandible. The sequence starts with a 3D seedless region growing for the purpose of detecting a large portion of the trabecular bone (TB) regions of the mandible after an initial threshold. This stage is followed by a rule-constrained 2D segmentation of each MR axial slice to merge the remaining portions of the TB regions previously undetected at lower intensity levels. The preceding two steps were repeated with different thresholds to detect the cortical bone (CB) regions. The penultimate step involved the merging of TB and CB regions to further define the shape of the body of the mandible. A series of morphological processes rounds up this approach to complete the definition of the mandibular body. It is the first research report on mandible segmentation in MR images.

Within the limitation of the study, this method is also more accurate than the conventional region growing (CRG) method and 3D level set. The reason why the accuracy of CRG is lower is that it can only find a relatively small

portion of the TB region. With 3D level set, leak-out problem easily occurs because the method can't deal well with TB having similar intensity values with the surrounding regions. This similarity causes the detected active contour to expand beyond the TB region and develop into a big bubble.

We have presented steps to determine the validity of magnetic resonance imaging (MRI) as a non-ionising imaging modality for generating a realistic shape of the mandible and to evaluate the precision of the mandibular shape. Three adult male subjects underwent CT scanning and MRI. A semi-automated image processing method was applied to segment the CT and MR images, from which the segmented paired images were co-registered with the ICP method. The similarity of paired co-registered mandibular models was assessed by volumetric measurements, 3D surface distance measurements, the Dice coefficient for agreement of paired volumes, and bucco-lingual "bone shape" thickness measurements. The Wilcoxon signed-rank test was applied to the comparative measurements. A realistic shape of the mandibular body, ramus and sympmphyseal region has been generated from the MR images. However, anatomical areas at the coronoid processes and condylar heads generated from the MRI were less precise when compared with those generated from CT imaging.

7.1.2 Segmentation of anterior teeth

We have presented an improved level-set-based method to extract the shapes of anterior teeth from CBCT images. A contour initialization technique was applied followed by a new level set algorithm to detect the contour of the tooth. The presented method has three novelties: 1) a more accurate estimation of

intensity distributions of the tooth root is used; 2) a more robust shape prior is used to add a more reasonable shape constraint on the contour evolution; and 3) the thickness of tooth dentine wall is used as a new constraint to avoid leakage. The experimental results show that the proposed method is more accurate than Gao's method and Li's method for the region of tooth root.

The segmented anterior teeth can be directly used for a 3D interactive tooth movement and collision detection system to assist the clinicians to make treatment planning. The system can also be used to educate dentistry students by showing a 3D environment of the impacted canine movement case. In contrast with raw CBCT images, the system offers the user 360 degree view of the 3D environment. The four modes of tooth movement can simulate well the orthodontic tooth movement in practice.

7.2 Future Work

The pilot study of reconstruction of mandibular shape from magnetic resonance imaging is carried out on only three pairs of image data sets. The difficulties of data acquisition lie in: (1) The study is carried out on living patients, thus it will be costly to collect enough data. (2) The study is carried out on both CBCT scanner and MRI scanner. The former modality will expose the patients to high radiation, and the latter one will take almost five minutes to acquire the data. If the above difficulties can be solved, the experiment results will be more convincing.

Our proposed tooth segmentation is designed for the anterior teeth which have single roots. For posterior teeth like the premolar or the molar which usu-

ally has multiple teeth, segmentation difficulty will increase because the topology of the tooth will change when the tooth root splits into different branches. Gao's method can be applied to posterior teeth. However, they have to manually select the slice where the topology of the tooth changes. And the parameters have to be setup again manually.

The Gao's method and our proposed method both use segmentation result of previous slice as the shape prior of the next slice. This may introduce accumulated error and decrease the segmentation accuracy. A more reliable shape prior should be found to ensure the segmentation consistency.

In Chapter 6, we built a 3D interactive tooth movement and collision detection system. The final target of the project is to develop an automated or semi-automated path planning algorithm for patient specific tooth movement cases. Before the system is built, several engineering problems have to be solved:

- The outer boundary of the maxilla shape has to be accurately defined. The 3D surface of the maxilla is the solution space for the tooth movement. The movement is not allowed if any part of the tooth touches the boundary of the maxilla.

- A path planning algorithm for a 3D object should be developed. The algorithm should consider the constraint of the solution space based on the shape of the patient specific maxilla.

- The final challenge of the project lies in that the tooth can't be moved as a free body. Thus when the tooth is moved in different mode, a different constraint should be added into the path planning algorithm.

References

(????). 22

ADAMS, R. & BISCHOF, L. (1994). Seeded region growing. *IEEE Transactions on Pattern Analysis and Machine Intelligence*, **16**, 641–647. 26, 42

ALUSH, A., GREENSPAN, H. & GOLDBERGER, J. (2010). Automated and interactive lesion detection and segmentation in uterine cervix images. *IEEE Transactions on Medical Imaging*, **29(2)**, 488C501. 30

BABICH, G. & CAMPS, O. (1996). A comparative study among pattern classifiers in interactive image segmentation. *IEEE Transactions on Pattern Analysis and Machine Intelligence*, **18**, 567–570. 30

BARANDIARAN, I., MACIA, I., BERCKMANN, E., WALD, D., DUPILLIER, M., PALOC, C. & GRANA, M. (2009). An automatic segmentation and reconstruction of mandibular structures from ct-data. *Intelligent Data Engineering and Automated Learning*, **5788**, 649–655. 5

BEICHEL, R., MITCHELL, S., SORANTIN, E., LEBERL, F., GOSHTASBY, A. & SONKA, M. (2001). Shape- and appearance-based segmentation of volu-

metric medical images. *Proc. IEEE Int. Conf. Image Process.*, **2**, 589C592. 38

BEZDEK, J., HALL, L. & CLARKE, L. (1993). Review of mr image segmentation techniques using pattern recognition. *Medical Physics*, **20**, 1033–1048. 24, 30, 32

BOURGEAT, P., FRIPP, J., STANWELL, P., RAMADAN, S. & OURSELIN, S. (2007a). Mr image segmentation of the knee bone using phase information. *Medical Image Analysis*, **11**, 325–335. 42

BOURGEAT, P., FRIPP, J., STANWELL, P., RAMADAN, S. & OURSELIN, S. (2007b). Mr image segmentation of the knee bone using phase information. *Medical Image Analysis*, **11**, 325–335. 65

BRENNER, D., ELLISTON, C., HALL, E. & BERDON, W. (2001). Estimated risks of radiation-induced fatal cancer from pediatric ct. *American Journal of Roentgenology*, **176(2)**, 289–96. 82

BURSTEIN, D. & GRAY, M. (2003). New mri techniques for imaging cartilage. *The Journal of Bone and Joint Surgery, American Volume*, **85A (Suppl. 2)**, 70–77. 64

C. LEE, T.K., S. HUN & UNSER, M. (1998). Unsupervised connectivity-based thresholding segmentation of midsaggital brain mr images. *Computers in Biology and Medicine*, **28**, 309–338. 26

CAM, L. & LUCIEN (1990). Maximum likelihood - an introduction. *ISI Review*, **58(2)**, 153–171. 30

CAO, L., SHI, Z. & CHENG, E. (2002). Fast automatic multilevel thresholding method. *Electronics Letters*, **38**, 868–870. 25

CASELLES, V., KIMMEL, R. & SAPIRO, G. (1997). Geodesic active contours. *International Journal of Computer Vision*, **22**, 61–79. 35

CATE, A. (1998). *Oral Histology: Development, Structure and Function*. Mosby, St. Louis, 5th edn. 14, 15

CHAN, T. & VESE, L. (2001). Active contour without edges. *IEEE Transactions on Image Processing*, **10**, 266–277. 83

CHANG, Y., XIA, J., YUAN, P., KUO, T., XIONG, Z., GATENO, J. & ZHOU, X. (2013). 3d segmentation of maxilla in cone-beam computed tomography imaging using base invariant wavelet active shape model on customized two-manifold topology. *Journal of X-Ray Science and Technology*, **21**, 251–282. 7, 38

CHEN, C., LUO, J. & PARKER, K. (1998). Image segmentation via adaptive k-mean clustering and knowledge-based morphological operations with biomedical applications. *IEEE Transactions on Image Processing*, **7(12)**, 1673–83. 32

CHEN, T. & METAXAS, D. (2005). A hybrid framework for 3d medical image segmentation. *Medical Image Analysis*, **9**, 547–565. 84

CHOW, C. & KANEKO, T. (1972). Automatic boundary detection of the left-ventricle from cineangiograms. *Computers and Biomedical Research*, **5**, 388–410. 25

CHUANG, K., TZENG, H., CHEN, S., WU, J. & CHEN, T. (2006). Fuzzy c-means clustering with spatial information for image segmentation. *Computerized Medical Imaging and Graphics*, **30(1)**, 9–15. 32

CHYZHYK, D., AYERDI, B. & MAIORA, J. (in press). Active learning with bootstrapped dendritic classifier applied to medical image segmentation. *Pattern Recognition Letters*. 30

COHEN, L. (1991). On active contour models and balloons. *CVGIP: Image Understanding*, **53**, 211–218. 35

COHNEN, M., KEMPER, J., MOBES, O., PAWELZIK, J. & MODDER, U. (2002). Radiation dose indental radiology. *European Radiology*, **12(3)**, 634–7. 20

COOTES, T., TAYLOR, C., COOPER, D. & GRAHAM, J. (1995). Active shape models - their training and application. *Computer Vision and Image Understanding*, **61**, 38C59. 38

COOTES, T., EDWARDS, G. & TAYLOR, C. (1998). Active appearance models. *Proc. Eur. Conf. Comput. Vis.*, **2**, 484C498. 38

CREMERS, D., TISCHHAUSER, F., WEICKERT, J. & SCHNORR, C. (2002). Diffusion snakes: Introducing statistical shape knowledge into the mumford-shah functional. *International Journal of Computer Vision*, **50**, 295–313. 35

DANFORTH, R. & CLARK, D. (2000). Effective dose from radiation absorbed during a panoramic examination with a new generation machine. *Oral*

Surgery, Oral Medicine, Oral Pathology, Oral Radiology, and Endodontology, **89(2)**, 236–43. 20

DICE, L. (1945). Measures of the amount of ecologic association between species. *Ecology*, **26**, 297–302. 70, 102

DOGDAS, B., SHATTUCK, D. & LEAHY, R. (2005). Segmentation of skull and scalp in 3-d human mri using mathematical morphology. *Human Brain Mapping*, **26**, 273–285. 41

DOKLDAL, P., BLOCH, I., COUPRIE, M., RUIJTERS, D., URTASUN, R. & GARNERO, L. (2003). Topologically controlled segmentation of 3d magnetic resonance images of the head by using morphological operators. *Pattern Recognition*, **36**, 2463–2478. 41

DUDA, R., HART, P. & STORK, D. (2000). *Pattern Classification*. John Wiley and Sons, 2nd edn. 30

DULA, K., MINI, R., VAN DER STELT, P., LAMBRECHT, J., SCHNEEBERGER, P. & BUSER, D. (1996). Hypothetical mortality risk associated with spiral computed tomography of the maxilla and mandible. *European Journal of Oral Sciences*, **104(5-6)**, 503–10. 20

EDER, D., BREALEY, R., BERTRAM, J., EDER, D., KAMINSKY, S. & WATERS, J. (2003). *Laboratory Atlas of Anatomy and Physiology*. McGraw-Hill, New York, 4th edn. 1, 2

EL-BAZ, A., FARAG, A., GIMELFARB, G., FALK, R., EL-GHAR, M. & ELDIASTY, T. (2006). A framework for the automatic segmentation of lung nod-

ules from low dose chest ct scans. *Proceedings of the international conference on pattern recognition (ICPR'06)*, 611–614. 22

ERICSON, C. (2004). *Real-Time Collision Detection*. CRC Press. 121

FABIJASKA, A. (2009). Two-pass region growing algorithm for segmenting airway tree from mdct chest scans. *Computerized Medical Imaging and Graphics*, **33**, 537–546. 26, 43

FAN, J., YAU, D., ELMAGARMID, A. & AREF, W. (2001). Automatic image segmentation by integrating color-based extraction and seeded region growing. *IEEE Transactions on Image Processing*, **10**, 1454–1466. 27

FAN, J., ZENG, G., BODY, M. & HACID, M. (2005). Seeded region growing: an extensive and comparative study. *Pattern Recognition Letters*, **26**, 1139–1156. 27

FARAG, A., AHMED, M., EL-BAZ, A. & HASSAN, H. (2005). *Handbook of biomedical image analysis, volume I: segmentation models*. Kluwer Academic/Plenum Publishers, New York. 22

FARINA, D., BODIN, C., GANDOLFI, S., GASPERI, W., BORGHESI, A. & MAROLDI, R. (2009). Tmj disorders and pain: Assessment by contrast-enhanced mri. *European Journal of Radiology*, **70**, 25–30. 64

FREIXENET, J., MUNOZ, X., RABA, D., MARTI, J. & CUFI, X. (2002). Yet another survey on image segmentation: Region and boundary information integration. *European Conference on Computer Vision*, 408–422. 24

GAO, H. (2010). Individual tooth segmentation from ct images using improved level set method for orthodontic treatment planning. *PhD Thesis*. 88

GAO, H. & CHAE, O. (2010). Individual tooth segmentation from ct images using level set method with shape and intensity prior. *Pattern Recognition*, **43**, 2406–2417. 6, 35, 84, 86, 87, 88, 90, 92, 93, 94, 95, 96, 97, 100, 102, 103, 107, 110, 111

GIBBS, P., BUCKLEY, D., BLACKBAND, S. & HORSMAN, A. (1996). Tumour volume detection from mr images by morphological segmentation. *Physics in Medicine and Biology*, **41**, 2437–2446. 28

GIBBS, S. (2000). Effective dose equivalent and effective dose: comparison for common projections in oral and maxillofacial radiology. *Oral Surgery, Oral Medicine, Oral Pathology, Oral Radiology, and Endodontology*, **90(4)**, 538–45. 20

GOLDMAN, L. (2008). Principles of ct: Multislice ct. *Journal of Nuclear Medicine Technology*, **36**, 57–68. 18

GOLLMER, S. & BUZUG, T. (2012). Fully automatic shape constrained mandible segmentation from cone-beam ct data. *2012 9th IEEE International Symposium on Biomedical Imaging*, 1272–1275. 7

GOTTSCHALK, S., LIN, M. & MANOCHA, D. (1996). Obbtree: A hierarchical structure for rapid interference detection. *SIGGRAPH '96 Proceedings of the 23rd annual conference on Computer graphics and interactive techniques*, 171–180. 122

GREENSPAN, H., RUF, A. & GOLDBERGER, J. (2006). Constrained gaussian mixture model framework for automatic segmentation of mr brain images. *IEEE Transactions on Medical Imaging*, **25(9)**, 1233–1245. 22

GRIMSON, W., ETTINGER, G., KAPUR, T., LEVENTON, M., W.M.WELLS & *et al.* (1997). Utilizing segmented mri data in image-guided surgery. *Int. J. Patt. Rec. Art. Intel.*, **11**, 1367–1397. 22

HARALICK, R. & SHAPIRO, L. (1985). Image segmentation techniques. *Comput. Vis. Graph. Im. Proc.*, **29**, 100–132. 24

HARTIGAN, J. & WONG, M. (1979). Algorithm as 136: A k-means clustering algorithm. *Journal of the Royal Statistical Society: Series C (Applied Statistics)*, **28**, 100–108. 94, 95

HASHEMI, R., BRADLEY, W. & LISANTI, C. (2010). *MRI: The Basics*. Lippincott Williams & Wilkins, Philadelphia, 3rd edn. 3, 21

HEILAND, M., SCHULZE, D., ROTHER, U. & SCHMELZLE, R. (2004). Postoperative imaging of zygomaticomaxillary complex fractures using digital volume tomography. *Journal of Oral and Maxillofacial Surgery*, **62(11)**, 1387–91. 20

HELD, K., KOPS, E., KRAUSE, B., WELLS, W., KIKINIS, R. & *et al.* (1997). Markov random field segmentation of brain mr images. *IEEE Transactions on Medical Imaging*, **16(6)**, 878–886. 31

HEO, H. & CHAE, O. (2004). Segmentation of tooth in ct images for the 3d reconstruction of teeth. *Proceedings of SPIE-IST Electronic Imaging*, 455–466. 83

HOUNSFIELD, G. (1973). Computerized transverse axial scanning (tomography): Part i. description of system. *British Journal of Radiology*, **46**, 1016–1022. 16

HUDSON, T., LIN, M., COHEN, J., GOTTSCHALK, S. & MANOCHA, D. (1997). V-collide: Accelerated collision detection for vrml. *In Proceedings of VRML*, 119–125. 121

ICRP (2007). Recommendations of the international commission on radiological protection (users edition). icrp publication 103 (users edition). *Ann. ICRP 2007*, **37**, 2–4. 64

JACCARD, P. (1912). The distribution of flora in the alpine zone. *New Phytologist*, **11**, 37–50. 102

JIANG, X. & MOJON, D. (2003). Adaptive local thresholding by verification-based multithreshold probing with application to vessel detection in retinal images. *IEEE Transactions on Pattern Analysis and Machine Intelligence*, **25**, 131–137. 25, 26

JOLESZ, F., NABAVI, A. & KIKINIS, R. (2001). Integration of interventional mri with computer-assisted surgery. *Journal of Magnetic Resonance Imaging*, **13**, 69–77. 22

JOLLIFFE, I. (2005). *Principal Component Analysis*. Wiley Online Library. 119

JOSHI, S., MILLER, M. & GRENANDER, U. (1997). On the geometry and shape of brain sub-manifolds. *Int. J. Patt. Rec. Art. Intel.*, **11**, 1317–1343. 31

KAINMUELLER, D., LAMECKER, H., SEIM, H., ZINSER, M. & ZACHOW, S. (2009). Automatic extraction of mandibular nerve and bone from cone-beam ct data. *Medical Image Computing and Computer Assisted Intervention*, 76–83. 6

KAPILA, S., CONLEY, R. & HARRELL, W. (2011). The current status of cone beam computed tomography imaging in orthodontics. *Dentomaxillofacial Radiology*, **40**, 24–34. 64

KASS, M., WITKIN, A. & TERZOPOULOS, D. (1988). Snakes: Active contour models. *International Journal of Computer Vision*, **1**, 321–331. 33

KEYHANINEJAD, S., ZOROOFI, R., SETAREHDAN, S. & SHIRANI, G. (2006). Automated segmentation of teeth in multi-slice ct images. *IET International Conference on Visual Information Engineering*, 339–344. 6

KHOO, V., DEARNALEY, D., FINNIGAN, D., PADHANI, A., TANNER, S. & LEACH, M. (1997). Imagnetic resonance imaging (mri): considerations and applications in radiotheraphy treatment planning. *Radiotherapy & Oncology*, **42**, 1–15. 22

KIM, D., CHUNG, S. & PARK, J. (2006). Automatic navigation path generation based on two-phase adaptive region-growing algorithm for virtual angioscopy. *Medical Engineering & Physics*, **28**, 339–347. 26, 43

KITTLER, J. & ILLINGWORTH, J. (1986). Minimum error thresholding. *Pattern Recognition*, **19**, 41–47. 26

LAMECKER, H., ZACHOW, S., WITTMERS, A., WEBER, B., HEGE, H., ELSHOLTZ, B. & *et al.* (2006). Automatic segmentation of mandibles in low-dose ct-data. *International Journal Computer Assisted Radiology and Surgery*, **1**, 393–395. 7, 38

LI, C., XU, C., GUI, C. & FOX, M. (2005). Level set evolution without re-initialization: A new variational formulation. *Proceedings of the IEEE CVPR*, 430–436. 35, 36, 88, 91, 101, 103, 107, 111

LI, S. (1995). *Markov Random Field Models in Computer Vision*. Springer. 31

LIEBGOTT, B. (2011). *The Anatomical Basis of Dentistry*. MOSBY ELSEVIER. 2

LIN, Z., JIN, J. & TALBOT, H. (2001). Unseeded region growing for 3d image segmentation. *Pan-Sydney Workshop on Visual Information Processing*. 27

LONGSTRETH, W., PHILLIPS, L., DRANGSHOLT, M., KOEPSELL, T., CUSTER, B., GEHRELS, J. & *et al.* (2004). Dental x-rays and the risk of intracranial meningioma: a population-based case-control study. *Cancer*, **100(5)**, 1026–34. 82

LORIGO, L., FAUGERAS, O., GRIMSON, W., KERIVEN, R. & KIKINIS, R. (1998). Segmentation of bone in clinical knee mri using texture-based geodesic active contours. *Medical Image Computing and Computer Assisted Intervention*, 1195–1204. 41

LOUBELE, M., BOQAERTS, R., DIJCK, E.V., PAUWELS, R., VANHEUSDEN, S., SUETENS, P. & *et al.* (2009). Comparison between effective radiation dose of cbct and msct scanners for dentomaxillofacial applications. *European Journal of Radiology*, **71**, 461–468. 64

LUDLOW, J., DAVIES-LUDLOW, L. & BROOKS, S. (2003). Dosimetry of two extraoral direct digital imaging devices: Newtom cone beam ct and orthophos plus ds panoramic unit. *Dentomaxillofacial Radiology*, **32(4)**, 229–34. 20

LUDLOW, J., LASTER, W., SEE, M., BAILEY, L. & HERSHEY, H. (2007). Accuracy of measurements of mandibular anatomy in cone beam computed tomography images. *Oral Surgery, Oral Medicine, Oral Pathology, Oral Radiology, and Endodontology*, **103**, 534–542. 77

MA, Z., TAVARES, J., JORGE, R. & MASCARENHAS, T. (2010). A review of algorithms for medical image segmentation and their applications to the female pelvic cavity. *Computer Methods in Biomechanics and Biomedical Engineering*, **13(2)**, 235–46. 24

MAH, J., DANFORTH, R., BUMANN, A. & HATCHER, D. (2003). Radiation absorbed in maxillofacial imaging with a new dental computed tomography device. *Oral Surgery, Oral Medicine, Oral Pathology, Oral Radiology, and Endodontology*, **96(4)**, 508–13. 20

MARET, D., MOLINIER, F., BRAGA, J., PETERS, O., TELMON, N., TREIL, J. & *et al.* (2010). Accuracy of 3d reconstructions based on cone beam computed tomography. *Journal of Dental Research*, **89**, 1465–1469. 64

MEHNERT, A. & JACKWAY, P. (1997). An improved seeded region growing algorithm. *Pattern Recognition Letters*, **18**, 1065–1071. 27

MEMON, A., GODWARD, S., WILLIAMS, D., SIDDIQUE, I. & AL-SALEH, K. (2010). Dental x-rays and the risk of thyroid cancer: a case-control study. *Acta Oncologica*, **49(4)**, 447–53. 82

MODAYUR, B., PROTHERO, J., OJEMANN, G., MARAVILLA, K. & BRINKLEY, J. (1997). Visualization-based mapping of language function in the brain. *NeuroImage*, **6**, 245–258. 26, 27

MOHAMED, N., AHMED, M. & FARAG, A. (1999). Modified fuzzy c-mean in medical image segmentation. *ICASSP 1999*, **6**, 3429–3432. 32

MULL, R. (1984). Mass estimates by computed tomography: physical density from ct numbers. *American Journal of Roentgenology*, **143(5)**, 1101–4. 16

NAKAGAWA, Y. & ROSENFELD, A. (1979). Some experiments on variable thresholding. *Pattern Recognition*, **ll**, 191–204. 26

NG, H. (2008). Segmentation of human muscles of mastication from magnetic resonance images. *PhD Thesis*. 8, 29, 30

NG, H., ONG, S., FOONG, K., GOH, P. & NOWINSKI, W. (2006a). Medical image segmentation using k-means clustering and improved watershed algorithm. *Image Analysis and Interpretation, 2006 IEEE Southwest Symposium on*, 61–65. 32

NG, H., ONG, S., HU, Q., FOONG, K., GOH, P. & NOWINSKI, W. (2006b). Muscles of mastication model-based mr image segmentation. *International Journal of Computer Assisted Radiology and Surgery*, **1**, 137–148. 8, 80

NG, H., FOONG, K., ONG, S., LIU, J., GOH, P. & NOWINSKI, W. (2007a). Shape determinative slice localization for patient-specific masseter modeling using shape-based interpolation. *International Journal of Computer Assisted Radiology and Surgery*, **2**, 398–400. 8

NG, H., HU, Q., ONG, S., FOONG, K., GOH, P. & NOWINSKI, W. (2007b). Segmentation of the temporalis from mr data. *International Journal of Computer Assisted Radiology and Surgery*, **2**, 19–30. 8

NG, H., ONG, S., FOONG, K., GOH, P. & NOWINSKI, W. (2008). Masseter segmentation using an improved watershed algorithm with unsupervised classification. *Computers in Biology and Medicine*, **38**, 171–184. 8

NG, H., ONG, S., LIU, J., HUANG, S., FOONG, K., GOH, P. & NOWINSKI, W. (2009). 3d segmentation and quantification of a masticatory muscle from mr data using patient-specific models and matching distributions. *Journal of Digital Imaging*, **22**, 449–462. 8

NG, H., ONG, S., LIU, J., HUANG, S., FOONG, K., GOH, P. & NOWINSKI, W. (2010). Salient features useful for the accurate segmentation of masticatory muscles from minimum slice subsets of magnetic resonance images. *Machine Vision and Applications*, **21**, 449–467. 8

NGAN, D., KHARBANDA, O., GEENTY, J. & DARENDELILER, M. (2003). Comparison of radiation levels from computed tomography and conventional dental radiographs. *Australian Orthodontic Journal*, **19(2)**, 67–75. 20

NGUYEN, T. (2012). Automatic segmentation for dental operation planning. *Diploma thesis*. 6

NGUYEN, T., LAMECKER, H., KAINMUELLER, D. & ZACHOW, S. (2012). Automatic bone and tooth detection for ct-based dental implant planning. *International Journal Computer Assisted Radiology and Surgery*, **7, Supplement 1**. 5

OSHER, S. & FEDKIW, R. (2002). *Level Set Methods and Dynamic Implicit Surfaces*. Springer. 35

OSHER, S. & SETHIAN, J. (1988). Fronts propagating with curvature-dependent speed: Algorithms based on hamilton-jacobi formulations. *Journal of Computational Physics*, **79**, 12–49. 35

OTSU, N. (1979). A threshold selection method from gray level histograms. *IEEE Transactions on Systems, Man, and Cybernetics*, **9**, 62–66. 26

PAL, N. & PAL, S. (1991). Image model, poisson distribution and object extraction. *Int. J. Pattern Recognition Artif. Intell.*, **5**, 459–483. 26

PAL, N. & PAL, S. (1993). A review on image segmentation techniques. *Pattern Recognition*, **26**, 1277–1294. 24

PALOMO, J., PEJAVAR, S. & HANS, M. (2008). Influence of cbct exposure conditions on radiation dose. *Oral Surgery, Oral Medicine, Oral Pathology, Oral Radiology, and Endodontology*, **105**, 773–782. 64

PAPAMARKOS, N., STROUTHOPOULOS, C. & ANDREADIS, I. (2000). Multithresholding of color and gray-level images through a neural network technique. *Image and Vision Computing*, **18**, 213–222. 25

PARAGIOS, N., MELLINA-GOTTARDO, O. & RAMESH, V. (2004). Gradient vector flow fast geometric active contours. *IEEE Transactions on Pattern Analysis and Machine Intelligence*, **26**, 402–407. 34

PARK, J. & LEE, C. (2009). Skull stripping based on region growing for magnetic resonance brain images. *NeuroImage*, **47**, 1394–1407. 26, 28, 41, 43, 47, 59

PEREZ, A. & GONZALEZ, R. (1987). An iterative thresholding algorithm for image segmentation. *IEEE Transactions on Pattern Analysis and Machine Intelligence*, **9**, 742–751. 26

PHAM, D., PRINCE, J., DAGHER, A. & XU, C. (1997). An automated technique for statistical characterization of brain tissues in magnetic resonance imaging. *Int. J. Patt. Rec. Art. Intel.*, **11(8)**, 1189–1211. 24

PHILLIPS, D. & LANNUTTI, J. (1997). Measuring physical density with x-ray computed tomography. *NDT & E International*, **30**, 339C350. 16

PLUEMPITIWIRIYAWEJ, C., MOURA, J., WU, Y. & HO, C. (2005). Stacs: New active contour scheme for cardiac mr image segmentation. *IEEE Transactions on Medical Imaging*, **24**, 593–603. 91

POHLMAN, S., POWELL, K., OBUCHOWSKI, N., CHILCOTE, W. & GRUNDFEST-BRONIATOWSKI, S. (1996). Quantitative classification of breast tumores in digitzed mamograms. *Medical Physics*, **23**, 1337–1345. 28

PRASTAWA, M., BULLITT, E. & GERIG, G. (2009). Simulation of brain tumors in mr images for evaluation of segmentation efficacy. *Medical Image Analysis*, **13(2)**, 297–311. 22

RAHMATI, P., ADLER, A. & HAMARNEH, G. (2012). Mammography segmentation with maximum likelihood active contours. *Medical Image Analysis*, **16**, 1167–86. 30

RAJAPAKSE, J., GIEDD, J. & RAPOPORT, J. (1997). Statistical approach to segmentation of single-channel cerebral mr images. *IEEE Transactions on Medical Imaging*, **16**, 176–186. 31

RICE, H., FRUSH, D., FARMER, D., WALDHAUSEN, J. & COMMITTEE, A.E. (2007). Review of radiation risks from computed tomography: essentials for the pediatric surgeon. *Journal of Pediatric Surgery*, **42**, 603–607. 64

RIFAI, H., BLOCH, I., HUTCHINSON, S., WIART, J. & GARNERO, L. (2000). Segmentation of the skull in mri volumes using deformable model and taking the partial volume effect into account. *Medical Image Analysis*, **4**, 219–233. 41

ROBERTS, M., COOTES, T. & ADAMS, J. (2003). Linking sequences of active appearance sub-models via constraints: An application in automated vertebral morphometry. *Proc. Brit. Mach. Vis. Conf.*, **1**, 349C358. 38

ROERDINK, J. & MEIJSTER, A. (2000). The watershed transform: Definitions, algorithms and parallelization strategies. *Fundamental Informaticae*, **41**, 187–228. 28

ROY, S., CARASS, A., BAZIN, P., RESNICK, S. & PRINCE, J. (2012). Consistent segmentation using a rician classifier. *Medical Image Analysis*, **16**, 524–535. 30

RUEDA, S., GIL, J., PICHERY, R. & RAYA, A. (2006). Automatic segmentation of jaw tissues in ct using active appearance models and semi-automatic landmarking. *Medical Image Computing and Computer-Assisted Intervention*, **21**, 167–174. 5

SADANANTHAN, S., ZHENG, W., CHEE, M. & ZAGORODNOV, V. (2010). Skull stripping using graph cuts. *NeuroImage*, **49**, 225–239. 41

SAHOO, P., SOLTANI, S. & A.K.C.WONG (1988). A survey of thresholding techniques. *Comput. Vis. Graph. Im. Proc.*, **41**, 233–260. 26

SCAF, G., LURIE, A., MOSIER, K., KANTOR, M., RAMSBY, G. & FREEDMAN, M. (1997). Dosimetry and cost of imaging osseointegrated implants with film-based and computed tomography. *Oral Surgery, Oral Medicine, Oral Pathology, Oral Radiology, and Endodontology*, **83(1)**, 41–8. 20

SCARFE, W., FARMAN, A. & SUKOVIC, P. (2006). Clinical applications of cone-beam computed tomography in dental practice. *Journal of the Canadian Dental Association*, **72**, 75–80. 3, 16, 17, 20, 64

SCHALKOFF, R. (1992). *Pattern Recognition: Statistical, Structural and Neural Approaches*. John Wiley and Sons. 30

SCHMID, J., KIM, J. & MAGNENAT-THALMANN, N. (2011). Robust statistical shape models for mri bone segmentation in presence of small field of view. *Medical Image Analysis*, **15**, 155–168. 41, 42, 65

SCHULZE, D., HEILAND, M., THURMANN, H. & ADAM, G. (2004). Radiation exposure during midfacial imaging using 4- and 16-slice computed tomography, cone beam computed tomography systems and conventional radiography. *Dentomaxillofacial Radiology*, **33(2)**, 83–6. 20, 82

SHAHVARAN, Z., KAZEMI, K., HELFROUSH, M., JAFARIAN, N. & NOORIZADEH, N. (2012). Variational level set combined with markov random field modeling for simultaneous intensity non-uniformity correction and segmentation of mr images original research article. *Journal of Neuroscience Methods*, **209**, 280–289. 31

SHAN, Z., YUE, G. & LIU, J. (2002). Automated histogram-based brain segmentation in t1-weighted three-dimensional magnetic resonance head images. *NeuroImage*, **17**, 1587–1598. 41

SHARMA, N. & AGGARWAL, L. (2010). Automated medical image segmentation techniques. *J Med Phys*, **35(1)**, 3–14. 24

SMITH, S. (2002). Fast robust automated brain extraction. *Human Brain Mapping*, **17**, 143–155. 41

SONKA, M., PARK, N. & HOFFMAN, E. (1996). Rule-based detection of intrathoracic airway trees. *IEEE Transactions on Medical Imaging*, **15**, 314–326. 26, 43

SUETENS, P., BELLON, E., VANDERMEULEN, D., SMET, M., MARCHAL, G., NUYTS, J. & MORTELMANS, L. (1993). Image segmentation: methods and applications in diagnostic radiology and nuclear medicine. *European Journal of Radiology*, **17**, 14–21. 24

SUKOVIC, P. (2003). Cone beam computed tomography in craniofacial imaging. *Orthodontics & Craniofacial Research*, **6(Suppl 1)**, 31–6. 19

TAYLOR, P. (1995). Invited review: computer aids for decision-making in diagnostic radiology-a literature review. *British Journal of Radiology*, **68**, 945–957. 22

TEK, H. & ARAS, H. (2004). Local watershed operators for image segmentation. *Proceedings of the 7th International Conference on Medical Image Computing and Computer-Assisted Intervention*, 127–134. 29

TSAI, A., YEZZY, A., WELLS, W., TEMPANY, C., TUCKER, D., FAN, A. & *et al.* (2003). A shape-based approach to the segmentation of medical imagery using level sets. *IEEE Transactions on Medical Imaging*, **22**, 137–154. 35, 84

UKIL, S. & REINHARDT, S. (2009). Anatomy-guided lung lobe segmentation in x-ray ct images. *IEEE Transactions on Medical Imaging*, **28(2)**, 202C214. 30

VINCENT, L. & SOILLE, P. (1991). Watersheds in digital spaces: an efficient algorithm based on immersion simulations. *IEEE Transaction on Pattern Analysis and Machine Intelligence*, **13(6)**, 583–598. 28

WEINSTOCK, R. (1952). *Calculus of Variations with Applications to Physics and Engineering*. Dover Publications, New York. 34

WHITE, S. (1992). 1992 assessment of radiation risk from dental radiography. *Dentomaxillofacial Radiology*, **21(3)**, 118–26. 20

WIRJADI, O. (2007). *Survey of 3D image segmentation methods*. Fraunhofer-Institut furTechnound Wirtschaftsmathematik. 24

XU, C. & PRINCE, J. (1998). Snakes, shapes, and gradient vector flow. *IEEE Transactions on Image Processing*, **3**, 359–369. 8, 34, 83

YANOWITZ, S. & BRUCKSTEIN, A. (1989). A new method for image segmentation. *Computer Vision, Graphics, and Image Processing*, **416**, 82–95. 26

YUSHKEVICH, P., PIVEN, J., HAZLETT, H., SMITH, R., HO, S., GEE, J. & *et al.* (2006). User-guided 3d active contour segmentation of anatomical structures: Significantly improved efficiency and reliability. *NeuroImage*, **31**, 1116–1128. 52, 66

ZHANG, J., YAN, C., CHUI, C. & ONG, S. (2010). Fast segmentation of bone in ct images using 3d adaptive thresholding. *Computers in Biology and Medicine*, **40**, 231–236. 25, 26

ZHANG, Y., BRADY, M. & SMITH, S. (2001). Segmentation of brain mr images through a hidden markov random field model and the expectation-maximization algorithm. *IEEE Transactions on Medical Imaging*, **20**, 45–57. 41

ZHANG, Z. (1994). Iterative point matching for registration of free-form curves and surfaces. *International Journal of Computer Vision*, **13**, 119–152. 66

ZIEGLER, C., WOERTCHE, R., BRIEF, J. & HASSFELD, S. (2002). Clinical indications for digital volume tomography in oral and maxillofacial surgery. *Dentomaxillofacial Radiology*, **31**, 126–30. 19

ZOROOFI, R., NISHII, T., SATO, Y., SUGANO, N., YOSHIKAWA, H. & TAMURA, S. (2001). Segmentation of avascular necrosis of the femoral head using 3-d mr images. *Computerized Medical Imaging and Graphics*, **25**, 511–521. 41

Appendix A: minimization of the proposed energy functional

In Chapter 5, we need to minimize the overall energy functional in Eq. 5.25, which we restate here for convenience

$$\begin{aligned} J(\phi) = & \lambda_1 \int_\Omega \frac{1}{2}(|\nabla\phi| - 1)^2 dxdy \\ & + \lambda_2 \left(\int_\Omega -\ln(p_1) H(-\phi) dxdy + \int_\Omega -\ln(p_2)\left(1 - H(-\phi)\right) dxdy \right) \\ & + \lambda_3 \int_\Omega g\delta(\phi)|\nabla\phi| dxdy \\ & + \lambda_4 \int_\Omega \hat{\phi}_0^2 \delta(\phi)|\nabla\phi| dxdy \\ & + \lambda_5 \int_\Omega \phi_t (H(\phi_t) - H(\phi)) dxdy \end{aligned} \tag{1}$$

Define $F_1 = \frac{1}{2}\lambda_1(|\nabla\phi| - 1)^2$, $F_2 = \lambda_3 g\delta(\phi)|\nabla\phi| + \lambda_4\hat{\phi}_0^2\delta(\phi)|\nabla\phi|$, $F_3 = \lambda_2\left[-\ln(p_1)H(-\phi) - \ln(p_2)(1 - H(-\phi))\right] + \lambda_5\phi_t(H(\phi_t) - H(\phi))$. Apply the Euler-Lagrange equation 2.4 to $J(\phi)$, we get

$$\frac{\partial F_3}{\partial \phi} - \frac{d}{dx}\left(\frac{\partial F_1}{\partial \phi_x}\right) - \frac{d}{dy}\left(\frac{\partial F_1}{\partial \phi_y}\right) - \frac{d}{dx}\left(\frac{\partial F_2}{\partial \phi_x}\right) - \frac{d}{dy}\left(\frac{\partial F_2}{\partial \phi_y}\right) = 0 \tag{2}$$

where

$$
\begin{aligned}
\frac{d}{dx}\left(\frac{\partial F_1}{\partial \phi_x}\right) + \frac{d}{dy}\left(\frac{\partial F_1}{\partial \phi_y}\right) &= \frac{d}{dx}\left(\lambda_1(|\nabla\phi|-1)\frac{\partial\left(\sqrt{\phi_x^2+\phi_y^2}\right)}{\partial \phi_x}\right) \\
&\quad + \frac{d}{dy}\left(\lambda_1(|\nabla\phi|-1)\frac{\partial\left(\sqrt{\phi_x^2+\phi_y^2}\right)}{\partial \phi_y}\right) \\
&= \frac{d}{dx}\left(\lambda_1(|\nabla\phi|-1)\frac{\phi_x}{|\nabla\phi|}\right) + \frac{d}{dy}\left(\lambda_1(|\nabla\phi|-1)\frac{\phi_y}{|\nabla\phi|}\right) \\
&= \frac{d}{dx}\left(\lambda_1\left(\phi_x - \frac{\phi_x}{|\nabla\phi|}\right)\right) + \frac{d}{dy}\left(\lambda_1\left(\phi_y - \frac{\phi_y}{|\nabla\phi|}\right)\right) \\
&= \lambda_1\left(\frac{d}{dx}(\phi_x) + \frac{d}{dy}(\phi_y)\right) \\
&\quad - \lambda_1\left(\frac{d}{dx}\left(\frac{\phi_x}{|\nabla\phi|}\right) + \frac{d}{dy}\left(\frac{\phi_y}{|\nabla\phi|}\right)\right) \\
&= \lambda_1\left(\Delta\phi - \mathtt{div}\left(\frac{\nabla\phi}{|\nabla\phi|}\right)\right)
\end{aligned}
\tag{3}
$$

$$
\begin{aligned}
\frac{d}{dx}\left(\frac{\partial F_2}{\partial \phi_x}\right) + \frac{d}{dy}\left(\frac{\partial F_2}{\partial \phi_y}\right) &= \frac{d}{dx}\left((\lambda_3 g + \lambda_4\hat{\phi}_0^2)\delta(\phi)\frac{\partial\left(\sqrt{\phi_x^2+\phi_y^2}\right)}{\partial \phi_x}\right) \\
&\quad + \frac{d}{dy}\left((\lambda_3 g + \lambda_4\hat{\phi}_0^2)\delta(\phi)\frac{\partial\left(\sqrt{\phi_x^2+\phi_y^2}\right)}{\partial \phi_y}\right) \\
&= \frac{d}{dx}\left((\lambda_3 g + \lambda_4\hat{\phi}_0^2)\delta(\phi)\frac{\phi_x}{|\nabla\phi|}\right) \\
&\quad + \frac{d}{dy}\left((\lambda_3 g + \lambda_4\hat{\phi}_0^2)\delta(\phi)\frac{\phi_y}{|\nabla\phi|}\right) \\
&= \delta(\phi)\mathtt{div}\left((\lambda_3 g + \lambda_4\hat{\phi}_0^2)\frac{\nabla\phi}{|\nabla\phi|}\right)
\end{aligned}
\tag{4}
$$

$$\begin{aligned}\frac{\partial F_3}{\partial \phi} &= \lambda_2 \left[\ln(p_1)\delta(\phi) - \ln(p_2)\delta(\phi)\right] - \lambda_5 \phi_t \delta(\phi) \\ &= -\lambda_2 \delta(\phi) \ln\left(\frac{p_2}{p_1}\right) - \lambda_5 \delta(\phi)\phi_t\end{aligned} \tag{5}$$

Thus, the Euler-Lagrange equation becomes

$$\begin{aligned}&- \lambda_2 \delta(\phi) \ln\left(\frac{p_2}{p_1}\right) - \lambda_5 \delta(\phi)\phi_t \\ &- \lambda_1 \left(\Delta\phi - \mathtt{div}\left(\frac{\nabla\phi}{|\nabla\phi|}\right)\right) \\ &- \delta(\phi)\mathtt{div}\left((\lambda_3 g + \lambda_4 \hat{\phi}_0^2)\frac{\nabla\phi}{|\nabla\phi|}\right) = 0\end{aligned} \tag{6}$$

According to Eq. 2.5, we have

$$\begin{aligned}&\frac{\partial \phi}{\partial t} = \lambda_1 \left[\Delta\phi - \mathtt{div}(\frac{\nabla\phi}{|\nabla\phi|})\right] + \lambda_2 \delta(\phi) \ln\left(\frac{p_2}{p_1}\right) \\ &+\delta(\phi)\left(\mathtt{div}\left((\lambda_3 g + \lambda_4 \hat{\phi}_0^2)\frac{\nabla\phi}{|\nabla\phi|}\right)\right) + \lambda_5 \delta(\phi)\phi_t\end{aligned} \tag{7}$$

Publication List

[1] JI, D.X., FOONG, K.W.C. & ONG, S.H. (2013). A two-stage rule-constrained seedless region growing approach for mandibular body segmentation in MRI. *International Journal of Computer Assisted Radiology and Surgery*, **published online**.

[2] JI, D.X., ONG, S.H. & FOONG, K.W.C. A level-set based approach for anterior teeth segmentation in cone beam computed tomography images. *Computers in Biology and Medicine*, **submitted**.

[3] JI, D.X., FOONG, K.W.C., ONG, S.H. & TAKADA, K. (2011). Reconstruction of mandibular shape from magnetic resonance imaging-a precision study. *62nd AAOMR Annual Meeting*, 87.

[4] XU, J.X. & JI, D.X. (2010). A feature-based data-driven approach for controller design and tuning. *2010 IEEE International Conference on Cybernetics and Intelligent Systems & Robotics, Automation and Mechatronics*, 172-178.

[5] XU, J.X., DENG, X. & JI, D.X. (2010). Study on C. elegans behaviors using recurrent neural network model. *2010 IEEE International Confer-*

ence on Cybernetics and Intelligent Systems & Robotics, Automation and Mechatronics, 1-6.